Relationships between the molecular structure and the mechanical and physico-chemical properties of semicrystalline polymers

Boris Belin

THESE DE DOCTORAT

NNT : 2023UPASF097

université PARIS-SACLAY

Relationships between the molecular structure and the mechanical and physico-chemical properties of semicrystalline polymers

Relations entre la structure moléculaire et les propriétés mécaniques et physico-chimiques des polymères semicristallins

Thèse de doctorat de l'université Paris-Saclay

École doctorale n° 579, Sciences Chimiques : Molécules, Matériaux, Instrumentation et Bio-systèmes (2MIB)
Spécialité de doctorat : Physique
Graduate School : Chimie. Référent : Faculté des sciences d'Orsay

Thèse préparée à l'unité de recherche **Institut de Chimie Physique** (Université Paris-Saclay, CNRS),
sous la direction de **Benard ROUSSEAU**, Directeur de recherche,
la co-direction de **Véronique LACHET** , Ingénieure de recherche,
et la co-supervision de **Marianna YIANNOURAKOU**, Ingénieure de recherche à Materials Design S.A.R.L.

Thèse soutenue à Orsay, le 20 Décembre 2023, par

Boris BELIN

Composition du Jury

Membres du jury avec voix délibérative

Marie-Pierre GAIGEOT Professeure, Université Paris-Saclay Laboratoire Analyse, Modélisation, Matériaux pour la Biologie et l'environnement	Présidente
Julie DIANI Directrice de recherche Laboratoire de mécanique des solides, Ecole polytechnique	Rapporteure & Examinatrice
Florent GOUJON Maître de conférence (HDR), Université Clermont-Auvergne Institut de Chimie de Clermont-Ferrand	Rapporteur & Examinateur
Eliane ESPUCHE Professeure, Université Claude Bernard Lyon 1 Ingénierie des matériaux polymères	Examinatrice
Séverine QUEYROY Maitresse de conférence, Aix Marseille Université Institut de Chimie Radicalaire	Examinatrice

université PARIS-SACLAY

ÉCOLE DOCTORALE
Sciences Chimiques : Molécules, Matériaux, Instrumentation et Biosystèmes (2MIB)

Titre: Relations entre la structure moléculaire et les propriétés mécaniques et physico-chimiques des polymères semicristallins

Mots clés: simulation moléculaire; polymère semicristallin; propriétés mécaniques; perméation

Résumé: Cette thèse est consacrée à l'étude des polymères semicristallins par simulation à l'échelle moléculaire. Elle s'est déroulée dans le cadre d'une collaboration entre l'entreprise Materials Design S.A.R.L., l'Institut de Chimie Physique d'Orsay, et l'IFP Energies nouvelles. Notre objectif était de fournir une méthode générale de construction d'échantillons semicristallins et de l'implémenter dans une suite logicielle puis d'utiliser cet outil pour obtenir des propriétés structurales, mécaniques et de perméabilité à de petites molécules de gaz.
Les polymères semicristallins sont des matériaux dans lesquels coexistent des régions cristallines et des régions amorphes. On se situe ici à l'échelle de l'alternance cristal-amorphe, sur des dimensions de l'ordre de quelques dizaines de nanomètres. Les études expérimentales ne permettent pas de caractériser précisément le chemin suivi par les chaines de polymères dans ces deux phases et à leur interface, il est donc ardu de construire des échantillons pour la simulation à l'échelle moléculaire.
Dans la première partie de cette thèse, nous avons adapté une théorie issue de la physique statistique des polymères, afin de construire différents échantillons de polyéthylène semicristallin. Différents paramètres utilisés lors de la construction permettent de contrôler le degré de cristallinité et la proportion de sections de chaînes amorphes pontant deux zones cristallines. Dans la seconde partie, nous avons étudié les propriétés mécaniques, dans le domaine élastique et sous haute déformation de différents échantillons de polyéthylène. Nous avons observé l'importance du degré de cristallinité pour les propriétés élastiques, auquel s'ajoute la proportion de section de chaînes pontantes liant deux phases crystallines dans le cas de la haute déformation. Enfin, nous avons réalisé des calculs numériques de solubilité et de diffusion de CH_4 et CO_2 dans le polyéthylène. Les résultats obtenus sur la sorption sont en accord avec les résultats expérimentaux.

université PARIS-SACLAY

ÉCOLE DOCTORALE
Sciences Chimiques : Molécules, Matériaux, Instrumentation et Biosystèmes (2MIB)

Title: Relationships between the molecular structure and the mechanical and physicochemical properties of semicrystalline polymers

Keywords: molecular simulation; semicrystalline polymer; mechanical properties; permeation

Abstract: This thesis is dedicated to the study of semicrystalline polymers through molecular-scale simulations. It was carried out in collaboration between the company Materials Design S.A.R.L., the Institut de Chimie Physique in Orsay, and IFP Energies nouvelles. Our objective was to provide a general method for building semicrystalline structures and to implement it in software. Subsequently, we used this tool to obtain structural, mechanical, and gas permeability properties. Semicrystalline polymers are materials in which crystalline regions coexist with amorphous regions. We are operating at the scale of the crystal-amorphous alternation, on dimensions of the order of a few tens of nanometers. Experimental studies do not precisely characterize the paths followed by polymer chains in these two phases and at their interface. Therefore, building models for molecular-scale simulation is challenging.

In the first part of this thesis, we adapted a polymer statistical physics theory to construct various samples of semi-crystalline polyethylene. Different parameters used during construction allow us to control the degree of crystallinity and the proportion of amorphous chain sections bridging two crystalline regions.

In the second part, we investigated the mechanical properties, both in the elastic domain and under high deformation, of different polyethylene samples. We observed the importance of the degree of crystallinity for elastic properties, coupled with the proportion of bridging chain sections connecting two crystalline phases in the case of high deformation.

Finally, we conducted numerical calculations of the solubility and diffusion of methane and carbon dioxide in polyethylene. The obtained results on sorption are in agreement with experimental findings and prior studies.

Remerciements

Je souhaite exprimer ma sincère reconnaissance envers mes encadrants, Bernard, Véronique et Marianna, pour leur guidance dans ce projet de thèse. Chacun d'eux m'a offert un encadrement de qualité mêlant conseils avisés et confiance en mon autonomie. J'aspire à m'inspirer de leurs qualités scientifiques et humaines tout au long de mon parcours professionnel.

Mes remerciements vont également aux institutions qui ont financé et organisé cette thèse de doctorat, en commençant par mon employeur, Materials Design S.A.R.L. Cette entreprise, qui met au service de l'industrie des ressources humaines n'ayant rien à envier à un laboratoire de sciences fondamentales de haut niveau, fut un lieu idéal pour mener cette thèse. Mes remerciements vont également à l'IFP Energies Nouvelles, un institut de recherche stimulant d'un point de vue scientifique et qui, en contribuant généreusement à ma participation à des congrès scientifiques, m'a permis de découvrir cette facette de la recherche. Je n'oublie pas le CNRS et l'Université Paris-Saclay, qui ont joué un rôle bien sûr déterminant.

Un grand merci à tous mes collègues, notamment Benoît Minisini et Dave Rigby pour leurs conseils en physique des polymères et en simulation numérique, Benoît Leblanc et Jason Aubry pour leur précieuse aide dans le développement. Bien sûr, mes salutations vont à Erich Wimmer et Clive Freeman, nos grands chefs, ainsi qu'à tous mes autres collègues avec qui j'ai partagé d'agréables moments, que ce soit au bureau ou sur un bateau, tels que Marthe, Jessica, Jörg, Walter, Leonid, Kyle, Laetitia, Naida, Reynald, René, Pierre-Arnaud, Kasia et tous les autres. Un remerciement particulier à Fabrice Detrez, qui a assuré le suivi annuel de ma thèse et avec qui j'ai eu des discussions scientifiques et amicales enrichissantes.

Mes pensées vont également à ma famille, à mon père Jean-Louis, ma mère Elisabeth, et mes deux frères Samuel et Antoine. Le souvenir de mes deux grands-mères, Odette et Monique, décédées au début du doctorat à un mois d'intervalle, a accompagné ce travail. Leur soutien m'a été précieux jusqu'à la fin de leurs vies.

Enfin, je souhaite exprimer mes sentiments profonds envers ma compagne, Diana. Au-delà du romantisme que les mots écrits ici ne pourraient rendre compte que très imparfaitement. La possibilité de poursuivre ces études découle aussi de notre bonne entente, de l'entraide au cours de ces dernières années, qui nous a permis de progresser dans nos projets communs et personnels. Je suis convaincu que nous formerons une famille heureuse avec l'arrivée prochaine de notre fils.

[...] We may reflect at this point whether and when the right questions have been asked. I maintain that some of the questions in the recent past have been fallacious and largely contributed to the polarization of views. The fallacy, I feel, has been to believe that one single set of neutron scattering data on one rather arbitrarily chosen piece of polyethylene can decide the whole issue of how a polymer crystallizes and the nature of its structure. The history of science has taught many lessons about the fallacious beliefs in a single decisive experiment to settle controversial issues once and for all. If such a belief often foundered with apparently clear-cut simple issues, how can one hope that it will yield results on a piece of isotropically doped quench crystallized polyethylene as examined for low-angle neutron scattering? Science advances not by resolving but by bypassing the inappropriate questions! As regards the issue under discussion, this is far from decided even as far as expectation of a single decision is appropriate. I believe we are only now at a stage that the relevant variables have been identified allowing a meaningful attack on the central issues to be planned.

So far I endeavoured to give an essentially non-committal account. Having minimised the extent and magnitude of the conflicting issues at this point I reached a stage where what is left as controversial remains open ended: "it could go this way or that, let us wait and see". I feel that in the interest of scientific objectivity this was my duty to do. Yet I realize that there is something intrinsically unsatisfactory in a totally non-committal attitude. Man is not purely a reasoning apparatus, (if nothing else the present controversies show this) but also has his convictions which guide him and which he is trying to impress on others. This applies to science as well as to other spheres, and within science even to the otherwise most objectively reasoned argumentation. Some of the most momentous advances in science, just as the most futile controversies, were punctuated by strong personal commitments, recall say Galileo and the Vatican, where the latter has shown more reason and objectivity than normally credited by the popular image, or closer to our times and topic, the events concerning the discovery of macromolecules. Arguments which lack this force of personal conviction remain unappealing and will in fact fail to leave their mark. Having done my duty of a comparatively impartial chronicler I feel that by now I have earned the licence to express also my own views.[...]

Crystalline Polymers: an Introduction *BY A. KELLER H., 1979, in Faraday Discussions of the Chemical Society.*

Comment on the quote*: In 1979, the Faraday Discussions of the Chemical Society were dedicated to addressing the challenge of polymer crystallization, both for pure and semicrystalline variants, along with the resulting morphologies. The introductory paper by Keller aimed to ease the tensions resembling a Cold War between proponents of the switchboard model and the adjacent folding reentry model. Keller showed that the conflicts were considerably exaggerated, with different sides' positions being caricatured by their opponents.*

Additionally, Keller cautioned against premature conclusions in the study of these intricate metastable materials. Polymers exhibit polydispersity and diverse branching degrees, their potential thermodynamic path to crystallization are infinite. Researchers may be inclined to prematurely declare "Eureka" based on isolated experiment outcomes. Yet, as previously mentioned, the challenge lies in meticulously controlling the myriad parameters that define a given polymer, as well as understanding the thermodynamic pathways to crystallization.

Concluding this study, it becomes evident that there is no singular solution to the morphology question; rather, a spectrum of potential morphologies exists, ranging from the two classical models : switchboard model and adjacent reentry model. The longstanding struggle over morphology appears to have subsided, not due to a definitive victory, but rather because the controversy itself is dissipating.

Contents

List of Figures

List of Tables

Chapter 1

Introduction

The goal of the study is to investigate the relationship between the morphology of semicrystalline polymers at the molecular scale and their mechanical and transport properties through simulation.

The study may be divided into different phases:

- The development of a method to construct semicrystalline structures at the molecular scale, controlling certain aspects of the morphology.
- The computation of mechanical properties.
- The computation of solubility and diffusion coefficients.

1.1 Context of the academic and industrial partnership

The thesis project is conducted within the framework of a CIFRE scholarship. It is a collaboration between the *Institut de Chimie-Physique* in Orsay, *IFP Energies nouvelles*, and *Materials Design S.A.R.L./Inc*. The thesis is under the supervision of Bernard Rousseau (CNRS) as the thesis director, co-supervised by Véronique Lachet (IFPEN) as the thesis co-director, and overseen by Marianna Yiannourakou at *Materials Design*.

The three partners were previously connected through the GIBBS code, a Monte Carlo code developed by *ICP* and *IFPEN*, with Bernard Rousseau and Véronique Lachet being responsible of the development. This code has been implemented and is commercially available within the materials simulation software MedeA, developed by *Materials Design*.

The collaboration's context arises from an interest in the fundamental science underlying the complex relationships between semicrystalline polymer morphology and the mechanical and transport properties, on the CNRS side. *IFP Energies nouvelles* has an interest in applications for the oil and gas industry, while Materials Design aims to enhance its understanding of semicrystalline modeling with the goal of providing new research services and modeling tools in the field of polymers.

1.2 Industrial interest

Polymers can be shaped into various forms using a wide range of industrial processes such as molding, thermoforming, and 3D printing, rendering them highly versatile. Many industries employ them for their mechanical, permeation, dielectric, optical, thermal, and chemical properties, among others.

IFP Energies nouvelles has had a long-standing interest in the polymer properties relevant to flexible pipes in the oil and gas industries. Polymers like HDPE shield the metallic components of the pipes from corrosion caused by the oil inside and seawater outside. Investigating the permeation of these polymers to gases is crucial in this field.

Semicrystalline polymers find extensive use in various sectors, including automotive, aerospace, pharmaceuticals, and the food industry, among others. Permeability and mechanical properties at different temperatures and pressures are sometimes challenging to replicate in a laboratory setting but can be accessed through simulation.

This work may be useful for other applications, which fall outside the scope of this study. For instance, modern televisions often utilize OLED technology, which incorporates semicrystalline polymers as semiconductors. While electronic properties were not the focus of this work, the same model-building procedures could be applied to investigate electronic properties in organic semiconductors with the assistance of Density Functional Theory. New solid-state batteries that involve polymers would also benefit from polymer model-building capabilities. The fact that this study primarily focuses on transport and mechanical properties does not preclude the use of the same model-building procedures to compute other properties with other computational methods.

1.3 Structure of the thesis dissertation

Chapter 2 is dedicated to the bibliography and begins with a discussion on semicrystalline polymer morphology. It highlights the complex paths polymer chains follow in semicrystalline structures. Some regions present an alignment of the chains, while others exhibit disorder. The transition between the crystalline and amorphous phases remains a subject of debate, with unanswered questions about the proportion of perfect foldings of polymer chains at the edges of crystalline regions. Another debated question is the fraction of polymer sections bridging crystalline phases, finishing their path in the amorphous phase or looping back into the crystalline phase they emerged from. The chapter reviews four existing procedures for building molecular-scale semicrystalline structures for simulation, comparing their advantages and disadvantages. Finally, it provides a brief overview of the literature on mechanical and permeation properties.

The chapter 3 begins with an introduction to the basics of the simulation tools used, specifically Molecular Dynamics and Monte Carlo. The most critical part of the chapter is dedicated to an original method for building semicrystalline polymer models. This method relies on a statistical physics theory [Adhikari and Muthukumar, 2019] that predicts the fractions of amorphous chain sections types (tie chain, loop, or tail chain) and the probability distribution of their lengths. The inputs of this statistical theory are employed to control the molecular-scale morphology. Technical details of the implementation are explained.

In the chapter 4, a characterization of the semicrystalline models obtained using our building method is presented. This includes simple characterizations such as density profiles

and degrees of crystallinity, as well as more complex ones, like the quantity of entanglements. The chapter also covers computations of mechanical properties that are strongly dependent on morphological characteristics.

The chapter 5 focuses on the computation of the solubility coefficient and diffusivity of CO_2 and CH_4. For sorption, a method involving Grand Canonical Monte Carlo with frozen polymer chains and molecular dynamics for swelling and chain relaxation was iteratively used. Computation of diffusion coefficients was carried out and compared with experimental data. The final section investigates the coupling between sorption and mechanical properties, particularly the plasticizing effect due to the sorbed CO_2 with T_g computations.

Finally, in the chapter 6, the study's strengths and limitations are discussed. Regarding semicrystalline polymer model building, the chapter presents models of other polymers and proposes simplifications or less idealized model building procedures. Concerning the properties, possibilities to extend the scope of the computed mechanical properties are discussed, as well as improvements in the precision of sorption computations and diffusion coefficients.

Chapter 2

State of the art

A semicrystalline polymer material consists of polymer components arranged in a highly ordered structure, where the polymer chains align with each other to form crystallites separated by an amorphous phase (see Figure 2.1). Polymers are made up of linearly bound molecular units that repeat, connected by covalent bonds. In this material, a polymer chain traverses both phases, moving through crystalline domains where it aligns with other polymer sections, as well as amorphous domains where it follows a disordered path.

Several polymers exhibit a semicrystalline structure, including poly-aryletherketones, polyamides, and polyolefins, among others. This study focuses on linear polyethylene, which has a backbone composed of CH_2 groups. It is the simplest polymer and therefore the preferred model for developing methods for molecular simulation and computational workflows to calculate physicochemical properties. While the dissertation primarily focuses on semicrystalline polyethylene, the methods presented are intended to be general enough to be applied to other semicrystalline polymers. Examples of model constructions for other polymers will be shown in the conclusion chapter.

In this chapter, we will offer a non-exhaustive review of the literature concerning what is known about the morphology, modeling of semicrystalline polymers, as well as their mechanical and permeation properties.

Section 2.1 will present the morphology of semicrystalline polymers, starting from the large scale and progressing to the small scale. Section 2.2 will discuss different methods proposed in the literature for building semicrystalline polymer models for molecular simulation. Finally, sections 2.3 and 2.4 will provide a concise overview of experimental and simulation literature results concerning the mechanical properties and theory of permeation properties in semicrystalline structures.

2.1 Semicrystalline morphology from the mesoscale to the molecular scale

Using an optical microscope, it is possible to observe micrometer-scale structures known as spherulites (see Figure 2.2). By examining the X-ray powder diffraction pattern (see Figure 2.3), it becomes apparent that the semicrystalline polymer material consists of both a crystalline phase (see Figure 2.4) and an amorphous phase [Murthy and Minor, 1990]. The diffraction pattern exhibits peaks corresponding to crystalline planes and an amorphous halo, indicating the presence of both phases. This leads to the question of how the crystalline and amorphous phases are organized within the spherulites.

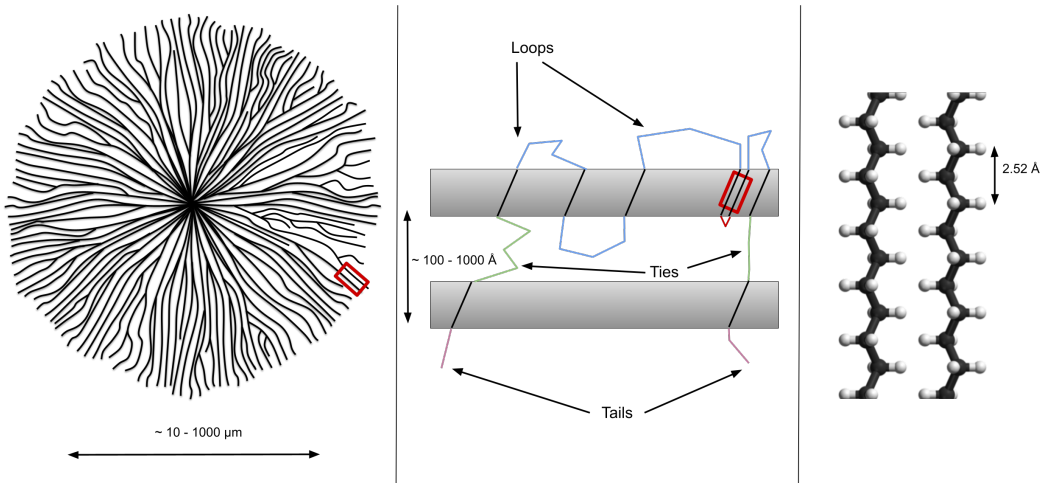

Figure 2.1: *"Multiscale" scheme of semicrystalline polymers. Left: a micron-sized spherulite consisting of crystalline lamellae emanating from a nucleation center in all directions. These lamellae are aligned polymers forming a crystalline region. Middle: a single polymer chain is represented crossing two lamellae in grey, the chain sections in the amorphous regions are of three types: loops in blue, the polymer is reentering the same lamella, bridge or tie chains in green, the polymer is bonding two lamellae, and tails in purple, the polymer ends in the unordered phase. The red walk is called an adjacent reentry, also called a perfect fold. This is the smallest possible loop. Right: a representation of two crystalline paralleled polyethylene chains. The red rectangles show the successive magnification from left to right.*

2.1.1 Spherulite

When observing spherulites under microscopy between two perpendicular polarizers, distinct Maltese cross patterns become visible (see Figure 2.5). These patterns provide valuable insights into the organization of the crystalline phase within the spherulites [Lenz and Stein, 1973]. Parallel linear polymer chains act as polarizers. When their direction aligns with one of the crossed polarizers, minimal light is transmitted. However, as the chains deviate from alignment with the polarizers, the transmission of light increases. This effect gives rise to dark perpendicular cones, forming the characteristic Maltese cross, as well as bright regions. The degree of transmission also depends on the wavelength, partly due to the polymer's absorption properties [Ehrenstein and Theriault, 2001].

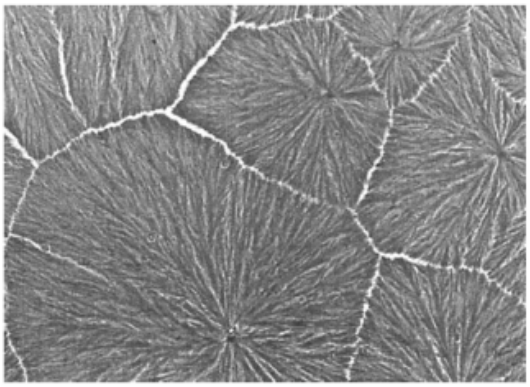

Figure 2.2: *Poly(ethylene propylene) spherulites observed with microscopy [Pethrick, 2007].*

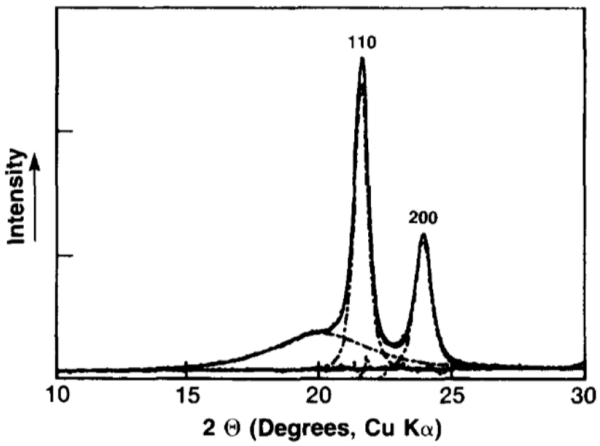

Figure 2.3: *Profile analysis of a diffractometer scan from polyethylene. The full line is the observed data points, the broken curves are the profile of the separated components (amorphous and crystalline phase). The numbers identifying the peaks are Miller indices [Murthy and Minor, 1990].*

When spherulites are rotated within their plane, the corresponding Maltese cross patterns remain unchanged, indicating that the molecular arrangement is consistent regardless of the polar angle. This reveals that the molecular axis of the polymer molecules in the crystalline domains of the spherulites is normal to the radius vector. X-ray diffraction studies [Goderis et al., 1999] have shown that the crystalline structures are organized in lamellae, approximately $\approx$ 10 nm thick. These lamellae are crystalline domains originating from a nucleation center and separated by an amorphous phase, constituting the spherulites (refer to the left scheme in Figure 2.1).

2.1.2 Lamellar structure, long period and incomplete crystallization

The X-ray diffraction pattern provides valuable information for measuring the alternation between the amorphous and crystalline phases, known as the *long period* L_P. Additionally, calorimetric measurements estimate the thickness of the crystalline lamellae m [Goderis

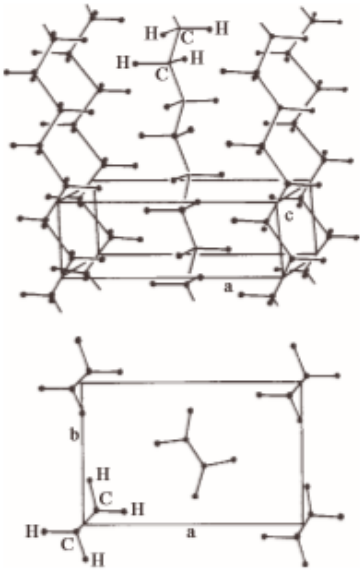

Figure 2.4: *Orthorombic polyethylene crystalline cell, space group Pnma (*$a = 0.740\,\text{nm}$*,* $b = 0.493\,\text{nm}$ *and* $c = 0.253\,\text{nm}$*). The density is* $1.003\,\text{g/cm}^3$ *[Bunn, 1939].*

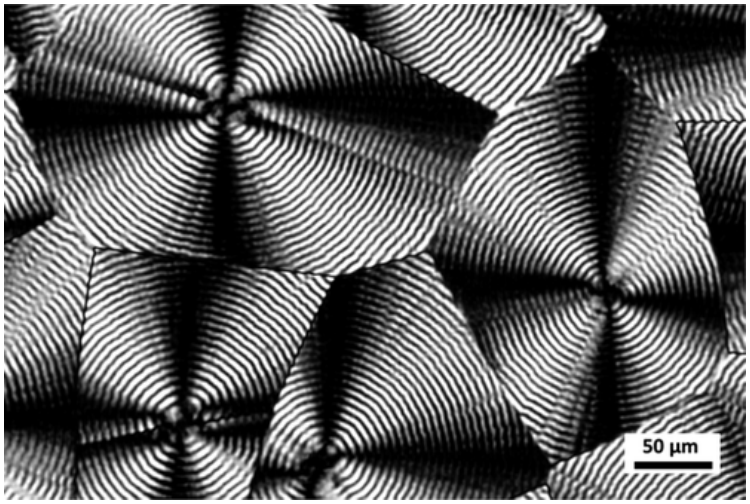

Figure 2.5: *Typical appearance of banded spherulites of polyethylene in the polarizing microscope [Lovinger, 2020].*

et al., 1999, Ryan et al., 1994]:

$$L_P = m + d, \tag{2.1}$$

where d represents the thickness of the amorphous phase. The values of L_P and m depend on the crystallization path, such as the cooling rate [Mutter et al., 1993]. The center of Figure 2.1 illustrates the alternation between the amorphous and crystalline phases, with the bold double arrow representing the long period L_P.

The thicknesses can be related to the densities as follows:

$$L_P \rho = m\rho_c + d\rho_a, \tag{2.2}$$

where ρ is the total density of the semicrystalline structure, ρ_c is the density of the crystalline

phase, and ρ_a is the density of the amorphous phase. This relation is an approximation; it implies that the density abruptly changes between the crystalline phase and the amorphous phase. In reality, a continuous transition exists.

Another important characterization parameter is the degree of crystallinity, which represents the mass or volumic ratio of the crystalline phase to the total semicrystalline material:

$$\chi_c = \frac{W_c}{W_{\text{total}}}, \tag{2.3}$$

$$\phi_c = \frac{V_c}{V_{\text{total}}}, \tag{2.4}$$

where χ_c (ϕ_c) is the massic (volumic) degree of crystallinity, W_c (V_c) is the mass (volume) of the crystalline phase, and W_{total} (V_{total}) is the total weight (volume) of the semicrystalline material.

Reciprocally, we also define the massic (or volumic) amorphous fraction.

$$\chi_a = 1 - \chi_c \tag{2.5}$$

$$\phi_a = 1 - \phi_c \tag{2.6}$$

The two quantities, which will be useful in the following, are the crystallinity degree χ_c, and the amorphous fraction ϕ_a.

Incomplete crystallization occurs because in the molten state, polymers are randomly oriented, leading to multiple chain entanglements. The growth of crystallites is faster than the resolution of entanglements. Eventually, the density of entanglements in the amorphous phase reaches a maximum, impeding further crystalline growth [Flory and Yoon, 1978].

2.1.3 Loss of order from the crystalline phase to the amorphous phase, controversy about the path of a single chain and tilt angle

2.1.3.1 Experimental studies

In pure crystalline polyethylene, which can be obtained by rapidly cooling polyethylene in a solution, it was quickly recognized that the chains located at the edges of the crystallite primarily fold towards the adjacent stems. These folding patterns are referred to as *adjacent reentries*, and the folding model is known as *the adjacent reentry folding model* [Spells and Sadler, 1984] (see Figure 2.6). The compact folding of the chains in pure crystalline polyethylene was demonstrated by measuring the radius of gyration of deuterated chains, which was significantly smaller compared to the chains in the molten state. This smaller radius of gyration indicates the necessity for a compact folding of the chains within the crystalline structure, i.e *adjacent reentries*. More recent research has quantified the fraction of adjacent reentry folds in various pure crystalline polymers, revealing that it typically ranges from 91% to 95% [Ma et al., 2019].
In the semicrystalline structure, the folding models at the edges of the crystalline lamellae have been a subject of prolonged and ongoing debate. In the 1970s, the trajectory of a single deuterated polyethylene chain in the semicrystalline structure, obtained by rapidly quenching from the melt, was investigated using neutron scattering (NS) techniques [Schelten et al., 1976, Schelten et al., 1977, Sadler and Keller, 1977, Stamm et al., 1979]. The

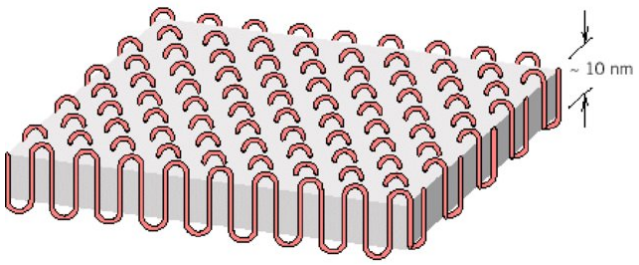

Figure 2.6: *Scheme of an adjacent reentry folding model in a pure crystalline polymer[Abdou, 2015].*

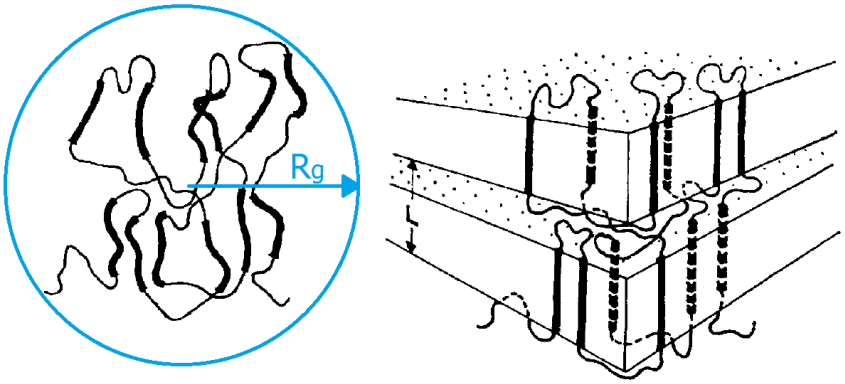

Figure 2.7: *Left: Scheme of a polymer chain in the melt with a radius of gyration R_g. Right: Polymer chain in the semicrystalline structure keeping the same radius of gyration, here the crystalline chains are orthogonal with the interface [Stamm et al., 1979].*

studies revealed that the radius of gyration of the polymer in the semicrystalline structure is comparable in length to that in the molten state (see Figure 2.7). This finding suggests that the overall extension of the polymer molecules is not significantly altered during the crystallization process, leading to the formation of a relatively low proportion of adjacent chain reentries (refer to the center of Figure 2.1 for the definition of adjacent reentry).

Since the 2000s, new techniques have been employed to characterize the morphology of semicrystalline polymers, including atomic force microscopy (AFM) and solid-state nuclear magnetic resonance (ssNMR). The use of isotope labeling in ssNMR allows for the study of a small fraction of the polymer chains. AFM images of semicrystalline films of isotactic poly(methyl methacrylate) [Kumaki et al., 2005] and polyethylene [Mullin and Hobbs, 2011, Savage et al., 2015] have revealed a high proportion of adjacent reentries, in contrast to the findings from NS measurements on semicrystalline materials obtained from the melt. Similarly, ssNMR studies on polypropylene solution-grown single crystals and semicrystalline polypropylene obtained from the melt have also shown a high proportion of adjacent reentries, along with the additional observation that the morphology is less dependent on the kinetic path of crystallization and more influenced by the entanglements in the initial amorphous material [Hong and Miyoshi, 2013, Hong et al., 2016].

It is challenging to draw definitive conclusions about the correct morphology of the folding pattern due to the paradoxical nature of experimental findings. This can be attributed to the diversity of procedures used to prepare polymer samples and the nature of the polymers

under study. For example, AFM studies often require specific samples such as stretched polymer films during the cooling process, which may lead to a higher proportion of observed adjacent reentries. On the other hand, the measurements conducted by Stamm et al. in the 1970s utilized deuterated chains. To prevent phase separation between deuterated and non-deuterated chains, quenching is needed. This approach may have hindered strong reorganization and favored a less compact folding model.

2.1.3.2 Theoretical treatment

In an effort to address the controversy, Flory, Yoon, and Dill published two articles in 1984 proposing a theoretical treatment. In their initial paper, they considered chains emanating normally from the interface and wrote [Flory et al., 1984]:

> The flux of chains emanating from 001 face of the crystal is large; it may reach the maximum that spatial requirements of the chains will allow (if the conformation in the crystal and the crystal dictate). This flux must be diminished substantially as a necessary prerequisite for attainment of random disorder. The mere requirement of isotropy of the distribution of bond directions necessitates a reduction of the surface density of chains by a factor of one-half if the chains in the crystal are normal to the interface and if the difference in densities of the phases is ignored.

Based on these assumptions, Flory, Yoon, and Dill reached the conclusion that a minimum of 70% of the chains emanating from the crystal exhibit an *adjacent reentry* behavior. In a subsequent article published in the same year [Yoon and Flory, 1984], Yoon and Flory demonstrated that the presence of a tilt angle (depicted in the central schematic of Figure 2.1, where the crystalline stems form an angle, known as the tilt angle, with the interface normal) weakens the necessity for adjacent reentries in order to dissipate the flux of emerging chains. An easy way to undertand that, is that in a Pythagoras triangle, the adjacent sides, are alway smaller than the hypothenuse. As the tilt angle increases, the same number of chains emerge at the interphase, but they do so over a larger surface area. In this model, the polymer chains emerge from the (201) polyethylene crystalline plane:

> The reduction of surface chain density in lamellar semicrystalline polymers due to tilting of the interfacial plane from orthogonality to the chain sequences within the crystal allows the incidence of adjacent folds to diminish markedly; it may become negligible for a tilt angle $> 25°$.

In semicrystalline polyethylene, the tilt angles have been evaluated to be approximately $\approx 35°$ on average [Keller, 1961, Bassett et al., 1981, Bassett et al., 1963a, Bassett et al., 1963b, Cowking et al., 1968, Voigt-Martin et al., 1980, Voigt-Martin et al., 1989], reaching up to $60°$ with high molecular weight polymers [Peterlin, 1980, Frank, 1979, Hay and Keller, 1967, Point et al., 1969, Alamo et al., 1992]. Building on the approach of Yoon and Flory, Fritzsching *et al.* in a recent study further refined the understanding of how the surface density of polymers emerging from the crystalline phase dissipates and avoids density anomalies in the interphase, which is the region where the dissipation of order occurs between the crystalline and amorphous phases [Fritzsching et al., 2017]. This study also considered the fact that the center of the isotropic amorphous phase has a lower density ($0.85\,\mathrm{g\,cm^{-3}}$) compared to the $1.0\,\mathrm{g\,cm^{-3}}$ density of the crystalline phase, necessitating even more density dissipation in the interphase. According to their findings, the avoidance

of density anomalies is attributed to the tilt angle, the presence of free chains with their chain ends in the interphase, and a low proportion of adjacent reentries. With high molecular weight chains, there are fewer chain ends, allowing for the observation of large tilt angles up to $60°$.

Most theoretical models assume a regular and planar interface, but the presence of surface roughness could potentially aid in dissipating chain surface density as well as volumetric density. The rough patterns observed in AFM studies support this notion [Savage et al., 2015].

In conclusion, it appears that there are various mechanisms in nature to accommodate the dissipation of order, the necessary dissipation of chain surface density to achieve isotropic polymer paths, and the gradual decrease in mass density toward the amorphous phase. In 1979, Volume 68 of the *Faraday Discussions of the Chemical Society* [Keller, 1979] was largely dedicated to the controversy between the proponents of the *switchboard models* with very few adjacent reentries and the opposing *adjacent reentry folding models*. The issue was the subject of a heated debate among the founding figures of the field, such as Keller, Flory, and Sadler. However, it seems that the controversy has dissipated over time. There is no definitive answer; it appears that the preparation of the sample, the length of the polymer chain, and the number of entanglements in the melt will tilt the balance toward one model or the other.

The interphase between the crystalline and amorphous regions has been observed through Raman spectroscopy, which requires the inclusion of three distinct phases in spectral decompositions [Mutter et al., 1993, Strobl and Hagedorn, 1978], as well as through NMR, with a separation of molecular degrees of freedom between the amorphous phase and the interphase [Bergmann, 1978]. Experimental estimates suggest that the thickness of the interphase ranges from approximately 0.8 nm to 3.4 nm.

2.1.4 Characterization of the amorphous chain sections: chain section types and trapped entanglements

2.1.4.1 Type of chain sections in the amorphous phase

As discussed previously, there is an ongoing debate regarding the folding patterns at the edge of the crystalline phase in the interphase, highlighting the variety of folding patterns allowed by nature.

Moving into the amorphous phase, another important aspect used to characterize it is the type of chains that either bound or do not bound the crystalline lamellae.

In the semicrystalline structure, the same chain travels through both the crystalline domains and the amorphous phases, as depicted in the central scheme of Figure 2.1.

Taking the example of the chain shown in the central scheme of Figure 2.1, we observe that it starts its path in the bottom-left region of the scheme, within the bottom amorphous phase, forming what is referred to as a *free chain* or a *tail* in this context. The chain then enters the gray crystalline lamella, adopting a crystalline zig-zag conformation (for polyethylene), represented by a bold segment. As mentioned earlier, the chain enters the lamella at an angle relative to the normal of the crystalline edge. It then emerges from the crystalline lamellae, depicted by green lines, forming what is known as a *bridge* or a *tie chain* in the literature, connecting the two crystalline lamellae. Upon reentering the

top crystalline lamella, the chain again emerges from it, creating a *loop* within the same lamella. This pattern is repeated twice. The final reentry, highlighted in red, represents an *adjacent reentry*, which is the smallest possible loop where two adjacent crystalline stems are bound together by the shortest chain section in the interphase. Another *loop* is then formed in the top-right region of the top crystalline lamella. Finally, the chain crosses the central amorphous phase once again, forming a last *tie chain* before concluding its path in the bottom amorphous phase as a *tail*. It should be noted that other chain types are possible but were not considered in this work. For instance, a chain can terminate within the crystalline phase, creating a crystalline defect.

2.1.4.2 Entanglements

In addition to the descriptions of amorphous chain types, as explained earlier, the hinderance of complete crystallization arises from the presence of entanglements, which require more time to be resolved than the time needed for crystallization to occur. The entanglements trapped in the amorphous phase are referred to as *trapped entanglements*. These *trapped entanglements* can have different types depending on the involved chain sections. Examples include *loop-loop entanglements*, *tie-tie entanglements*, *tie-loop entanglements*, *tail-tie entanglements*, and so on.

Furthermore, the description can be further refined by introducing the notion of *bridging entanglements*, which involve entanglements composed of chain types emerging from different lamellae. For instance, *loop-loop bridging entanglements* connect two different lamellae through an entanglement.

2.1.4.3 Stress transmitters and elastically active chains

The characterization of chain types and trapped entanglements is crucial for understanding the mechanical properties of semicrystalline materials. Specifically, *tie chains* and *loop-loop bridging entanglements* are believed to play a significant role as *stress transmitters* when the semicrystalline structure is subjected to strain. This hypothesis was suggested by Humbert *et al.* [Humbert et al., 2009, Humbert et al., 2010] and Huang and Brown [Huang and Brown, 1991].

Similarly, in the context of transport properties, Memari, Lachet, and Rousseau [Memari et al., 2015] proposed that *elastically active chains*, which consist of tightly bound *bridging entanglements* and *tie chains*, impose additional constraints on the amorphous phase and limit the solubility of penetrants.

2.2 Review of the literature of semicrystalline model building at the molecular scale

2.2.1 Direct nucleation from the melt with molecular dynamics

Molecular modeling techniques, such as molecular dynamics, have been utilized to simulate nucleation processes from the melt [Esselink et al., 1994, Takeuchi, 1998, Yi and

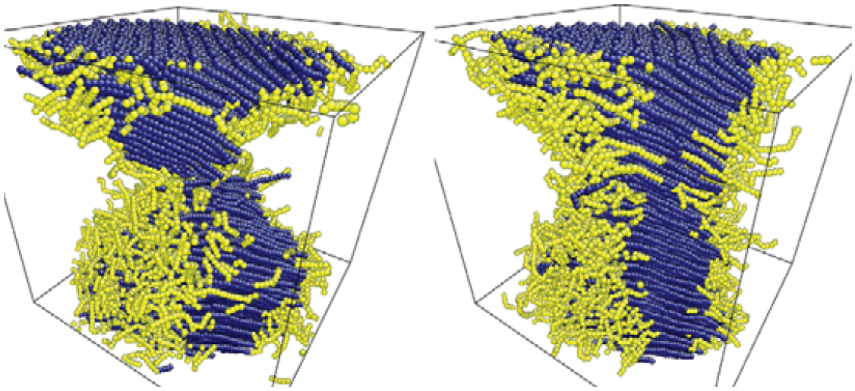

Figure 2.8: *Example of a direct nucleation study of polyethylene from the melt [Sommer and Luo, 2010].*

Rutledge, 2009, Yi and Rutledge, 2011, Yi et al., 2013, Zhang and Larson, 2018, Koyama et al., 2002, Lavine et al., 2003, Ko et al., 2004, Jabbarzadeh and Tanner, 2009, Kavassalis and Sundararajan, 1993, Liu and Muthukumar, 1998, Hu, 2001, Meyer and Müller-Plathe, 2002, Yamamoto, 2008, Yamamoto, 2010]. These simulations provide valuable insights into the molecular-scale mechanisms of nucleation and aid in understanding the chain folding patterns within the crystallites. However, direct observation of nucleation events using molecular dynamics is challenging due to the rarity and anisotropic nature of homogeneous nucleation, which requires the simultaneous creation of a surface normal to the chain direction and the lateral stacking of parallel chains[Yi et al., 2013].

To overcome these challenges, simulations are often biased to accelerate the formation of a nucleus large enough to survive and grow within a reasonable simulation time. Biases can include the use of super-cooled short chains [Esselink et al., 1994, Takeuchi, 1998, Yi and Rutledge, 2009, Yi and Rutledge, 2011, Yi et al., 2013, Zhang and Larson, 2018], pre-oriented chains [Koyama et al., 2002, Lavine et al., 2003, Ko et al., 2004, Jabbarzadeh and Tanner, 2009], or artificially stiffened chains [Kavassalis and Sundararajan, 1993, Liu and Muthukumar, 1998]. Coarse-graining techniques [Hu, 2001, Meyer and Müller-Plathe, 2002, Yamamoto, 2008, Yamamoto, 2010, Jabbari-Farouji et al., 2017] have also been employed to accelerate simulations.

However, it should be noted that due to the small size of the simulation boxes (approximately 100 Å), the characteristic lamellar structure observed in experimental studies, characterized by the regular alternation of crystalline and amorphous phases (as depicted in the middle image of Figure 2.1), may not fully emerge in these simulations (Figure 2.8 exemplifies the kind of structure resulting from direct nucleation). Consequently, the obtained systems are often inadequate for property calculations.

As a result, simulation boxes are commonly constructed directly with a predetermined semicrystalline structure, and various procedures proposed in the literature will be discussed in the following sections.

2.2.2 The Interphase Monte Carlo Method (Rutledge model)

Since 1998, the Rutledge group at MIT has proposed a method for modeling semicrystalline structures known as the *Interphase Monte Carlo Method* [Balijepalli and Rutledge, 1998, Gautam et al., 2000, Balijepalli and Rutledge, 2000, Rutledge, 2002, in 't Veld and Rutledge,

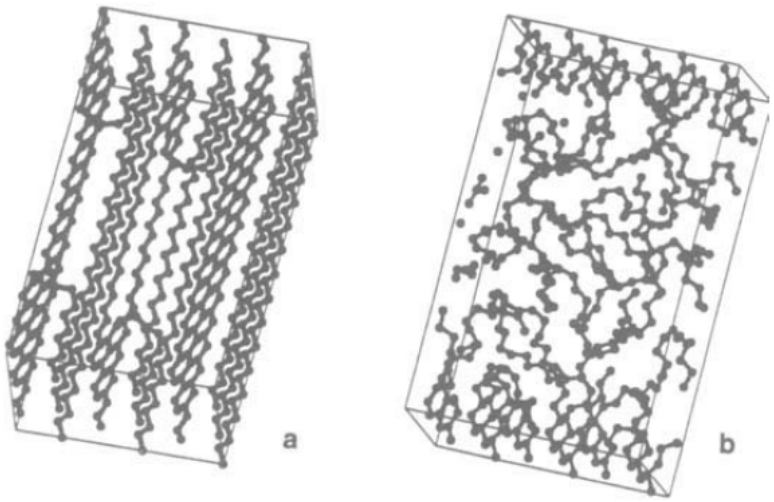

Figure 2.9: *Scheme explaining the Rutledge model. The left scheme is the initial simulation box, a pure crystal with randomly deleted chain sections in the center of the crystal to target the amorphous density. The right scheme is the simulation box after Monte-Carlo steps of connection, slicing bonds and displacement moves.*

2003, in't Veld et al., 2006] hereafter referred to as the Rutledge model.

This method begins with a cuboid-shaped pure crystal. In the central section of the cuboid, which is intended to represent the amorphous phase, monomers or entire chain sections are removed to achieve the desired density for the amorphous region. Subsequently, a Monte Carlo procedure is employed within this central section, involving slicing chain bonds, connecting chain ends, and employing classic displacement-type moves for the chains. Meanwhile, the remaining atoms are kept frozen.

The Rutledge model incorporates two main constraints: the target density and the interlamellar distance. To satisfy these constraints, the atoms at the lower and upper ends are kept frozen (refer to Figure 2.9).

The Rutledge group has developed simulation models that incorporate both crystalline stems orthogonal to the interface and stems with a tilt angle. Similar to the findings of Flory (see Section 2.1.3), a lower proportion of *adjacent reentries* is observed when the tilt angle is non-zero compared to when it is zero. The energetically optimal tilt angle corresponds to an interface aligned along the 201 crystalline plane, and the Rutledge Monte Carlo procedure achieves a fraction of *adjacent reentries* ranging from 20-30% in this case. Local stress analysis indicates that this tilt angle reduces interfacial energy [Hütter et al., 2006, Rutledge, 2002].

A distinctive characteristic of Rutledge models is the low number of tie chains. In Rutledge systems, the majority of chain sections consist of loops [Kim et al., 2014, Yeh et al., 2015]. However, in real systems, where the gyration radius exceeds the long period L_p, a higher number of tie chains is expected.

The hindered complete crystallization is believed to be due to entanglements, as discussed earlier. The topological reorganization facilitated by the Monte Carlo connections and disconnections resolves many entanglements, overcoming steric hindrance and leading to energetically favorable conformations. Consequently, the Rutledge model explores energeti-

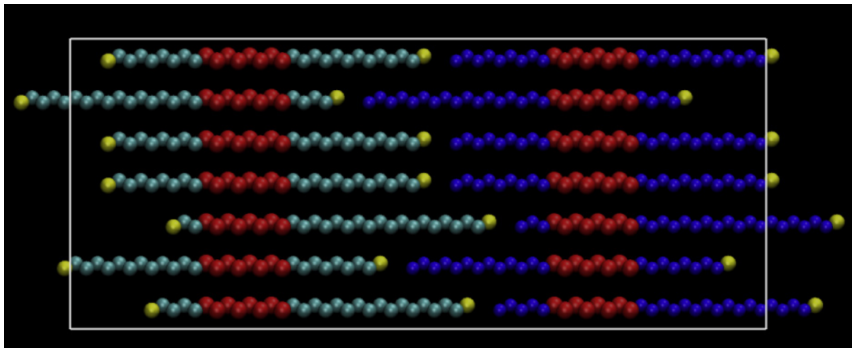

Figure 2.10: *Scheme of the chains in the initial condition in the Pandiyan and Rousseau connection method. The blue chains are then melted and a connection algorithm connects chain when falling within a cut-off radius [Pandiyan and Rousseau, 2013].*

cally favorable conformations of the amorphous phase, favoring the presence of *adjacent reentries*.

2.2.3 The Monte Carlo random walk method (Nilsson's model)

More recently, Nilsson *et al.* proposed an alternative approach for constructing semicrystalline polymer models[Nilsson et al., 2012, Moyassari et al., 2015].

This method utilizes a random walk technique between two crystallites, where upon reaching a crystallite, the chain automatically connects to a crystalline stem. Chains emerge from the lamellae and can either fold back adjacently or initiate a random walk, resulting in the formation of loops or tie chains (refer to Figure 2.1 for definitions). The target density of the amorphous phase is achieved by controlling the probability of direct adjacent reentry.

Both the Nilsson and Rutledge methods employ the amorphous phase density as a controlling parameter, coupled with either random walks or a Monte Carlo connection algorithm.

2.2.4 Pandiyan and Rousseau connection method

Pandiyan and Rousseau [Pandiyan and Rousseau, 2013] proposed a different approach, starting with a pure crystalline sample and randomly cutting each chain in a central region. This is followed by a relaxation process above the melting temperature to create an amorphous region, while keeping two crystalline areas frozen (refer to Figure 2.10). During a subsequent relaxation step, two chain ends are connected, forming a chemical bond if they fall within a specified cutoff distance. The acceptance or rejection of these connections is determined by the input fractions of polymer section types.

This method enables the investigation of the role of each type of walk (tie chains, loops, and tails) by controlling their relative fractions [Pandiyan and Rousseau, 2013].

2.2.5 Monasse and Queyroy method

Starting with information about the morphology instead of starting with the density as the controlling parameter was also proposed by Monasse and Queyroy [Monasse et al., 2008, Queyroy and Monasse, 2012].

In their work, they deliberately selected specific reference systems characterized by predefined morphological attributes, including degrees of crystallinity and connection patterns (encompassing tails, tie chains, and loops), alongside amorphous section lengths. These systems were meticulously manually built.

Although this technique demands a considerable investment of time, it affords unparalleled precision in regulating the proportions of different chain section types and the distribution of their respective lengths.

2.2.6 Discussion on the different semicrystalline modeling methods: advantages and disadvantages

Nilsson's and Rutledge's methods lack control over morphologies. Nilsson *Monte Carlo random walk model* heavily relies on a high proportion of adjacent reentries to achieve the experimental density of the amorphous phase, which is a contentious choice when considering the experimental literature.

Rutledge model favors structures predominantly composed of loops and aims to create the most energetically stable amorphous phases through topological reorganization.

In Pandiyan and Rousseau work [Pandiyan and Rousseau, 2013], attempts were made to control the fraction of different chain section types, but the connection procedure was not efficient enough, resulting in a high number of unconnected chains and unrealistic polydispersity in molecular weights.

Monasse and Queyroy construction method is tedious and requires prior knowledge of all morphological traits, making it inconvenient for systematic studies of semicrystalline samples. However, it offers the advantage, similar to Pandiyan and Rousseau method, of providing control over the amorphous morphology.

When seeking a building method suitable for examining the relationship between morphology and physico-chemical properties, three main criteria have been identified:

- The method should be automated or capable of generating multiple cells within a limited timeframe.
- Some degree of control over morphologies is necessary.
- The method should possess inherent randomness to generate different models with the same morphological characteristics as inputs.

2.3 Mechanical properties of semicrystalline polymers

To characterize strain in materials, the main criterion is their ability to resist a distorting constraint and return to their original size and shape when the strain or force is removed. When a material can regain its initial shape and size for a given strain, it is said to be within its elastic domain. In this small strain regime, the strain-stress relationship is described by Hooke's law:

$$\sigma = E\epsilon \tag{2.7}$$

where σ and ϵ represent the internal stress and strain, respectively. Hooke's law applies to directional normal stress. For shear stress, a similar relationship can be expressed as:

$$\theta = G\tau \tag{2.8}$$

where θ and τ represent the equivalent quantities for shear stress and strain. Here, E and G are the Young's modulus and the shear modulus, respectively. Beyond the elastic domain, when the strain is too high, the deformation is called plastic.

2.3.1 Experimental mechanical properties of polyethylene

The typical stress-strain behavior of a semicrystalline polymer is depicted in Figure 2.11. In Domain I, the material exhibits elastic behavior, meaning it can recover its original shape and size. The stress-strain curve in this region follows the equation 2.7. The slope of the curve represents the Young's modulus, denoted as E. The Young's modulus can vary depending on factors such as crystallinity, molecular weight, and processing conditions [Jordan et al., 2021]. For example, low-density polyethylene (LDPE), which has a low degree of crystallinity, typically has a Young's modulus ranging from 50 to $400\,\mathrm{MPa}$ [ASTMD-638-14, 2014]. On the other hand, high-density polyethylene (HDPE) exhibits a higher Young's modulus, ranging from 800 to $3000\,\mathrm{MPa}$ [Jordan et al., 2021].

Domain II begins at the end of the elastic region after a yield value, denoted as σ_Y, typically falling within the range of 10 to $40\,\mathrm{MPa}$ according to measures compiled by ASTM International [ASTMD882-18, 2018], respectively for LDPE and HDPE. The yield value occurs at $8.8\,\%$ for HDPE and $10.0\,\%$ for LDPE. In this domain, the material undergoes plastic deformation, spherulitic structures are still present.

In Domain III, the material experiences further deformation as molecules align in the direction of strain, forming fibrils. Spherulites are destroyed, and the amorphous regions undergo bond breakage, leading to the formation of cavities. Ultimately, failure occurs at a rupture stress also called tensile strength denoted as σ_R, typically ranging from 23.5 to $47.4\,\mathrm{MPa}$ from the same data provided by ASTM International [ASTMD882-18, 2018].

The shear modulus G is strongly influenced by temperature and shear rate. At a temperature of 20 °C, the shear modulus can range from 1 to $6\,\mathrm{GPa}$ [Nielsen, 1954].

2.3.2 Anisotropy of the elasticity at the microscopic scale

As discussed in Section 2.1, at the scale of the long period, the structures of semicrystalline materials exhibit high anisotropy. Therefore, it is necessary to introduce generalized Hooke's laws that account for directional strain and stress tensors. The Voigt notation

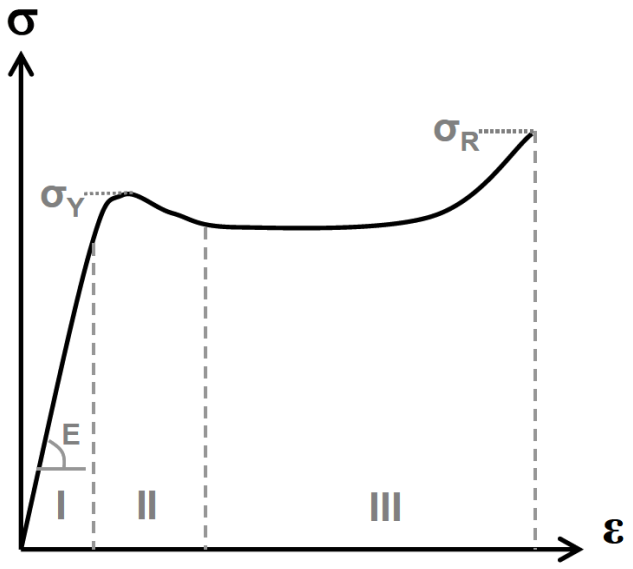

Figure 2.11: *Stress and strain curve of a semicrystalline polymer. The stress is uniaxial and the engineering strain ϵ is defined as $\frac{l-l_0}{l_0}$ where l_0 is the intial length of the sample [Seignobos, 2009].*

provides a compact representation of the elastic constants, which is convenient for calculations. In this section, we will provide a brief introduction to the generalized Hooke's law.

In a material at equilibrium, the internal stress tensor, denoted as $\sigma_{\alpha\beta}$, represents the opposite of the applied force per unit area acting on a face of the material (see Figure 2.12).

$$\sigma_{\alpha\beta} = -\frac{1}{s_\beta} f^\alpha \tag{2.9}$$

with a force f^α of direction α applied on the face which has as a normal β. We can write the generalized Hook law:

$$\sigma_{\alpha\beta} = C_{\alpha\beta\mu\nu}\epsilon_{\mu\nu} \tag{2.10}$$

where elastic constants $C_{\alpha\beta\mu\nu}$ are a rank 4 tensor. The stress and strain tensors symmetry ($\sigma_{\alpha\beta} = \sigma_{\beta\alpha}$ and $\epsilon_{\alpha\beta} = \epsilon_{\beta\alpha}$) and the generalized Hooke's laws imply that $C_{\alpha\beta\mu\nu} = C_{\beta\alpha\mu\nu} = C_{\alpha\beta\nu\mu} = C_{\beta\alpha\nu\mu}$. These symmetries reduce the number of elements of stress and strain tensors from 9 to 6 and the number of elastic constants from 81 to 36. Moreover, the stress-strain relation can be derived from a strain energy (U) :

$$\sigma_{\alpha\beta} = \frac{\partial U}{\partial \epsilon_{\alpha\beta}} \implies C_{\alpha\beta\mu\nu} = \frac{\partial^2 U}{\partial \epsilon_{\alpha\beta}\partial \epsilon_{\mu\nu}} \tag{2.11}$$

Maxwell relations on thermodynamic potentials tell us that the order of differentiation does not change the value of the derivative so : $C_{\alpha\beta\mu\nu} = C_{\mu\nu\alpha\beta}$. That reduces again the number of elastic constants for the stiffness tensor from 36 to 21. With those simplifications:

$$\begin{pmatrix} \sigma_{11} & \sigma_{12} & \sigma_{13} \\ \sigma_{21} & \sigma_{22} & \sigma_{23} \\ \sigma_{31} & \sigma_{32} & \sigma_{33} \end{pmatrix} = \begin{pmatrix} \sigma_{11} & \sigma_{12} & \sigma_{13} \\ \sigma_{12} & \sigma_{22} & \sigma_{23} \\ \sigma_{13} & \sigma_{23} & \sigma_{33} \end{pmatrix} = \begin{pmatrix} \sigma_{11} \\ \sigma_{22} \\ \sigma_{33} \\ \sigma_{23} \\ \sigma_{13} \\ \sigma_{12} \end{pmatrix} = \begin{pmatrix} \sigma_1 \\ \sigma_2 \\ \sigma_3 \\ \sigma_4 \\ \sigma_5 \\ \sigma_6 \end{pmatrix} \tag{2.12}$$

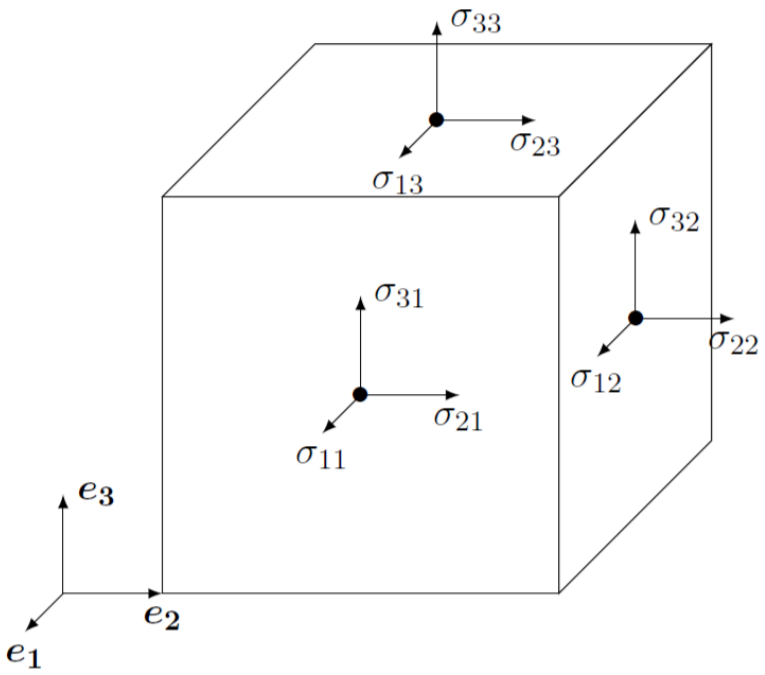

Figure 2.12: *Representation of the elementary volume in the $\{e_1, e_2, e_3\}$ frame where the tensors elements are shown on their face. Figure extracted from [Clavier, 2018]*

$$\begin{pmatrix} \epsilon_{11} & \epsilon_{12} & \epsilon_{13} \\ \epsilon_{21} & \epsilon_{22} & \epsilon_{23} \\ \epsilon_{31} & \epsilon_{32} & \epsilon_{33} \end{pmatrix} = \begin{pmatrix} \epsilon_{11} & \epsilon_{12} & \epsilon_{13} \\ \epsilon_{12} & \epsilon_{22} & \epsilon_{23} \\ \epsilon_{13} & \epsilon_{23} & \epsilon_{33} \end{pmatrix} = \begin{pmatrix} \epsilon_{11} \\ \epsilon_{22} \\ \epsilon_{33} \\ 2\epsilon_{23} \\ 2\epsilon_{13} \\ 2\epsilon_{12} \end{pmatrix} = \begin{pmatrix} \epsilon_1 \\ \epsilon_2 \\ \epsilon_3 \\ \epsilon_4 \\ \epsilon_5 \\ \epsilon_6 \end{pmatrix} \tag{2.13}$$

The factor 2 appearing in equation (2.13) is mandatory to keep the equation (2.10) true. Reference [L.D. Landau & E.M. Lifshitz, 1970] is available to provide exhaustive details.

$$\begin{pmatrix} \sigma_1 \\ \sigma_2 \\ \sigma_3 \\ \sigma_4 \\ \sigma_5 \\ \sigma_6 \end{pmatrix} = \begin{pmatrix} c_{11} & c_{12} & c_{13} & c_{14} & c_{15} & c_{16} \\ c_{21} & c_{22} & c_{23} & c_{24} & c_{25} & c_{26} \\ c_{31} & c_{32} & c_{33} & c_{34} & c_{35} & c_{36} \\ c_{41} & c_{42} & c_{43} & c_{44} & c_{45} & c_{46} \\ c_{51} & c_{52} & c_{53} & c_{54} & c_{55} & c_{56} \\ c_{61} & c_{62} & c_{63} & c_{64} & c_{65} & c_{66} \end{pmatrix} \begin{pmatrix} \epsilon_1 \\ \epsilon_2 \\ \epsilon_3 \\ \epsilon_4 \\ \epsilon_5 \\ \epsilon_6 \end{pmatrix} \tag{2.14}$$

In the case of an orthotropic material like crystalline polyethylene, the material has three planes of symmetry and is characterized by 9 coefficients.

$$\begin{pmatrix}\sigma_1\\ \sigma_2\\ \sigma_3\\ \sigma_4\\ \sigma_5\\ \sigma_6\end{pmatrix} = \begin{pmatrix}c_{11} & c_{12} & c_{13} & 0 & 0 & 0\\ c_{12} & c_{22} & c_{23} & 0 & 0 & 0\\ c_{13} & c_{23} & c_{33} & 0 & 0 & 0\\ 0 & 0 & 0 & c_{44} & 0 & 0\\ 0 & 0 & 0 & 0 & c_{55} & 0\\ 0 & 0 & 0 & 0 & 0 & c_{66}\end{pmatrix} \begin{pmatrix}\epsilon_1\\ \epsilon_2\\ \epsilon_3\\ \epsilon_4\\ \epsilon_5\\ \epsilon_6\end{pmatrix} \tag{2.15}$$

2.3.2.1 Elastic properties measured on the polyethylene pure crystalline phase

The crystalline phase, depicted in Figure 2.4, exhibits distinct anisotropic characteristics. The alignment of the crystal backbone predominantly follows the c axis, driven by covalent interactions, while the a and b axes experience strain resistance mainly through weaker non-covalent interactions.

Empirical investigations have yielded elastic coefficients of 3.2 GPa and 3.9 GPa (corresponding to c_{11} and c_{22}, respectively) along the a and b axes [Sakurada et al., 1964]. For the chain axis along the c direction, the coefficient c_{33} has been theoretically computed at 288 GPa in [Tashiro et al., 1978a, Tashiro et al., 1978b]. The most precise measurement, as determined from X-ray analysis by Nakamae *et al.*, establishes $c_{33} = 235$ GPa [Nakamae et al., 1991].

2.3.2.2 Elastic coefficients measured on ultra-drawn polyethylene

A suitable model for capturing the anisotropic elastic properties of semicrystalline polymers at the hundred of nanometers scale, the long period scale (as shown at the center of Figure 2.1), is provided by ultra-drawn polyethylene films. These films are produced by stretching the polymer melt in a single direction after it has been cooled from the molten state.

This process yields a structure different from the typical spherulite formation (as depicted on the left side of Figure 2.1). In ultra-drawn films, the crystalline phases are all oriented in a uniform direction, as demonstrated in Figure 2.13.

By measuring the elastic coefficients of ultra-drawn films, valuable insights can be gained into the elastic coefficients of the local semicrystalline structure, which consists of parallel crystalline lamellae separated by an amorphous phase. The elastic coefficient tensor is presented in Table 2.1.

c_{11}	c_{22}	c_{33}	c_{12}	c_{13}	c_{23}	c_{44}	c_{55}	c_{66}
7	7	81	3.8	4.7	3.8	1.6	1.6	1.6

Table 2.1: *Elastic coefficients of an ultra-drawn polymer film according to Choy et al. [Choy and Leung, 1985] in GPa.*

2.3.2.3 Elastic coefficients computed by molecular simulation on semicrystalline structures

The main group who directly computed the elastic coefficient tensor from molecular simulation with samples representing both the crystalline and amorphous phases like the one

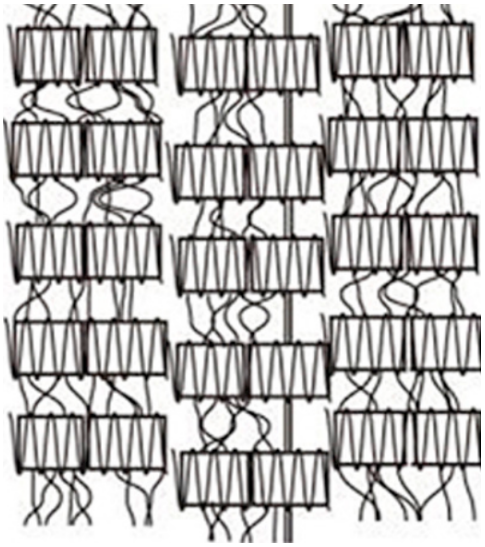

Figure 2.13: *Scheme of an ultra-drawn polyethylene extracted from [Wang et al., 2017].*

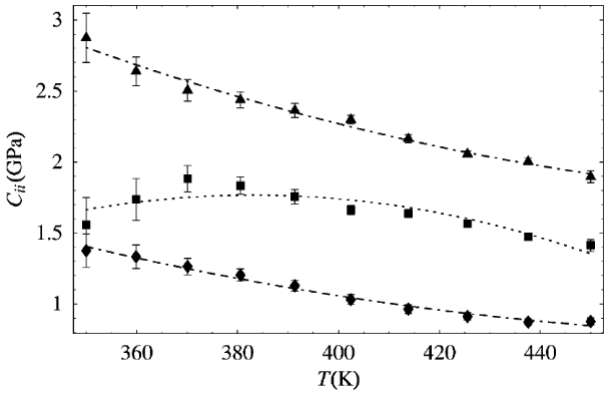

Figure 2.14: *Diagonal elastic coefficients of the non-crystalline part of the semicrystalline models computed by in't Veld* et al. *[in't Veld et al., 2006](c_{11}: squares; c_{22}: triangles, c_{33}: diamonds).*

on the right of Figure 2.9 is the Rutledge group [in't Veld et al., 2006].
It is not clear why in't Veld *et al.* computed the stress tensors using only the stress on the atoms in the non-crystalline phase. It is interesting to notice that the non-crystalline domain is less rigid in the c direction (see Figure 2.14).

2.3.3 Molecular simulation of the plastic deformation, beyond the elastic domain

Queyroy and Monasse [Monasse et al., 2008, Queyroy and Monasse, 2012], as well as the Rutledge group [Olsson et al., 2018, Ranganathan et al., 2020], have extensively investigated plastic deformation in semicrystalline polymers. Simulating plastic deformation is crucial for studying the effects of different chain types, entanglements, and crystallinity on the structural rigidity beyond the elastic regime.

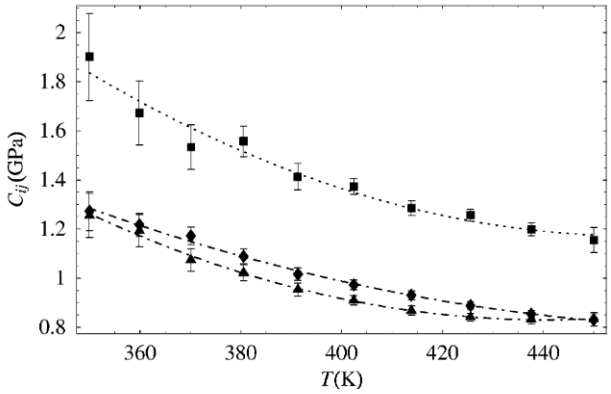

Figure 2.15: *Non-diagonal elastic coefficients of the non-crystalline part of the semicrystalline models computed by in't Veld* et al.*[in't Veld et al., 2006](c_{12}: squares; c_{13}: triangles, c_{23}: diamonds)*

However, it is important to note that direct comparisons between simulation results and experimental data are challenging due to the significant difference in strain rates. Molecular modeling typically employs strain speeds at least two orders of magnitude faster than experimental conditions. Another issue is of course the size of the samples, the fact that the entire spherulite is not simulated, as well as the connection between spherulites.

Monasse and Queyroy devised constructions that allow them to control certain aspects of the morphology, such as the fraction of *tie chains* bridging two crystalline lamellae and the distribution of their sizes. Their findings suggest that the fraction of *tie chains* and the degree of crystallinity contribute to an increase in the yield stress.

In a recent study by the Rutledge group [Ranganathan et al., 2020], they were able to adjust the parameters of the *Interphase Monte Carlo* method (introduced in section 2.2.2) to manipulate the quantity of entanglements. Although the Rutledge models have a debated characteristic regarding the connection and disconnection moves in the Monte Carlo steps that can resolve the *trapped entanglements*, they demonstrated that varying the number of Monte Carlo steps in their method and adjusting the temperature, indirectly controls the quantity of *trapped entanglements* as well as the fraction of different chain types (*tie chains*, *loops*, and *tails*). As expected, the increase of tie chains and entanglements rigidify the structures.

The yield mechanism varied with the topology of the structures. Structures with fewer entanglements exhibited a higher probability of melting/recrystallization compared to structures with more entanglements, which deformed with the formation of cavitations.

2.4 Permeability

Permeation refers to the ability of a fluid to pass through a material. Let us consider a membrane with a width l, an area A, and Q as the quantity of penetrant that crosses the membrane during a time interval t. The flux of fluid passing through the membrane per unit time and surface area is denoted by J.

$$J = \frac{Q}{At} \tag{2.16}$$

The diffusion mechanisms are strongly influenced by the interactions between the polymer and solute, as well as the state of the polymer (glassy or rubbery). The relative mobilities of the penetrant and the polymer play a crucial role [Crank, 1979, Rogers, 1985a, Aminabhavi et al., 1988].

In the case of Fickian diffusion, the diffusion speed is slower than the relaxation speed of the polymer. This condition typically holds above the glass-liquid transition temperature T_g. According to the first Fick's law, there exists a proportional relationship between the flux of penetrant and the concentration gradient in the membrane.

$$J = -D\nabla C \tag{2.17}$$

Here, C represents the local concentration of the dissolved gas in the polymer membrane, and D is the diffusion coefficient. The gas concentration in the polymer is related to the pressure P of the fluid phase.

$$C = S(P)P \tag{2.18}$$

In the high-pressure regime, the solubility coefficient $S(P)$ depends on pressure. However, at low pressure, the concentration follows Henry's law, which states that the concentration is proportional to the pressure, and S becomes a constant. To extend the validity of Henry's law, it is possible to use fugacity instead of pressure. At low pressure, gases behave like ideal gases without interparticle interactions, while at higher pressures, interparticle interactions such as Van der Waals or electrostatic forces introduce cohesiveness to the fluid. The fugacity of a real gas is an effective pressure that accounts for the cohesiveness through the chemical equilibrium constant of the gas, reflecting the tendency of gas molecules to stick together. It is equivalent to the pressure of an ideal gas having the same temperature and molar Gibbs free energy as the real gas. The fugacity f has the dimension of pressure, and in the low-pressure regime, $f = P$. Rewriting Henry's law using fugacity, we have:

$$C = Sf \tag{2.19}$$

Combining the last two equations yields:

$$J = -DS\nabla f \tag{2.20}$$

This equation directly provides the flux of penetrants through a membrane based on the pressure (or fugacity) difference on both sides of the membrane. The proportionality factor is called the permeability Pe, defined as:

$$Pe = S \times D \tag{2.21}$$

In this document, the concentration is expressed in terms of mass, specifically the quantity of dissolved gas in grams per $100\,\mathrm{g}$ of polymer ($\mathrm{g}/100\mathrm{g}$). Therefore, the solubility coefficient is expressed in $\mathrm{g}/100\mathrm{g}/\mathrm{MPa}$, and the diffusion coefficient D is expressed in cm^2/s. The permeability coefficient Pe is defined here assuming that S is constant, which only holds in the low-pressure Henry domain. However, the definition remains the same when other behaviors are observed.

2.4.1 Solubilities, sorption modes

In the most general case, the solubility coefficient S depends on temperature, pressure, and concentration. Various classical sorption modes are presented in Table 2.2 [Huggins, 1941, Flory, 1941, Flory, 1942], and the corresponding sorption isotherm curves are shown in Figure 2.16.

Mode	**Henry's law**	
Expr.	$C = SP$	Constant S independent of concentration, and pressure.
Interac.	Polymer-polymer	Weak penetrant-penetrant and penetrant-polymer interaction at low pressure.
Example	Sorption of O2, N2 and H2 in PDMS below 25 atm. [Merkel et al., 2000]	
Mode	**Langmuir**	
Expr	$C = \frac{C'_H bp}{1+bp}$	C'_H is a "hole saturation" constant, and b is a "hole affinity" constant.
Interac.	Penetrant-polymer	Penetrant molecules occupy sites or holes in the polymer until all sites are occupied.
Example	Gas adsorption on solid surfaces described by the Langmuir model and extended models such as solids with microvoids.	
Mode	**Dual Mode**	
Expr.	$C = SP + \frac{C'_H bP}{1+bP}$	Combination of Henry's sorption mode and Langmuir for glassy polymers.
Interac.	Polymer-polymer and penetrant-polymer	One population of molecules dissolved in the polymer following Henry's law and a second population of molecules adsorbed on specific sites under Langmuir mode.
Example	Sorption of low-activity gases, Ar and N_2 in glassy polymers [Bondar et al., 1996]	
Mode	**Flory-Huggins**	
Expr.	$C = K_D \exp(\sigma C) \times P$	The expression is given in the simplified version derived by Suwandi and Stern [Suwandi and Stern, 1973]. K_D is the solubility coefficient in Henry's domain, σ is the constant related to the penetrant-polymer interaction.
Interac.	Penetrant-penetrant	Stronger interactions between the penetrant molecules.
Example	Sorption of condensable gases of relatively high activities in rubbery polymers under high pressure [Flory and Rehner, 2004, Flory, 2004].	
Mode	**BET**	
Expr.	$\frac{1}{v((p_0/p)-1)} = \frac{c_{BET}-1}{v_m c_{BET}} \times \frac{p}{p_0} + \frac{1}{v_m c_{BET}}$	v is the adsorbed volumetric quantity of the penetrant; v_m is the monolayer adsorbed quantity; c_{BET} is the BET constant; p is the partial pressure of the adsorbate, p_0 is the equilibrium vapor pressure.
Interac.	Polymer-penetrant and penetrant-penetrant	The theory extends Langmuir model to multilayer adsorption [Brunauer et al., 1938].
Example	Sorption of water in higly hydrophilic polymers[Hernandez et al., 1992, Hernandez and Gavara, 1994, Hernandez, 1994].	

Table 2.2: *Classical sorption modes, the table is strongly inspired by the equivalent table in the dissertation thesis of T. Hu [Hu, 2021].*

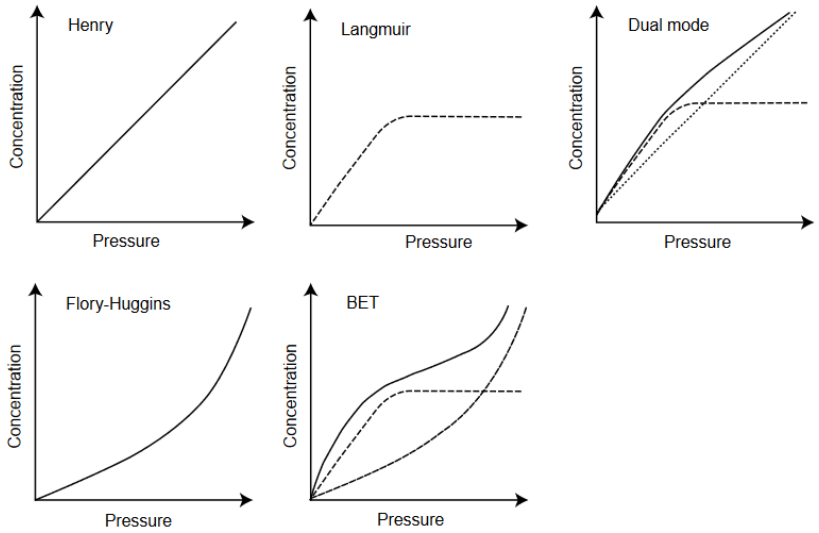

Figure 2.16: *Typical isotherm plots of sorbed concentration versus vapour pressure exctracted from Klopffer* et al. *[Klopffer and Flaconneche, 2001].*

The dual-mode sorption model is commonly used to fit small molecule sorption in polymers, particularly in glassy polymers [Rogers, 1985b, Paul, 2016], as it implies the presence of frozen micro-voids in the amorphous phase.

Our study focuses on the sorption of CH_4 and CO_2 in polyethylene at ambient temperature, spanning from atmospheric pressure to high pressures (40 MPa).

Although polyethylene is non-glassy at ambient temperature ($T_g \approx 195 \pm 10$ K) [Boyer, 1973], the dual-mode sorption model has been reported to effectively represent CH_4 sorption in HDPE [Von Solms et al., 2004].

On the other hand, the Flory-Huggins model is a suitable candidate for describing CO_2 sorption in rubbery polymers, particularly for highly active penetrants like CO_2 due to its intermolecular Coulombic interactions. However, the Flory-Huggins model has two significant limitations. Firstly, it relies heavily on assumptions that undermine its ability to accurately describe experimental data for polymer solutions. Specifically, the model inadequately represents the behavior of diluted solutions due to its assumption of a uniform distribution of polymer segments. Secondly, to effectively describe the isotherms of polymer solutions with high values of χ_c (typically $\chi_c > 0.8$), the Flory-Huggins model requires multiple empirical parameters, which limits its usefulness [Favre et al., 1993, Matteucci et al., 2006].

In contrast, modern equations of state, such as the Sanchez-Lacombe equation of state (EOS) [Sanchez and Lacombe, 1976, Sanchez and Lacombe, 1978], have been found to be more suitable for modeling sorption properties in rubbery polymers.

In most semicrystalline polymers, including polyethylene, the crystalline lamellae are completely impermeable [Rogers et al., 1959]. Typically, solubility coefficient is expressed in terms of solubility coefficient in the amorphous phase S_a:

$$S = \phi_a S_a \tag{2.22}$$

Here, ϕ_a represents the amorphous fraction. This relationship has been verified for differ-

ent types of polyethylene when Henry's law is valid and for temperatures above the glass transition temperature [Michaels and Bixler, 1961b, Michaels and Parker, 1959, Vittoria, 1995].

2.4.2 Diffusivity in semicrystalline polymers

2.4.2.1 Which diffusivity?

Three different diffusion coefficients can be defined: the self-diffusion coefficient D_{self}, the Maxwell-Stefan diffusion coefficient D^{MS}, and the Fick diffusion coefficient D^{F}. The self-diffusion coefficient is obtained from the Einstein relation:

$$\text{msd}(t) = \frac{1}{N}\sum_{i=1}^{N} |\mathbf{r}_i(t) - \mathbf{r}_i(0)|^2 \tag{2.23}$$

$$D = \frac{1}{d}\lim_{t\to\infty}\frac{d}{dt} msd(t) \tag{2.24}$$

where d is the number of directed dimensions (6 in 3D, 4 in 2D), $\frac{d}{dt}$ the time derivative and N is the number of sorbed species.

In the context of permeability and transport properties, the Fickian diffusion coefficient is the one which interests us. What is calculable with molecular dynamics is the self-diffusion coefficient.

In a gas-polymer system, chain mobility is significantly lower than the one of small molecules. The diffusion of polyethylene chains is estimated to be 100 times smaller than that of the sorbed species. By neglecting the average velocity of the chains, Maxwell-Stefan diffusion is reduced to the self-diffusion coefficient [Memari et al., 2015].

It is possible to relate Maxwell-Stefan diffusion to Fickian diffusion using the thermodynamic factor:

$$D^{\text{F}} = QD^{\text{MS}} \tag{2.25}$$

where:

$$Q = \frac{\partial \ln(f/P_0)}{\partial \ln(C)} \tag{2.26}$$

with P_0 as the standard pressure and C as the concentration in g/100g.

In the end, we have:

$$D^{\text{F}} = QD^{\text{self}} \tag{2.27}$$

In the following we use D for the fickian diffusion coefficient.

2.4.2.2 Geometric effect

Diffusivity is not influenced by the degree of crystallinity in the same way the solubility is. Instead, it depends on the concentration of dissolved gas in the amorphous fraction of the semicrystalline polymer. The presence of gas in the polymer matrix can enhance the dynamics of the amorphous chains, acting as plasticizers and reducing the intermolecular

interactions among the amorphous polymer chains [Naito et al., 1996]. However, the diffusivity of gas molecules is impeded by the impermeable crystalline domains. The diffusion coefficient in a semicrystalline structure is proposed to be [Michaels and Parker, 1959]:

$$D = \frac{D_a}{\beta\tau} \tag{2.28}$$

Here, D_a represents the diffusion coefficient in the pure amorphous polymer. The factor β accounts for the reduced mobility of the chains in the amorphous phase of the semicrystalline structure, as they are bound to the crystalline lamellae, compared to a pure amorphous material. The value of β is temperature-dependent. The factor τ is a purely geometric term that considers the longer path gas molecules must travel through the amorphous phase to cross the polymer membrane. In our study, we will explicitly model both the amorphous phase and the crystalline phase at the molecular scale. We will not require the β factor since the binding of amorphous chains to the crystalline phase will be directly modeled in the structure. However, we will still need to account for the tortuosity factor τ:

$$D = \frac{D_{sc}}{\tau} \tag{2.29}$$

Here, D_{sc} represents the diffusion coefficient computed from the molecular-scale semicrystalline model.

Michaels[Michaels and Bixler, 1961a] provides a power law for estimating the tortuosity factor:

$$\tau = \phi_a^{-n} \tag{2.30}$$

where ϕ_a is the volumic amorphous fraction and n is equal to 1.25 for linear polyethylene without branching. He also provides experimental estimation relying on comparison with natural rubber shown on Figure 2.17.

2.4.2.3 Competing effect of plasticizing and pressure

Several studies have examined the influence of pressure on gas transport properties in polyethylene. Flaconnèche et al. [Flaconneche et al., 2001] conducted an investigation and found that the permeability, diffusivity, and solubility coefficient of helium (He) and methane (CH_4) in polyethylene showed minimal variations within the pressure range of 4 to 10 MPa. Similarly, Lundberg [Lundberg, 1964] studied the diffusion of methane in linear polyethylene at different temperatures and pressures. It was observed that at 104.04 °C, the diffusivity remained relatively constant regardless of pressure. However, at 162.78 °C and 188.31 °C, the diffusivity exhibited a decreasing trend with increasing pressure.

Naito et al. [Naito et al., 1996] analyzed the pressure effect on gas permeation through semicrystalline polyethylene and polypropylene films. The study covered a pressure range of 1 to 130 atm at 25 °C, which is above the glass transition temperature (T_g). The results showed that the permeability decreased with increasing pressure for gases with low solubility (He, Ne, H_2, N_2, O_2, and Ar). However, for gases with higher solubility, such as CO_2, which have a plasticizing effect, the solubility increased with pressure, i.e., the concentration. To capture these opposing effects, Naito et al. [Naito et al., 1996] proposed a diffusion model given by the equation:

$$D = D_0 \exp\left(-\beta_h p + \alpha_C C\right) \tag{2.31}$$

Here, D_0 represents the diffusion coefficient at $p = 0$ and $C = 0$, β_h is a constant indicating the decrease in diffusivity caused by hydrostatic pressure, and α_C is a constant characterizing the increase in diffusivity due to the plasticizing effect of dissolved penetrant in the polymer.

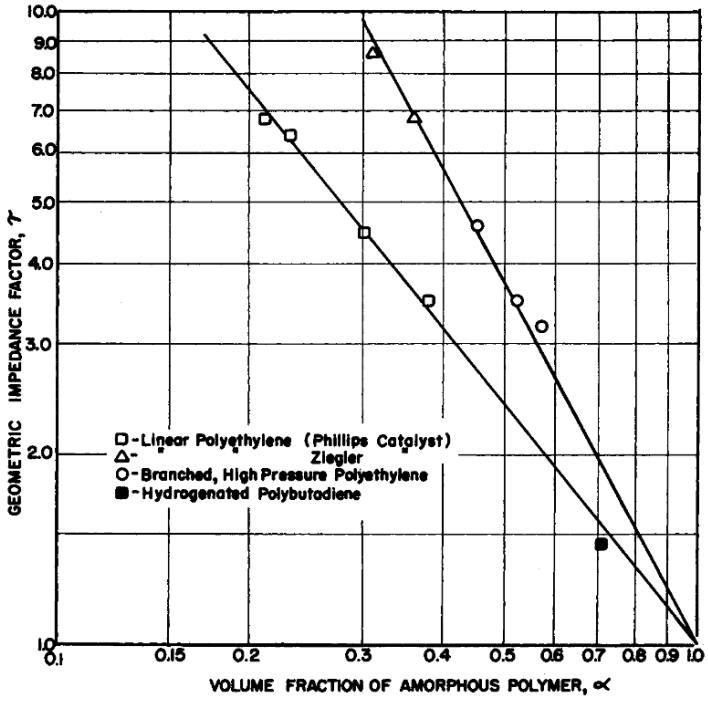

Figure 2.17: *Measures of tortuosity factor provided by Michaels [Michaels and Bixler, 1961b]*

Chapter 3

Methods

3.1 Molecular simulation methods

3.1.1 Representing the molecular system in different thermodynamic ensembles

3.1.1.1 Forcefields

Atomic force fields are essential components of molecular dynamics (MD) and Monte Carlo (MC) simulations, providing a mathematical description of the interactions between atoms in a molecular system. These force fields consist of different types of potentials that capture various aspects of atomic interactions. The potentials are separated into interactions related to bonded atoms and interactions between non-bonded atoms. The following examples of potentials are not exhaustive and only use analytical functions, tabulated potentials are used too. Different forcefields may include more or less potentials.

1. **Bonded interactions**:
    - **Bond potentials**: Bond potentials model the stretching of chemical bonds between atoms. They are typically represented by harmonic potentials, such as the harmonic potential $V_b = \frac{1}{2}k_b(r - r_0)^2$ which describe the energy as a function of bond length r.
    - **Angle potentials**: Angle potentials account for the bending of atoms around a central atom. They are described by mathematical functions that define the energy as a function of the bond angles formed by three atoms θ. Commonly used angle potentials include harmonic potentials $V_\theta = \frac{1}{2}k_\theta(\theta - \theta_0)^2$ or cosine-based potentials.

- **Torsion potentials**: Torsion potentials represent the rotation around dihedral angles ϕ formed by four consecutive atoms. They describe the energy landscape associated with the torsional motion of the atoms. Torsion potentials can be represented by simple trigonometric functions, such as the cosine potential $V_\phi = k_\phi \left(1 + \cos(n_\phi \phi - \phi_0)\right)$, or more complex multi-term potentials.

2. **Non-bonded Interactions**:

   - **Van der Waals Potentials**: Van der Waals potentials encompass the attractive forces between atoms arising from instantaneous induced dipole moments, as well as the repulsion resulting from the Pauli exclusion principle. They are typically described by Lennard-Jones potentials $V_{\text{vdW}} = 4\varepsilon \left[\left(\frac{\sigma}{r}\right)^{12} - \left(\frac{\sigma}{r}\right)^{6} \right]$ or other more sophisticated functions that incorporate higher order terms.
   - **Electrostatic Potentials**: Electrostatic potentials capture the long-range Coulombic interactions between charged atoms. In classical MD and MC simulations, these interactions are often represented by Coulombic interaction between partial charges $V_{\text{elec}} = \frac{1}{4\pi\epsilon_0} \frac{q_i q_j}{r_{ij}}$. Additionally, point charge models or more advanced schemes, such as polarizable force fields or Drude oscillators, can be employed depending on the required description level.

Parameters: These different potentials collectively define the force field used in MD and MC simulations. Force field parameters, such as equilibrium bond lengths r_0, force constants k_b, bond angles θ_0, force constants k_θ, torsion angles ϕ_0, force constants k_ϕ, and van der Waals parameters ε and σ, are typically derived from experimental data or quantum mechanical calculations.
In the context of molecular simulations, the total potential energy of a system in a specific configuration is obtained by summing the contributions from all the individual potentials. There are two main approaches for altering the system's configuration: the Monte Carlo sampling method and molecular dynamics, both of which are described in detail below.

3.1.1.2 Periodic boundary conditions (PBC)

Periodic boundary conditions (PBC) are commonly employed in molecular simulations to simulate systems with a finite number of particles in an effectively infinite environment. This approach allows to study bulk properties of materials by simulating a representative unit cell and assuming the system repeats periodically in all directions.

The main idea behind PBC is to create an artificial box around the simulation system. Any particle leaving the box on one side immediately re-enters the box from the opposite side, as if the system wraps around like a torus.

To illustrate this concept, let's consider a three-dimensional simulation box. A particle at position (x, y, z) with coordinates outside the box is transformed as follows:

$$
\begin{aligned}
x' &= x - n_x \cdot L_x \\
y' &= y - n_y \cdot L_y \\
z' &= z - n_z \cdot L_z
\end{aligned}
$$

where L_x, L_y, and L_z are the dimensions of the simulation box, and n_x, n_y, and n_z are integers representing the number of periodic images in each direction. These integers determine how many times the particle has crossed the boundaries of the box.

As a result of these transformations, the particle is placed back into the box, and its position is shifted by multiples of the box dimensions. This ensures that interactions and calculations involving the particle are correctly accounted for within the simulation.

3.1.1.3 Cutoff and Ewald summation

In simulations involving coulombic and Lennard-Jones interactions, a cutoff radius is typically chosen, usually around 1 nm. Beyond this cutoff, the long-range coulombic potential energy is computed using a technique called Ewald summation [Kolafa and Perram, 1992]. In Ewald summation, the long-range interaction between the charges of a central unit cell and all the charges of the lattice is performed in the reciprocal space of the periodic lattice. To improve computational efficiency, the summation may be performed over a mesh of charge densities using the Particle-Particle Particle-Mesh (PPPM) method [Plimpton et al., 1997]. For the Lennard-Jones interaction, beyond the cutoff, the potential is modified to converge to zero in a finite distance and a correction is added to take into account the interaction between the cutoff and the infinite.

3.1.1.4 Computation of thermodynamic quantities, sampling from ensembles

Molecular simulations allow for the sampling of microstates in a system consisting of N particles. Statistical physics provides a framework for connecting the microscopic view to macroscopic quantities. In molecular simulations, we obtain the microscopic configurations of the system. The thermodynamic state of a system is defined by a finite set of parameters, such as the number of particles N, temperature T, and pressure P. Other thermodynamic quantities are typically derived from these parameters using thermodynamic identities.

The positions and momenta of the particles are represented as coordinates in a multidimensional space known as the phase space. For a system with N particles, the phase space has $6N$ dimensions. $\mathcal{A}(t)$ denotes the instantaneous value of a specific property, while $\mathcal{A}(\Gamma)$ represents the value of that property at point Γ. The macroscopic quantity, denoted as $\mathcal{A}_{\text{obs}}$, is given by:

$$\mathcal{A}_{\text{obs}} = \langle \mathcal{A}(\Gamma(t)) \rangle_{\text{time}} = \lim_{t_{\text{obs}} \to +\infty} \frac{1}{t_{\text{obs}}} \int_0^{t_{\text{obs}}} \mathcal{A}(\Gamma(t))\, dt \tag{3.1}$$

Since numerical simulation is inherently discrete, we express the above equation as:

$$\mathcal{A}_{\text{obs}} = \langle \mathcal{A}(\Gamma(t)) \rangle_{\text{time}} = \frac{1}{\tau_{\text{obs}}} \sum_{\tau=1}^{\tau_{\text{obs}}} \mathcal{A}(\Gamma(\tau)) \tag{3.2}$$

This discrete approach is employed when integrating the particle motion over time using Newton's equations, as in molecular dynamics simulations with a time step τ. To ensure equation (3.2) holds, the simulation must adequately sample the entire phase space, and

thermodynamic consistency must be achieved between simulations with different initial configurations but the same macroscopic parameters.

When equilibrium is reached, Gibbs showed that instead of averaging over time, we can average over the statistical ensemble. This leads to:

$$\mathcal{A}_{\text{obs}} = \langle \mathcal{A} \rangle_{\text{ens}} = \langle \mathcal{A} | \rho_{\text{ens}} \rangle = \sum_{\Gamma} \mathcal{A}(\Gamma) \rho_{\text{ens}}(\Gamma) \tag{3.3}$$

Here, $\rho_{\text{ens}}(\Gamma)$ represents the probability of a given microstate Γ. In equilibrium, ρ_{ens} becomes independent of time. A trajectory that visits all the microconfigurations where ρ_{ens} is nonzero is called ergodic. It is important so that the system does not stay trapped in a subspace of the phase space. For each statistical ensemble, it is possible to write the ρ_{ens}, for example:

Canonical ensemble (NVT):

$$\rho_{NVT} = \frac{\exp\left(-\frac{\mathcal{H}(\Gamma)}{k_B T}\right)}{\sum_{\Gamma} \exp\left(-\frac{\mathcal{H}(\Gamma)}{k_B T}\right)} \tag{3.4}$$

where k_B is the Boltzmann constant and $\mathcal{H}$ represents the Hamiltonian.

Isothermal-Isobaric ensemble (NPT):

$$\rho_{NPT} = \frac{\exp\left(-\frac{\mathcal{H}(\Gamma)+PV(\Gamma)}{k_B T}\right)}{\sum_{\Gamma} \exp\left(-\frac{\mathcal{H}(\Gamma)+PV(\Gamma)}{k_B T}\right)} \tag{3.5}$$

Grand canonical (μVT):

$$\rho_{\mu VT} = \frac{\exp\left(-\frac{\mathcal{H}(\Gamma)-\mu N(\Gamma)}{k_B T}\right)}{\sum_{\Gamma} \exp\left(-\frac{\mathcal{H}(\Gamma)-\mu N(\Gamma)}{k_B T}\right)} \tag{3.6}$$

where μ represents the chemical potential of the particle bath that is in contact with the system, N is the number of particle.

It is not feasible to compute ρ_{ens} for each microstate. Another strategy is to use equation (3.2). However, instead of following Newton's laws of motion to visit microstates in a given ensemble, it is possible, in principle, to design an ergodic trajectory (with physical or non-physical moves) to sample microconfigurations representative of a system in an ensemble. This is the approach followed in Monte Carlo simulations, which will be discussed in more detail later.

3.1.2 Molecular dynamics

Molecular dynamics simulation is a computational technique used to study the behavior and dynamics of molecules at the atomic level. It is a powerful tool for investigating the physical and chemical properties of molecular systems and their interactions.

In a MD simulation, a set of equations of motion, typically derived from Newton's laws, is numerically solved to track the positions and velocities of individual atoms over time. By

simulating the motion and interactions of atoms, MD provides insights into the thermodynamics, kinetics, and structural properties of molecules and materials.

The simulation begins with an initial configuration of atoms, which can be generated from experimental data or constructed based on theoretical models. Each atom is assigned an initial position and velocity. Then, using the equations of motion and interatomic potentials (such as force fields), the positions and velocities of the atoms are updated at discrete time steps, typically in femtosecond intervals.

During the simulation, the atoms move and interact with each other, driven by the forces derived from the interatomic potentials. The simulation proceeds by integrating the equations of motion over thousands or millions of time steps, representing the system's evolution over a desired time scale. Statistical analysis techniques can be applied to extract meaningful information from the trajectory, such as thermodynamic properties, structural characteristics, and dynamic processes.

3.1.2.1 Integration

The goal is to solve the laws of motion for all the atom positions $\mathbf{r_i}(t) = (x_i(t), y_i(t), z_i(t))$ considering the force vector $\mathbf{F_i}$ acting on each particle with mass m_i:

$$\frac{\mathbf{F_i}}{m_i} = \frac{d^2\mathbf{r_i}(t)}{dt^2} \tag{3.7}$$

There are several methods available to numerically solve the given equations. One commonly used approach, implemented in the LAMMPS code [Thompson et al., 2022], is the Velocity-Verlet algorithm.

The Newton equation can be separated into two equations:

$$\begin{aligned} \frac{d\mathbf{r_i}(t)}{dt} &= \mathbf{v_i} \\ \frac{d\mathbf{v_i}(t)}{dt} &= \frac{\mathbf{F_i}}{m_i} \end{aligned} \tag{3.8}$$

with $\mathbf{v_i}$ the velocity of the particle. We can express the positions and velocities at a later time using a Taylor series expansion:

$$\begin{aligned} \mathbf{r_i}(t+\Delta t) &= \mathbf{r_i}(t) + \mathbf{v_i}(t)\Delta t + \frac{\mathbf{F_i}(t)}{2m_i}(\Delta t)^2 \\ \mathbf{v_i}(t+\Delta t) &= \mathbf{v_i}(t) + \frac{\mathbf{F_i}(t)}{m_i}\Delta t + \frac{1}{2m_i}\frac{d\mathbf{F_i}(t)}{dt}(\Delta t)^2 \end{aligned} \tag{3.9}$$

Approximating the derivative of force as $\frac{d\mathbf{F_i}(t)}{dt} \approx \frac{\mathbf{F_i}(t+\Delta t)-\mathbf{F_i}(t)}{\Delta t}$, we can simplify the equations:

$$\begin{aligned}\mathbf{r_i}(t+\Delta t) &= \mathbf{r_i}(t) + \mathbf{v_i}(t)\Delta t + \frac{\mathbf{F_i}(t)}{2m_i}(\Delta t)^2 \\ \mathbf{v_i}(t+\Delta t) &= \mathbf{v_i}(t) + \frac{\mathbf{F_i}(t) + \mathbf{F_i}(t+\Delta t)}{2m_i}\Delta t\end{aligned} \tag{3.10}$$

Using these equations, we can compute the trajectories of all the atoms step by step. At each step, the forces exerted on each atom are computed, and new positions and velocities are obtained. Since all the forces are pairwise forces and sum to zero, the total energy is conserved during the simulation, the system is evolving in the NVE ensemble.

3.1.2.2 Time step

The selection of an appropriate time step, denoted as Δt, plays a critical role in numerical simulations. It is commonly chosen to be one or two orders of magnitude smaller than the fastest characteristic time of vibration for a bond within the system. For instance, the vibration time period of C-H or O-H bonds is approximately 100 fs. Consequently, the time step Δt is typically set to be on the order of femtosecond.

3.1.2.3 Computation of thermodynamic quantities

The instantaneous temperature is computed from the velocities at each step for a system with N atoms:

$$T(t) = \sum_{i=1}^{N} \frac{m_i \mathbf{v_i}^2(t)}{k_B N_f} \tag{3.11}$$

where N_f is equal to the number of degrees of freedom, $N_f = 3N - 3$. Similarly it is possible to compute the instantaneous pressure:

$$P(t) = \frac{1}{V}\left(\frac{1}{3}\sum_i m_i \mathbf{v_i}^2 + \frac{1}{3}\sum_i \mathbf{r_i} \cdot \mathbf{F_i}\right) \tag{3.12}$$

The instantaneous pressure and temperature are averaged over time when equilibrium is achieved to compute the macroscopic thermodynamic quantities. The formalism we presented allows performing simulation in the NVE ensemble. The number of atoms is constant, the volume too, and the energy is also constant if the numerical integration is performed with a Δt small enough. In the real world, we are more interested in systems at equilibrium with constant pressure or temperature such as the atmosphere or the ocean. In the next sections, methods used to simulate our system in equilibrium with a thermostat and/or a barostat, or in other words, in the canonical ensemble (NVT) and in the isothermal-isobaric ensemble (NPT), are presented.

3.1.2.4 Nosé-Hoover thermostat

A method used to implement the NVT ensemble is the renormalization of the speeds of all particles at each step so that equation (3.11) is equal to the thermostat temperature [Berendsen et al., 1984]. Another possibility is to modify the equations of motion to include

a non-Newtonian term to maintain the total kinetic energy constant, it can be thought as a friction coefficient or a coupling with a heat bath constituted of a fictious one dimensional particule, it was proposed by Nosé and Hoover [Nosé, 1984, Hoover, 1985], it is usually described in the Hamiltonian formalism with the conjugate coordinates $(\mathbf{r_i}, \mathbf{p_i})$ where $\mathbf{p_i} = m\mathbf{v_i}$ coupled with the one dimensional fictious particle with conjugate coordinates (s, p_s):

$$\begin{aligned}
\frac{d\mathbf{r_i}(dt)}{dt} &= \frac{\mathbf{p_i}(t)}{m_i s^2} \\
\frac{d\mathbf{p_i}}{dt} &= -\frac{\partial U(\mathbf{r_1}, \cdots, \mathbf{r_N})}{\partial \mathbf{r_i}} \\
\frac{ds}{dt} &= \frac{p_s}{Q} \\
\frac{dp_s}{dt} &= \frac{1}{s}\left[\sum_i^N \frac{\mathbf{p_i}^2}{m_i s^2} - g k_B T\right]
\end{aligned} \tag{3.13}$$

with $g = 3N + 1$, Q the mass of the fictious particle and $U(\mathbf{r_1}, \cdots, \mathbf{r_N})$ is the potential energies of the non-fictious particules.
It was shown that ergodicity was not guaranteed with this thermostat, meaning that the system would not correctly sample the phase space. It was modified by Martyna et al. [Martyna et al., 1992] to solve this problem. The new version is called the Nosé-Hoover chain thermostat. M thermostats which are one dimensional fictious particles of mass Q_k are coupled to one another like a chain.

$$\begin{aligned}
\frac{d\mathbf{r_i}(t)}{dt} &= \frac{\mathbf{p_i}(t)}{m_i} \\
\frac{\mathbf{p_i}}{m_i} &= -\frac{\partial U(\mathbf{r_1}, \cdots, \mathbf{r_N})}{\partial \mathbf{r_i}} - \frac{p_{\zeta_1}}{Q_1}\mathbf{p_i} \\
\frac{d\zeta_k}{dt} &= \frac{p_{\zeta_k}}{Q_k}, \quad k = 1, \cdots, M \\
\frac{dp_{\zeta_1}}{dt} &= \left[\sum_i^N \frac{\mathbf{p_i}^2}{m_i} - g k_B T\right] - \frac{p_{\zeta_2}}{Q_2} p_{\zeta_1} \\
&\vdots \\
\frac{dp_{\zeta_k}}{dt} &= \left[\frac{p_{\zeta_{k-1}}^2}{Q_{k-1}} - k_B T\right] - \frac{p_{\zeta_{k+1}}}{Q_{k+1}} p_{\zeta_k} \\
&\vdots \\
\frac{dp_{\zeta_M}}{dt} &= \left[\frac{p_{\zeta_{M-1}}^2}{Q_{M-1}} - k_B T\right]
\end{aligned} \tag{3.14}$$

The total canonical Hamiltonian which is conserved and satisfies the ergodicity condition is:

$$\mathcal{H}_{NHC}(\mathbf{r}, \mathbf{p}, \zeta, \mathbf{p}_\zeta) = \sum_{i=1}^N \frac{\mathbf{p_i}^2}{2m_i} + \sum_{i=1}^M \frac{p_{\zeta_i}^2}{2Q_i} + N k_B T \zeta_1 + \sum_{i=2}^M k_B T \zeta_i + U(\mathbf{r}) \tag{3.15}$$

The considered systems in this work are relaxed in the NPT ensemble. For the relaxations needed for the high deformation, the NVT ensemble is used.

3.1.2.5 Isothermal-isobaric ensemble (NPT)

Shinoda [Shinoda et al., 2004] proposed a way to have simultaneously a thermostat and a barostat combining Parinello-Rahman work [Parrinello and Rahman, 1981] and Martyna chained thermostat [Martyna et al., 1992]. This isothermal-isobaric ensemble is often called Nosé-Hoover too. The M degrees of freedom from the chain thermostat have to be taken into account.

$$\begin{aligned}
\tau &= \mathbf{h}_0^{-1}(\sigma - P\mathbf{I})(\mathbf{h}_0^T)^{-1} \\
\pi_{\alpha\beta} &= c\sum_{\mu\nu} G_{\alpha\mu}G_{\mu\nu}\frac{dh_{\nu\beta}}{dt} \\
\frac{d\pi}{dt} &= V(\mathbf{P_{int}} - P\mathbf{I}) - \mathbf{h}\tau\mathbf{h}^T + \left(\frac{1}{3N}\sum_{i=1}^{N}\frac{\mathbf{p_i}^2}{m_i}\right) - \frac{p_{\zeta_1}}{Q_1}\pi \\
\frac{d\mathbf{h}}{dt} &= \frac{1}{W}\pi\mathbf{h} \\
\frac{dp_{\zeta_1}}{dt} &= \sum_{i=1}^{N}\frac{\mathbf{p_i}^2}{m_i} + \frac{1}{W}\mathbf{Tr}(\pi^T\pi) - (3N+d^2)k_BT - \frac{p_{\zeta_1}p_{\zeta_2}}{Q_2} \\
\frac{d\mathbf{p_i}}{dt} &= \frac{\partial U(\mathbf{r})}{\partial \mathbf{r_i}} - \frac{1}{W}\left(\pi\mathbf{p_i} - \frac{1}{3N}\mathbf{Tr}(\pi)\mathbf{p_i}\right) - \frac{p_{\zeta_1}}{Q_1}\mathbf{p_i} \\
\frac{d\mathbf{r_i}}{dt} &= \frac{\mathbf{p_i}}{m_i} + \frac{1}{W}\pi\mathbf{r_i}
\end{aligned} \tag{3.16}$$

The c constant is a coupling constant [Ray, 1983]. Only the equation of the first link of the chain is written for the thermostat. W is the mass associated to the barostat, and the Q_j are the masses associated to each link of the thermostat chain. $(3N + d^2)$ is the number of degrees of freedom of the system with d the dimensionality of the simulation domain. Martyna *et al.* proposed some way to choose the masses W and Q_i [Martyna et al., 1996].

$$\begin{aligned}
Q_1 &= \frac{3Nk_BT}{\omega_T^2} \\
Q_i &= \frac{k_BT}{\omega_T^2} \\
W &= \frac{(3N+3)k_BT}{3\omega_P^2}
\end{aligned} \tag{3.17}$$

where ω_T is the period associated to the thermostats, and ω_P the period of the barostat. In the simulation codes like LAMMPS, it is usually asked to define those values with the characteristic times.

$$\begin{aligned}
\tau_T &= \omega_T^{-1} \\
\tau_P &= \omega_P^{-1}
\end{aligned} \tag{3.18}$$

3.1.3 Monte Carlo

3.1.3.1 The detailed balance condition, a way to sample stationary distributions

The Monte Carlo method involves exploring the phase space in a random manner, taking into consideration the probability of each microstate occurring. However, generating a set

of configurations that respects their probability of existence presents a challenge. Let us denote this set of configurations as $\{\Gamma\}$. In 1953, Metropolis, Rosenbluth and Rosenbluth, and Teller [Metropolis et al., 1953] introduced an algorithm that generates this set of configurations by following a Markovian stochastic process. The probability of generating a new configuration Γ' does not depend on all the previously explored configurations but only on the current configuration Γ. The configuration Γ' is randomly generated and then accepted with a certain probability. If we denote $P(\Gamma, n_{\text{step}})$ as the probability of being in configuration Γ at step n_{step}, and $W(\Gamma \to \Gamma')$ as the probability of transitioning from configuration Γ to Γ', we can express this relationship as follows:

$$P(\Gamma, n_{\text{step}}+1) = P(\Gamma, n_{\text{step}}) - \sum_{\Gamma' \neq \Gamma} P(\Gamma, n_{\text{step}}) W(\Gamma \to \Gamma') + \sum_{\Gamma' \neq \Gamma} P(\Gamma', n_{\text{step}}) W(\Gamma' \to \Gamma) \tag{3.19}$$

The equation states that the probability of being in microstate Γ at step $n_{\text{step}}+1$ is equal to the probability of being in microstate Γ at step n_{step}, minus the sum of probabilities of transitioning out of microstate Γ, and then adding the probability of transitioning to microstate Γ from any other state Γ'. This equation captures the balance between the probabilities of staying in or leaving microstate Γ during the transition from step n_{step} to $n_{\text{step}}+1$.

In the steady state, the probability of being in state Γ does not depend on the step ($P(\Gamma, n_{\text{step}}+1) = P(\Gamma, n_{\text{step}})$). Equation 3.19 becomes:

$$\sum_{\Gamma' \neq \Gamma} P(\Gamma, n_{\text{step}}) W(\Gamma \to \Gamma') = \sum_{\Gamma' \neq \Gamma} P(\Gamma', n_{\text{step}}) W(\Gamma' \to \Gamma) \tag{3.20}$$

A way to ensure that equation 3.20 holds is called detailed balance, we impose:

$$P(\Gamma, n_{\text{step}}) W(\Gamma \to \Gamma') = P(\Gamma', n_{\text{step}}) W(\Gamma' \to \Gamma) \tag{3.21}$$

This condition on the probability of transitions satisfies that the distributions of configurations is stationary.

3.1.3.2 The metropolis algorithm for an ergodic sampling

The detailed balance condition allows us to obtain stationary distributions when transitioning from one microstate to another. However, in addition to detailed balance, another important aspect is ergodicity, which ensures that microstates are sampled in accordance with the chosen thermodynamic statistical ensemble. This is the aim of the Metropolis algorithm:

- Start with an initial configuration, denoted as Γ.
- Choose a configuration, Γ' using a probability $P_{gen}(\Gamma \to \Gamma')$.
- This configuration is accepted with a probability $P_{acc}(\Gamma \to \Gamma')$. This probability depends of the statistical ensemble you chose (this is detailed later).
  The probability of transitionning $W(\Gamma \to \Gamma')$ is :

  $$W(\Gamma \to \Gamma') = P_{gen}(\Gamma \to \Gamma') P_{acc}(\Gamma \to \Gamma') \tag{3.22}$$

  The detailed balance conditions is written:

  $$P(\Gamma) P_{gen}(\Gamma \to \Gamma') P_{acc}(\Gamma \to \Gamma') = P(\Gamma') P_{gen}(\Gamma' \to \Gamma) P_{acc}(\Gamma' \to \Gamma) \tag{3.23}$$

To satisfy the equation, Metropolis et al. proposed:

$$P_{acc}(\Gamma \to \Gamma') = min\left[1, \frac{P(\Gamma')P_{gen}(\Gamma' \to \Gamma}{P(\Gamma)P_{gen}(\Gamma \to \Gamma')}\right] \tag{3.24}$$

In standard Monte Carlo simulation, Γ' is generated randomly, so:

$$P_{gen}(\Gamma \to \Gamma') = P_{gen}(\Gamma' \to \Gamma) \tag{3.25}$$

Then :

$$P_{acc}(\Gamma \to \Gamma') = min\left[1, \frac{P(\Gamma')}{P(\Gamma)}\right] \tag{3.26}$$

In the case of the canonical ensemble:

$$\frac{P(\Gamma')}{P(\Gamma)} = \exp\left(-\frac{\mathcal{H}(\Gamma') - \mathcal{H}(\Gamma)}{k_B T}\right) \tag{3.27}$$

where $\mathcal{H}(\Gamma)$ and $\mathcal{H}(\Gamma')$ are the potential energies of configurations Γ and Γ', respectively, k_B is the Boltzmann constant, and T is the temperature. Compare this ratio to a random number between 0 and 1. If $\frac{P(\Gamma')}{P(\Gamma)} \geq 1$, accept the proposed configuration Γ' as the new current configuration. If $\frac{P(\Gamma')}{P(\Gamma)} < 1$, generate a random number, r, between 0 and 1. Accept Γ' if $r < \frac{P(\Gamma')}{P(\Gamma)}$, otherwise, keep the current configuration Γ. Repeat the generation of new configurations until the relevant macroscopic quantities are converging.

To sample other ensembles the equation 3.27 is replaced using the corresponding probabilities from other ensembles (refer to section 3.1.1.4).

3.1.3.3 Example of Monte Carlo moves

In this section, we will present examples of different Monte Carlo moves changing the configuration Γ toward a configuration Γ'

- Translation: The move consists into choosing a molecule randomly and translate it with a vector with its three components randomly generated between $[-D_{max}, D_{max}]$
- Rotation: For non mono-atomic molecule, three angles related to the three internal rotational degrees of liberty are randomly picked in $[-\theta_{max}, \theta_{max}]$ to rotate the molecule.
- Insertion, deletion of a molecule randomly picked. This moves is used to sample the grand canonical ensemble. The acceptance is given by the probability of the new configuration in the grand canonical ensemble.
- Exchange: Two molecules are randomly picked and exchange.

3.1.3.4 Biased Monte Carlo simulation

The previously described simulation steps involve generating new configurations in a completely random manner, making them unbiased. However, in certain cases, especially when studying large molecules, the acceptance probability of these steps can be significantly low. For example, during the insertion step, unbiased insertion of molecules into micro-cavities

has a minimal chance of being accepted if the insertion position is chosen randomly. The probability of selecting a position that lies within the polymer matrix is much higher. In general, randomly choosing a favorable position within a dense system that would be accepted is highly unlikely. As a result, achieving thermodynamic equilibrium within the available simulation times becomes unattainable.

To overcome this limitation, it becomes necessary to introduce bias into the simulation process. Instead of generating new configurations entirely at random, configurations are selected from a set of potential configurations based on an energy criterion. This leads to a distinction between the terms $P_{\text{gen}}(\Gamma \to \Gamma')$ and $P_{\text{gen}}(\Gamma' \to \Gamma)$, requiring their explicit calculation to determine the acceptance probability of the proposed move. One way to illustrate this is through the use of a pre-insertion bias:

In the pre-insertion bias approach, rather than attempting to insert a full molecule into the structure, trials are performed using a Lennard-Jones bead located at the same center of mass. The Lennard-Jones bead is used to find a suitable position but it is not actually inserted. The process involves the following steps:

1. k positions are drawn randomly within the simulation box.

2. For each of the k positions, the configuration energy is computed to calculate the Rosenbluth factor:

$$W(\Gamma_N \to \{\Gamma_{N+1}\}) = \sum_{i=1}^{k} \exp\left(-\frac{\mathcal{H}^{LJ}(\Gamma^i_{N+1})}{k_B T}\right) \tag{3.28}$$

   Here, Γ_N represents a configuration with N molecules, Γ_{N+1} is a configuration with $N+1$ molecules, and $\mathcal{H}^{\mathcal{LJ}}(\Gamma^i_{N+1})$ is the energy of the Lennard-Jones bead at position i with $i \in \{1, ..., k\}$.

3. Each configuration i out of the k configurations has a probability to be chosen:

$$P(\Gamma_N \to \Gamma^i_{N+1}) = \frac{\exp\left(-\frac{\mathcal{H}(\Gamma^i_{N+1})}{k_B T}\right)}{W(\Gamma_N \to \{\Gamma_{N+1}\})} \tag{3.29}$$

4. The probability of generating Γ_N from Γ_{N+1}, which involves removing a molecule from the box and placing it in a fictitious and infinite molecule tank (representing an ideal gas), is given by:

$$P_{\text{gen}}(\Gamma_{N+1} \to \Gamma_N) = \frac{1}{k} \tag{3.30}$$

The acceptance probability of the movement is then calculated as follows:

$$P_{\text{acc}}(\Gamma_N \to \Gamma_{N+1}) = \min\left[1, \exp\left(-\frac{\mathcal{H}(\Gamma_{N+1}) - \mathcal{H}(\Gamma_N) - \mu}{k_B T}\right) \frac{W(\Gamma_N \to \{\Gamma_{N+1}\})}{k \exp\left(-\frac{\mathcal{H}^{LJ}(\Gamma^i_{N+1})}{k_B T}\right)}\right] \tag{3.31}$$

It should be noted that the Hamiltonian $\mathcal{H}$ without superscript is the Hamiltonian of the true inserted molecule not the Hamiltonian of the Lennard-Jones bead.
Rotation-biased moves are usually added to the pre-insertion bias, in a similar fashion, with k possible rotations picked instead of k positions.

3.2 Building semicrystalline model

3.2.1 Adhikari's theory: a statistic of tie chain, loops, and tails

In this section, we briefly recall the Adhikari and Muthukumar theory [Adhikari and Muthukumar, 2019] used to generate the amorphous phase of the semicrystalline structure. For a detailed presentation of this work, please refer to the original paper.

The Adhikari and Muthukumar theory allows for the study of the statistics of ties and loops for a reference chain of finite length, considering its connectivity to multiple lamellae. The theory assumes that polymer chains in amorphous regions follow Gaussian statistics. Ties, loops, and tails are obtained from a three-dimensional random walk between "absorbing" walls.

The random walk of the reference polymer chain starts at a point in an amorphous region and continues until it touches a lamellar surface, forming the first chain end, known as a tail. Once the chain touches a lamellar surface, the formation of a rigid and vertical crystalline stem is guaranteed. The chain then emerges out of the crystalline lamella and enters the other amorphous region. The random walk continues, giving rise to loops or ties until the reference chain ends in the amorphous region.

In this statistic, the probability of formation of one of the chain path (see figure 3.1) in a semi-crystalline of infinite layers of crystalline lamellae and amorphous regions that is forming 4 stems, 2 tie chains ($n_{tie} = 2$), one loop ($n_{loop} = 1$) and 2 tails ($n_{tails} = 2$) is:

$$Z(N) = \int_0^{N-4m'} ds_1 \int_{s_1+m'}^{N-3m'} ds_2 \int_{s_2+m'}^{N-2m'} ds_3 \int_{s_3+m'}^{N-m'} ds_4 \times g_{tail}(s_1) g_{tie}(s_2 - s_1 - m') g_{loop}(s_3 - s_2 - m') \times g_{tie}(s_4 - s_3 - m') g_{tail}(N - s_4 - m') \quad (3.32)$$

where m' is the interlamella width in Kuhn length used as a unit of length and the $g_{tail}(s)$, $g_{loop}(s)$ and $g_{tie}(s)$ are the probability of formation of a tail, a loop, and a tie chain, at s Kuhn segments after emerging from the crystallite. Those g_i ($i = tail, loop, tie$) are found by modeling the random walk between two absorbing walls. In this formalism, when a freely jointed chain hits a crystallite wall, it automatically forms a tie chain or a loop. It is more convenient to write $Z(N)$ as $Z(N_a)$ with $N_a = N - 4m'$ the number of beads or the length of the polymer in Kuhn length in the amorphous region. It has been shown by Muthukumar in ref. [Muthukumar, 1996, Muthukumar, 2003] that the transformation of $Z(N_a)$ in Laplace space can be written as:

$$\tilde{Z}(E) = (\tilde{g}_{tail}(E))^2 (\tilde{g}_{tie}(E))^2 (\tilde{g}_{loop}(E)) \quad (3.33)$$

where the $\tilde{g}_i(E)$ are the Laplace transformations of the $g_i(s)$. It is generalized for a walk of n_{tie} tie chains, n_{loop} loops and 2 tails (a single linear, not branched, polymer has only two tails) as:

$$\tilde{Z}(E) = (\tilde{g}_{tail}(E))^2 (\tilde{g}_{tie}(E))^{n_{tie}} (\tilde{g}_{loop}(E))^{n_{loop}} \quad (3.34)$$

It is obvious that $n_{stem} = n_{tie} + n_{loop} + 1$, that the total number of chain sections in the amorphous is $n_{tie} + n_{loop} + 2 = n_{stem} + 1$ and that $N_a = N - n_{stem} m'$. Hence, $n_{loop} = n_{stem} - n_{tie} - 1$. Noticing that $Z(N_a)$ is also a function, by allowing the length of tails, loops, and ties to vary, Adhikari and Muthukumar calculate the probability of forming a chain of

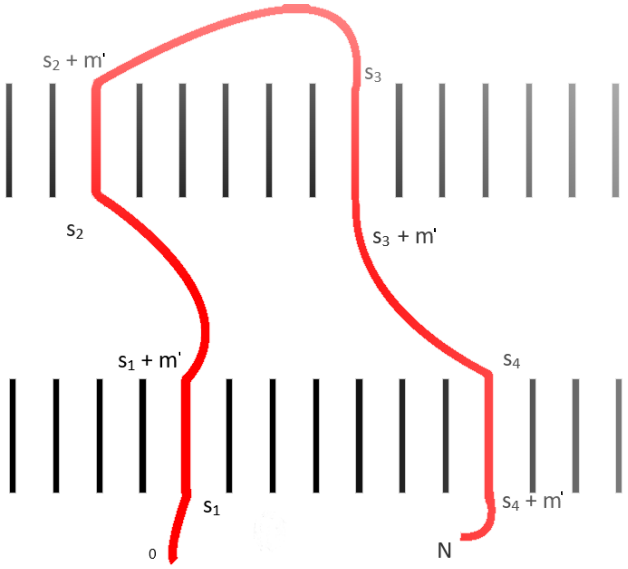

Figure 3.1: *A polymer of length N, forming 4 stems when crossing the crystalline lamella (the hatched area), 2 tie chains between $(s_1+m') \rightarrow s_2$ and $(s_3+m') \rightarrow s_4$, a loop between (s_2+m') and s_3, and two tails at 0 and at N. The figure is an adaptation of Adhikari's one [Adhikari and Muthukumar, 2019].*

length N with a number of ties n_{tie} when n_{stem} stems exist, associated with an arbitrary number of lamellae and amorphous regions. This probability is given as:

$$Z(n_{\text{tie}}, n_{\text{stem}}, N) = \mathcal{L}^{-1}\left[(\tilde{g}_{\text{tail}}(E))^2(\tilde{g}_{\text{tie}}(E))^{n_{\text{tie}}}(\tilde{g}_{\text{loop}}(E))^{n_{\text{stem}}-n_{\text{tie}}-1}\right], \tag{3.35}$$

where $\mathcal{L}^{-1}$ is the inverse Laplace operator, and $\tilde{g}_{\text{tie}}(E)$, $\tilde{g}_{\text{tail}}(E)$, and $\tilde{g}_{\text{loop}}(E)$ are the Laplace transforms of $g_{\text{tie}}(s)$, $g_{\text{tail}}(s)$, and $g_{\text{loop}}(s)$, respectively.

The final expression for the probability, including a typo correction from the Adhikari and Muthukumar paper, is:

$$\begin{aligned} Z(n_{\text{tie}}, n_{\text{stem}}, N) = \mathcal{L}^{-1}\Bigg[&\left(\frac{1}{E} - \frac{\sinh\left(\sqrt{\frac{E}{D}}\right)}{E\sinh\left(d'\sqrt{\frac{E}{D}}\right)} - \frac{\sinh\left((d'-1)\sqrt{\frac{E}{D}}\right)}{E\sinh\left(d'\sqrt{\frac{E}{D}}\right)}\right)^2 \\ &\times \left(\frac{\sinh\left(\sqrt{\frac{E}{D}}\right)}{\sinh\left(d'\sqrt{\frac{E}{D}}\right)}\right)^{n_{\text{tie}}} \left(\frac{\sinh\left((d'-1)\sqrt{\frac{E}{D}}\right)}{\sinh\left(d'\sqrt{\frac{E}{D}}\right)}\right)^{n_{\text{stem}}-n_{\text{tie}}-1}\Bigg]. \end{aligned} \tag{3.36}$$

Here, $D = 1/6$ in our study, and d' is the intercrystalline length expressed in Kuhn length units.

The fraction of tie segments is obtained from the probability $Z(n_{\text{tie}}, n_{\text{stem}}, N)$. When the number of formed stems is n_{stem}, the number of ties can vary from zero to $n_{\text{stem}} - 1$. Additionally, for a fixed number of stems, there are different ways of forming a given number of ties. The average number of ties formed per molecule, $\bar{n}_{\text{tie}}$, is then given by:

$$\bar{n}_{\text{tie}} = \frac{\sum_{n_{\text{tie}}=0}^{n_{\text{stem}}-1} \omega_{n_{\text{tie}}} n_{\text{tie}} Z(n_{\text{tie}}, n_{\text{stem}}, N)}{\sum_{n_{\text{tie}}=0}^{n_{\text{stem}}-1} \omega_{n_{\text{tie}}} Z(n_{\text{tie}}, n_{\text{stem}}, N)}, \tag{3.37}$$

where $\omega_{n_{\text{tie}}}$ is the number of ways of forming n_{tie} ties when the total number of ties and loops per molecule is $n_{\text{stem}} - 1$, given by:

$$\omega_{n_{\text{tie}}} = \frac{(n_{\text{stem}} - 1)!}{n_{\text{tie}}!(n_{\text{stem}} - 1 - n_{\text{tie}})!}. \tag{3.38}$$

Finally, the fraction of ties f_{tie} is given by:

$$f_{\text{tie}} = \frac{\bar{n}_{\text{tie}}}{n_{\text{stem}} + 1}. \tag{3.39}$$

Knowing the average number of tie chains per molecule, we obtain the average number of loop chains per molecule as $\bar{n}_{\text{loop}} = n_{\text{stem}} - 1 - \bar{n}_{\text{tie}}$. The number of tail segments per molecule is $n_{\text{tail}} = 2$.

3.2.2 Adapting Adhikari's theory to build semicrystalline samples

In this section, we present the application of Adhikari and Muthukumar theory to construct semi-crystalline samples for molecular dynamics simumlation studies. The computation of the fraction of ties using this theory requires a small amount of input data, including the reference chain length N, the amorphous thickness d, and the crystalline lamellar thickness m. The last two quantities can be obtained using the degree of crystallinity χ_c. In their work [Adhikari and Muthukumar, 2019], equal densities of the crystalline and amorphous phases were assumed. The length distribution of ties and loops in Kuhn segment length, as well as the tie fractions, are obtained from the theory.

In our work, our aim is to build semicrystalline samples at the atomistic length scale and provide a methodology that is applicable to different polymers. Therefore, our input parameters need to incorporate polymer-specific quantities for modeling. Additionally, we need to consider the available computing resources, which impose limitations on system sizes. Lastly, we would like to define one or more control parameters that can alter the fraction of ties and loops in the amorphous regions for a given degree of semi-crystallinity.

3.2.2.1 Parameters of the theory

The mass crystallinity degree χ_c is a crucial parameter in our study. Together with the long period L_p, which represents the period of alternation between amorphous and crystalline phases, we can obtain a length scale. We construct molecular simulation boxes that contain two of these periods, resulting in a box initially containing two crystalline lamellae separated by amorphous regions along the z direction. Full periodicity of the box is assumed in all three directions. Each simulation box contains two polymer chains. The crystalline regions are built using primitive cell information [Bunn, 1939], with an integer number of primitive cells in the x and y directions. The number of unit cells in the x and y directions determines the initial number of stems in the system. The total number of crystalline cells in the z

direction is computed based on the length of the crystalline regions m. For polyethylene (PE), each unit cell in the xy plane contains two crystalline stems.

Unlike the work of Adhikari and Muthukumar, we account for the difference between the densities of the amorphous and crystalline phases, denoted as ρ_a and ρ_c respectively. Here, ρ_a represents the average density of the non-crystalline domain, taking into account the interphase. We set ρ_a to be equal to 0.91 g/cm^{-3}. The crystalline density ρ_c is computed from the unit cell dimensions.

From the definition of the long period:

$$L_p = m + d, \tag{3.40}$$

and the crystallinity degree:

$$\chi_c = \frac{\rho_c m}{\rho_c m + \rho_a d}, \tag{3.41}$$

we obtain the values for the thicknesses m and d:

$$m = \frac{\chi_c L_p}{\chi + (1 - \chi_c)(\rho_c/\rho_a)}, \tag{3.42}$$

$$d = \frac{(1 - \chi_c) L_p}{\chi_c(\rho_a/\rho_c) + (1 - \chi_c)}. \tag{3.43}$$

Adhikari's theory is based on the assumption of an ideal freely-jointed chain. However, to capture the atomistic view, we must incorporate the Kuhn length b, which combines information about the atomistic backbone geometry of the real chain with the freely-jointed segments of the ideal chain.

The Kuhn length b is obtained from the knowledge of the characteristic ratio C_∞, an intrinsic property of the polymer, and the backbone geometry. For polyethylene, we have [Rubinstein, 2007]:

$$b = \frac{C_\infty l}{\cos(\theta/2)}, \tag{3.44}$$

where l is the carbon-carbon bond length and $\pi - \theta$ is the angle between two adjacent bonds along the polymer backbone.

The conversion from n, the number of CH_2 groups, to N, the number of Kuhn segments, is given by:

$$N = \frac{n \cos^2(\theta/2)}{C_\infty}. \tag{3.45}$$

From the total density ρ and the simulation box size, we obtain the chain molecular weight M_w. The parameters and their related quantities are given in Table 3.1.

l (Å)	1.54	
θ (°)	68	
n_{stem}	70	
ρ_a (g/cm^3)	0.91	
ρ_c (g/cm^3)	1	
L_p (Å)	200	
χ_c	0.5	0.7
ρ (g/cm^3)	0.955	0.973
M_w (g/mol)	149432	147668

Table 3.1: *Parameters used to build semicrystalline samples with $\chi = 0.5$ and 0.7. Also indicated are the density of the boxes and the molecular weight of each molecule in the final structures.*

The characteristic ratio C_∞ is the last parameter to be determined. Flory computed the characteristic ratio to be 6.9 at 413 K [Flory, 1989]. The length of the freely jointed segment, i.e., the Kuhn length, influences the fraction of ties in the system, denoted as f_{tie}. By changing the value of the characteristic ratio while keeping the other parameters constant, we can control the relative fractions of different types of walks. We believe that the chains in the amorphous regions are more constrained than in a bulk amorphous system. Additionally, the characteristic ratio was obtained in the melt, at high temperature. Thus, we expect that $C_\infty = 6.9$ represents a lower bound for the characteristic ratio that describes chain segments in a semi-crystalline sample. We will use different characteristic ratios: $C_\infty = 7$, 9, 11, and 13 to generate structures with two different crystallinity ratios, $\chi_c = 0.5$ and 0.7. The corresponding fractions of tie chains are plotted in Figure 3.2.

3.2.2.2 Finding the probability distribution of length of each kind of amorphous chain section (tie chains, loops and tails)

For each structure, we compute the number of tie, loop, and tail chains. We determine the length distribution of the chain sections in the amorphous phase using the probability distributions g_{tie}, g_{loop}, and g_{tail}. The distributions have to be truncated as in Adhikari's formalism they are not bounded towards $s \to +\infty$. In a real system, chain extension must be limited to the physical space allowed between crystalline regions. A coarse way to obtain a range $[1, P]$ of Kuhn segments to bound the probability distribution is to consider the weighted average of the length of tie, loop, and tail chains in Kuhn segments: s^P_{tie}, s^P_{loop}, and s^P_{tail}, and to write the following identity concerning the number of amorphous Kuhn segments $N_a = (1 - \chi)N$.

$$N_a = \bar{n}_{\text{tie}} s^P_{\text{tie}} + \bar{n}_{\text{loop}} s^P_{\text{loop}} + 2 s^P_{\text{tail}} \, . \tag{3.46}$$

$$N_a = \bar{n}_{\text{tie}} \sum_{s=1}^{P} g^P_{\text{tie}}(s) \times s + \bar{n}_{\text{loop}} \sum_{s=1}^{P} g^P_{\text{loop}}(s) \times s + 2 \sum_{s=1}^{P} g^P_{\text{tail}}(s) \times s \, , \tag{3.47}$$

where the g^P_i are the final probabilities used in this study:

$$g^P_{\text{tie}}(s) = \frac{g_{\text{tie}}(s)}{\sum_{s=1}^{P} g_{\text{tie}}(s)} \, , \tag{3.48}$$

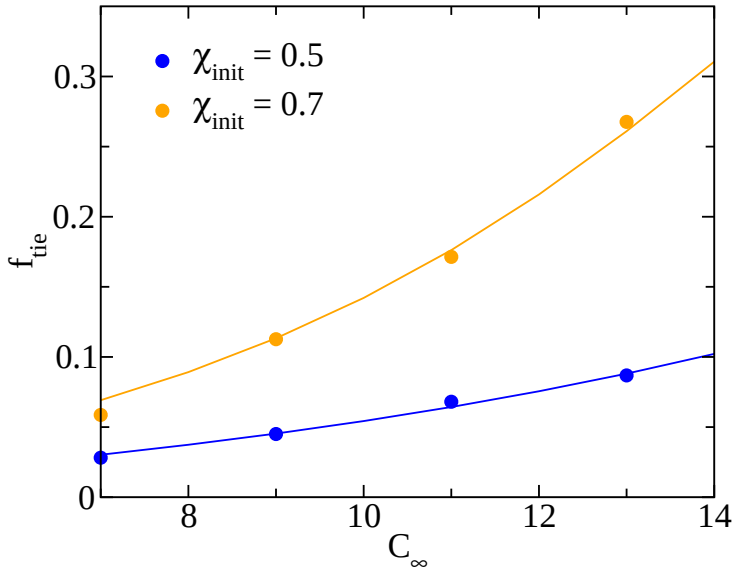

Figure 3.2: *Fraction of tie chains, f_{tie}, as a function of the characteristic ratio C_∞ obtained from the theory (solid lines) and for the samples built in this study (symbols) for the two crystallinity ratios studied here.*

$$g^P_{\text{loop}}(s) = \frac{g_{\text{loop}}(s)}{\sum_{s=1}^{P} g_{\text{loop}}(s)} \,, \tag{3.49}$$

$$g^P_{\text{tail}}(s) = \frac{g_{\text{tail}}(s)}{\sum_{s=1}^{P} g_{\text{tail}}(s)} \,. \tag{3.50}$$

We find the correct P which gives the correct average number of amorphous segments N_a. Those probabilities are discrete probabilities of the number of Kuhn segments per walk in the amorphous phase. From equation (3.45), we express the length of the walks in the amorphous phase according to the number of atoms in the backbone: $n = \frac{NC_\infty}{\cos^2\theta/2}$. We do not want to have only multiples of $\frac{C_\infty}{\cos^2\theta/2}$ for n, thus we interpolate the cumulative distribution functions of the probability distribution functions (3.48), (3.49), (3.50), and a procedure called *Inverse Transform Sampling* was used to randomly pick a number from those non-analytical numerical probability distributions (see Figures 3.3 and 3.4). This procedure is well described in this reference [Devroye, 1986]. It allows picking a number according to a discrete probability distribution as if it were a continuous function.

3.2.2.3 Generation of the amorphous phases according to the statistical theory, connection of the crystalline and amorphous phase, and equilibration

For each structure, we build the crystalline phases using unit cell information and box and region dimensions. We construct two amorphous phases using the MedeA Amorphous Materials Builder [Materials Design inc., a], which is based on the work by Theodorou and Sutter algorithm [Theodorou and Suter, 1985] with the chain sections taken from the probability distributions. The crystalline and amorphous regions are then stacked together.

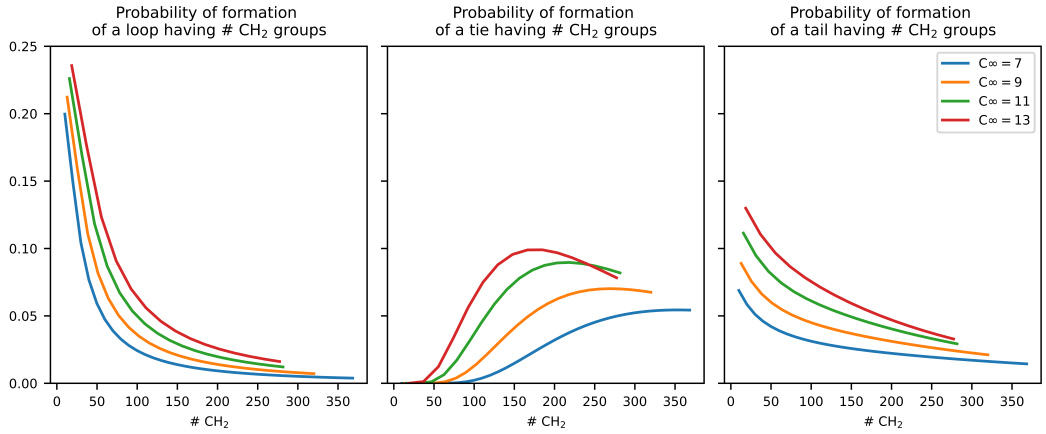

Figure 3.3: *Final probabilities of formation of tie chains, loops, and tails for* $\chi = 0.5$ *and different values of* C_∞.

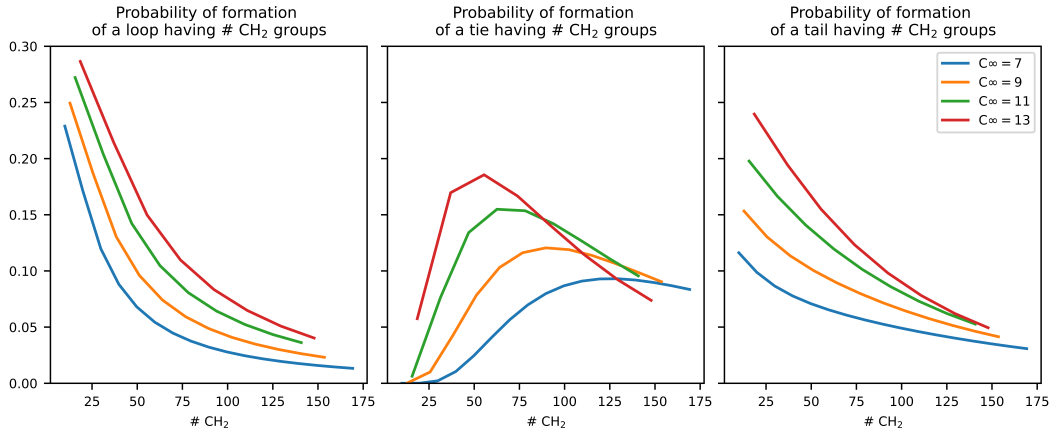

Figure 3.4: *Final probabilities of formation of tie chains, loops, and tails for* $\chi = 0.7$ *and different values of* C_∞.

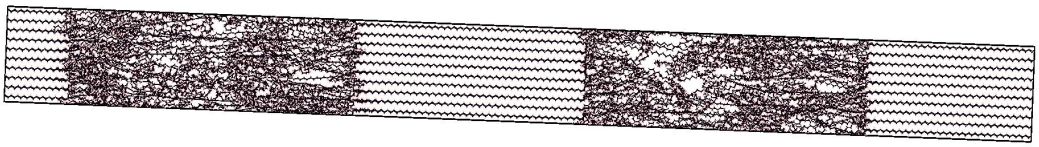

Figure 3.5: *Structure with crystallinity degree $\chi = 0.5$ after connection and before relaxation.*

pseudo-atom	type	ϵ/k$_B$ [K]	σ [Å]
CH3 (1)	[CH3]-CHx	98	3.75
CH2 (2)	CHx-[CH2]-CHx	46	3.95
stretch	type	length [Å]	k$_l$ [K/Å^2]
'1 - 2'	CH_3-CH_2	1.54	269727
'2 - 2'	CH_2-CH_2	1.54	269727
bend	type	theta [°]	k$_\theta$/k_B [K/rad^2]
	CHx-[CH2]-CHy	114	62500

Table 3.2: *Forcefield used to represent the polyethylene molecules*

We label the ends of the chain segments in the amorphous phases according to the desired connections. A tie chain will have one end labeled *A* and the other *B*, a tail chain will have one of the ends only labeled *A* or *B*, loop chains will have both ends labeled with the same letter *A* or *B*. The reactive sites (CH_3) on one edge of the crystallite stems are labeled *C* and those on the other edge *D*.

Then, a connection algorithm is launched, originally designed for thermoset building [Rigby et al., 2016]. The algorithm is a tool of the material simulation software MedeA [Materials Design inc., b] and is named Thermoset builder. Spheres of capture centered on the labeled site grow incrementally with a chosen step. Every time it encounters an allowed connection (here *A* with *C* and *B* with *D*), it forms a bond and performs a few steps of a NVT relaxation. We keep the crystalline phases frozen during the connection process. An example of resulting structure is shown in Figure 7.3.

The structures were thermalized and mechanically equilibrated for 100 ns using LAMMPS [Thompson et al., 2022] and the TraPPE-UA force field [Martin and Siepmann, 1998] (see table 3.2) in the NPT ensemble with $T = 300$ K and $P = 1$ atm, using a time step of 1 fs (see Figure 7.4). The NPT ensemble used here allows relaxation in each spatial direction to ensure the correct equilibration of box lengths in all directions (known as LAMMPS NPT *aniso* mode).

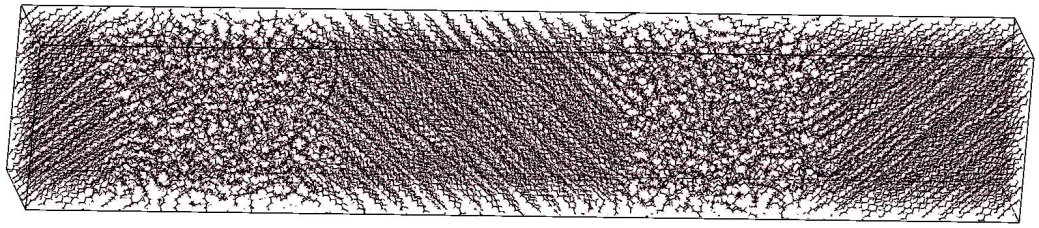

Figure 3.6: *Structure with an initial crystallinity degree $\chi = 0.5$ after relaxation.*

Chapter 4

Characterization of the semicrystalline samples: morphology, entanglements, mechanical properties

4.1 Structural characterization of the samples

4.1.1 27 structures with various building inputs

In this work, 27 structures, i.e. 27 simulation boxes, were generated with different degrees of crystallinity and characteristic ratios (see table 4.1). The chosen degree of crystallinity aims to represent HDPE ($\chi_c = 50$ to 80% and $d = 0.93$ to 0.97 g/cm^3) [Peacock, 2000], the molecular weight (≈ 150000 g/mol) and the initial long period (200Å) is in the range of what is expected from HDPE, it has to be noticed that the molecular weight in HDPE may vary from 10^4 to 10^6 g/mol and the long period from 10^2 to 10^3 Å [Voigt-Martin and Mandelkern, 1984]. The samples correctly model HDPE with "average" characteristics.

4.1.2 Density profile and degree of crystallinity

For all these structures, the degree of crystallinity after relaxation was computed from the density profile along the z axis, normal to the amorphous-crystalline interface (see Fig-

	$\chi_{init} = 0.5$	$\chi_{init} = 0.7$
$C_\infty = 7$	3	3
$C_\infty = 9$	6	3
$C_\infty = 11$	3	3
$C_\infty = 13$	3	3

Table 4.1: *Number of modeled structures for each χ_{init} and C_∞.*

χ_{init}	0.5	0.7
$\overline{\chi}_{relax}$	0.49	0.67
$\sigma_{\chi_{relax}}$	0.05	0.06
$\overline{\rho}_{relax}$	0.939	0.966
$\sigma_{\rho_{relax}}$	0.008	0.006

Table 4.2: *Mean of the degrees of crystallinity χ_{relax}, and of the densities $\bar{\rho}_{relax}$ after relaxation, as well as their standard deviations $\sigma_{\chi_{relax}}$ and $\sigma_{\rho_{relax}}$.*

ure 4.1). A region is considered as amorphous when its density is smaller than 95% the crystalline density value, else it is considered as crystalline. Average values over all structures and corresponding standard deviations are given in table 4.2. Some fluctuations are observed, although the final degree of crystallinity remains within two standard deviations. After equilibration, the amorphous region thickness lies in the range of $64 - 89$ Å for samples having an initial degree of crystallinity equal to 0.5 and $41 - 70$ Å for samples having an initial degree of crystallinity equal to 0.7. Semi-crystalline density after relaxation was also computed for all structures. Values are close from HDPE experimental data: 0.941-0.965g/cm^3[Lange and Speight, 2005]. As expected, a strong correlation can be seen between degree of crystallinity and density (see Figure 4.2).

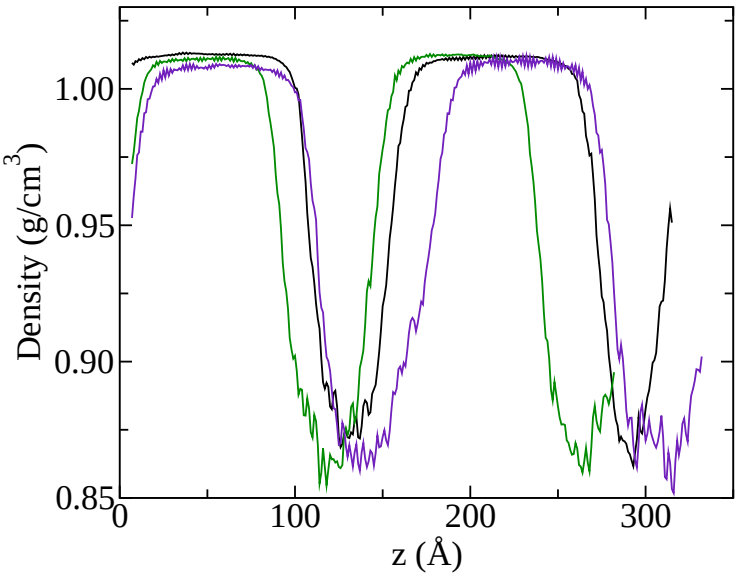

Figure 4.1: *Density profile along the z axis, the axis of the long period, of the 3 structures with $\chi_{init} = 0.7$ and $C_\infty = 7$.*

Thus, we have observed that our structures respect the original constrains imposed by the building procedure for macroscopic observables. We now turn to the analysis of the molecular morphology of the samples, i.e. the amount of the different segment types and an entanglement analysis.

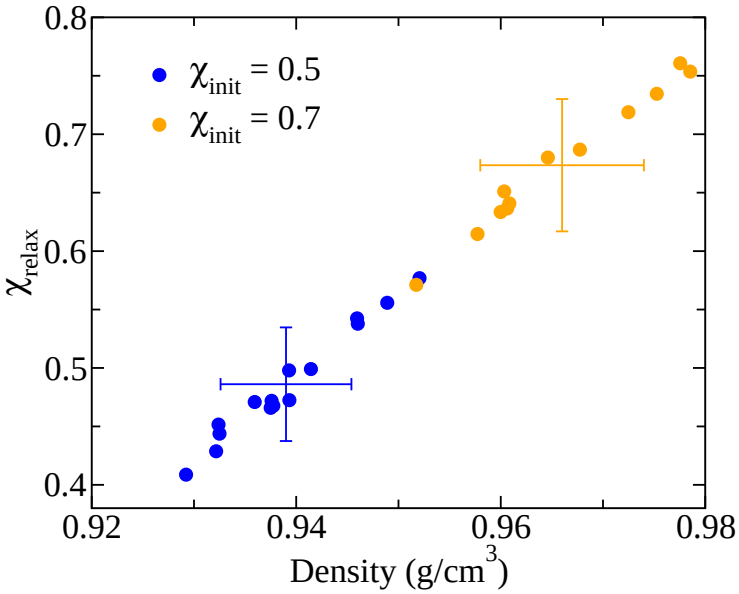

Figure 4.2: *Degree of crystallinity as a function of density for all studied structures. Blue and orange symbols correspond to structures with $\chi_{init} = 0.5$ and $\chi_{init} = 0.7$ respectively. The two crosses indicate the average crystallinity and average density with corresponding standard deviation.*

4.1.3 Respecting the tie fraction imposed during the building construction

Figure 3.2 shows that the expected fraction of ties is well reproduced for each crystallinity at every C_∞ value. The building procedure thus allows a fine control of the imposed structural constraints. Occasionally some connection cannot be performed. However this does not change significantly the imposed characteristics.

4.1.4 Comments on the comparison with alternative building procedures and the question of adjacent reentries

In contrast to the findings in Nilsson's research [Nilsson et al., 2012] and the work by Monasse and Queyroy [Monasse et al., 2008], our study reveals a notable scarcity of small loops, specifically identified as adjacent reentries, averaging just 1 to 2 instances per crystallite edge. This distinction underscores an intriguing aspect of our results.

It is essential to acknowledge the inherent variability in the presence of adjacent reentries within crystallite structures. This variability is intricately tied to the diverse nature of the samples under investigation and the nuanced techniques employed for their characterization as we shown in the bibligraphy section 2.1.3. Importantly, the choice of investigative method often necessitates tailored preparations for each unique sample.

Given the differences we see in the presence of adjacent reentries in crystallite structures across various studies, it's hard to use this alone as a reliable measure to judge the trust-

Figure 4.3: *The primitive paths of chains in an amorphous region computed with the Z1 code [Kröger, 2005], the segments belonging to loops are yellow and red, the segments belonging to tie chains are blue, the tail segments are in green. The spheres represent the primitive path kinks and the ends of the chains.*

worthiness of our model building procedure.

4.1.5 Measuring the entanglements

The Z1 code from Martin Kröger [Kröger, 2005] is used to analyze the entanglements in the amorphous phases of each structure in a similar way that Ranganathan et al. [Ranganathan et al., 2020] did on their semi-crystalline structures. The Z1 code compute the primitive path (defined below), the primitive path nodes are the entanglements. The obtained primitive paths of an amorphous phase (an amorphous region was sliced) is shown in Figure 4.3. The primitive path of a polymer chain immersed in a space of obstacles (usually other polymers) is defined as the shortest path connecting the ends of the chain that does not violate the crossing of the polymer chain [Shanbhag and Kröger, 2007].

The Z1 code principles: All chains are represented by a variable number of nodes, initially coinciding with the atoms of the backbone. During each step of the sequential minimization procedure, the focus is on three adjacent nodes belonging to a particular chain, which are denoted as chain A. These three nodes together form a triangle that encloses an area defined by the surface of the triangle. By utilizing adaptive neighbor lists, the code performs a search for segments from other chains (B, C, etc.) that intersect this area. From the resulting list, a segment is selected that allows for the maximum displacement of one of the nodes within the triangle, ensuring no overlap occurs between the chains as the

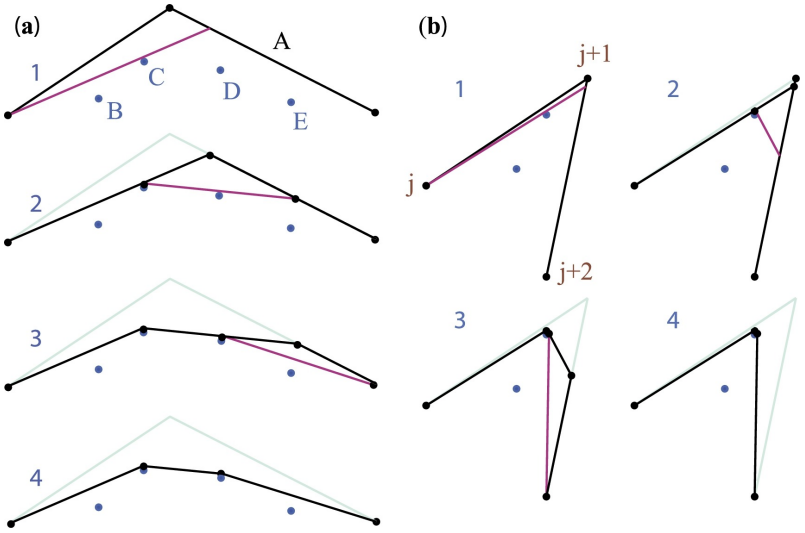

Figure 4.4: *Explanation of Z1 code principles, the figure is extracted from [Kroger et al., 2023].*

displacement proceeds along a straight line (refer to Figure 4.4).

After relaxation, the density of topological entanglements, defined as the number of links between two chain sections along their primitive path per unit volume of amorphous phase, is identical for all degree of crystallinity values, as shown in figure 4.5. An average value around 0.78 entanglements per nm^3 is found, close to the value of 0.64 ± 0.03 nm^3 obtained by Lee and Rutledge [Lee and Rutledge, 2011].

4.1.6 Consistency of the entanglement measures with the theories of Flory-Yoon and Hoffman-Miller

The relationship between crystallization and entanglement remains a subject of ongoing debate. The literature presents two classical theories on this matter:

- Hoffman and Miller [Hoffman and Miller, 1997] propose a viewpoint that hinges on the assumption of gradual crystallization kinetics. They suggest that, as the crystallization process advances, a portion of the entanglements is gradually eliminated from the amorphous regions.
- In contrast, Flory and Yoon [Flory and Yoon, 1978] assert that during the timescale of crystallization, polymer chains are unable to disentangle. Consequently, entanglements become confined to the amorphous domains.

In the Flory and Yoon perspective, all entanglements existing in the molten state become encapsulated within the amorphous phase. As a result, the density of entanglements within the amorphous phase surpasses that within the molten state. Conversely, according to Hoffman and Miller, a portion of entanglements should vanish as crystallization progresses, leading to an entanglement density lower than what the Flory and Yoon model predicts.

This divergence in viewpoints gains support from Bartczak's experimental findings [Bartczak,

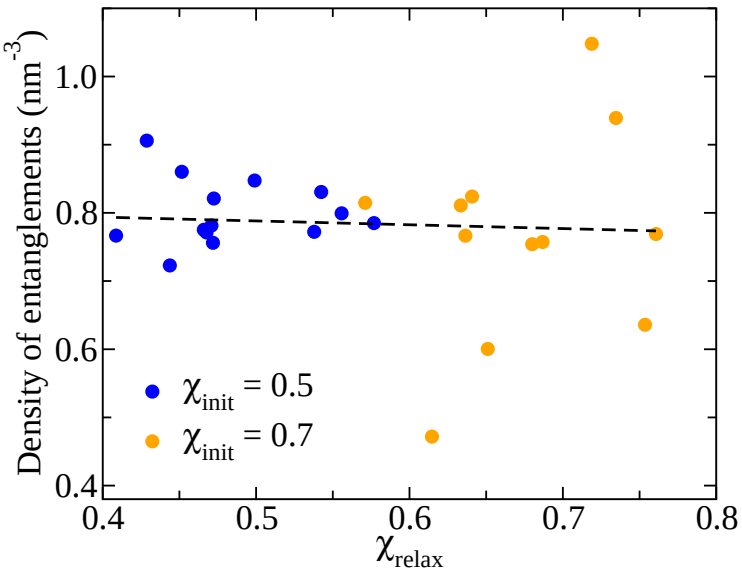

Figure 4.5: *Density of topological entanglements in the amorphous regions as a function of the degree of crystallinity χ_{relax} in all the generated semi-crystalline structures.*

2018]. Bartczak's work demonstrates that a fraction of entanglements resolves during crystallization, with this resolution being influenced by factors like chain length and structural irregularities such as branching. Interestingly, longer chains and increased irregularities both hinder the disappearance of entanglements. Nethertheless, both theories agree that the density of entanglements in the amorphous phase of semicrystalline structures exceeds that in the molten state.

In our specific context, the elevated entanglement density aligns more closely with the Flory and Yoon theory. However, it's worth noting that the process leading to the semicrystalline state in our case deviates from the physical crystallization from a molten state involved in our model building procedure. Despite this unphysical pathway, the key takeaway is that our building procedure still yields a higher entanglement density than the molten state, agreeing with both theoretical frameworks.

The entanglement length expressed in terms of number of CH_2 groups is evaluated with two estimators by the Z1 code: the classical kink entanglement length Ne_{CK} and the classical coil entanglement length Ne_{CC} defined in [Hoy et al., 2009]. Averaged entanglement lengths are given in table 4.3 along with the corresponding entanglement weights W_e^a. Experimental data for entanglement weight in the melt is [Ramos et al., 2008] $W_e^{melt} \approx 800$ to 1200 g/mol, a value two to three times larger than the one observed in our simulations though in agreement with the increase in entanglement density in the amorphous phase.

	Ne_{CK}	Ne_{CC}
mean	23.6	28.9
standard deviation	3.7	7.9
W_e^a (g/mol)	330.5	405.9

Table 4.3: *Mean and standard deviation over all structures of two different estimators developed by Kröger [Kröger, 2005] for the entanglement lengths in amorphous domains expressed in number of CH_2 groups and in molecular weights.*

4.2 Elastic constants

4.2.1 Computing the elastic constants, evolution with the degree of crystallinity

The study focused on three diagonal coefficients of the elastic matrix c_{11}, c_{22} and c_{33}. All structures were uniaxially strained with an engineering tensile strain of $\epsilon = \pm 1\%$ and $\pm 2\%$. The deformation was performed with LAMMPS keeping the normal section constant and imposing an affine transformation of the force centers that matches the box deformation. The results are shown in figure 4.6. As indicated from experimental studies [Addiego et al., 2009], the elastic coefficients increase with the degree of crystallinity.

4.2.2 Anisotropy of the elastic constants: geometrical considerations

The responses to deformations in the $x-$ and $y-$directions are expected to be similar if the crystalline chains are not tilted, i.e., these chains remain aligned to the $z-$direction. This is the case before relaxation (see figure 7.3). In this situation, the $x-$ and $y-$directions are equivalent, the stress arising from the strain imposed in these two directions is not opposed by strong covalent bond forces but instead by relatively weaker van der Waals forces. However, after relaxation, the crystalline stems are tilted in the (y, z) plane (being almost aligned to the (y, z) bisector, see figure 4.7a), whereas no tilt occurs in the (x, z) plane (see figure 4.7b). Taking these geometrical considerations into account, stresses due to deformations in both the $z-$ and the $y-$directions are opposed by strong covalent forces. However, in the $z-$direction, most of the deformation can occur in the amorphous phase, without much change in the crystalline region. On the contrary, when the strain is applied in the $x-$ and $y-$directions, both crystalline and amorphous phases have to be deformed, with some strong covalent forces to oppose for the y-direction case and with weaker van der Waals forces to oppose for the x-direction. That is the reason why $c_{22} > c_{11} \approx c_{33}$. The same behavior was observed by In't Veld and Rutledge [in't Veld et al., 2006].
With the exception of the degree of crystallinity effect, we did not notice any correlation between the elastic coefficients and other morphological specificities such as the amount of tie chains or topological entanglements. Such behavior is expected in the small deformation regime.

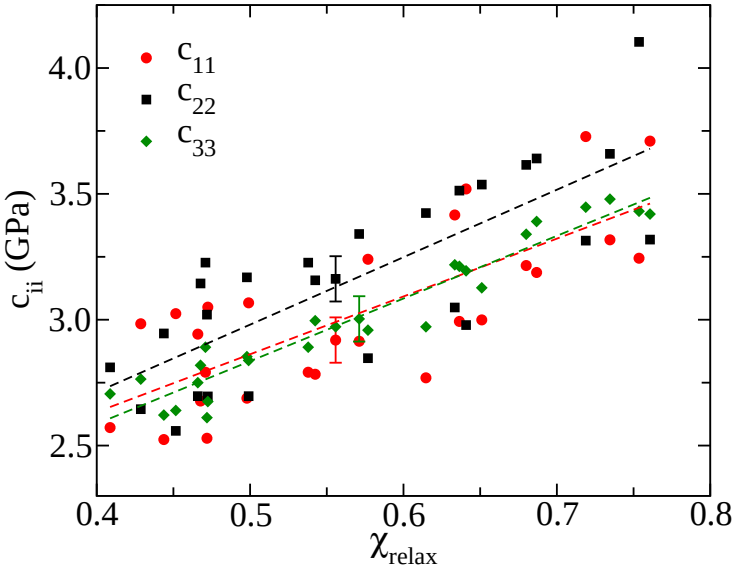

Figure 4.6: *Tensile elastic coefficients c_{ii} as a function of the degree of crystallinity χ_{relax} of all the modeled structures. Error bars are obtained by error propagation from the errors of the internal stress calculated for the strained structures and the largest error bar* is represented once for each coefficient.

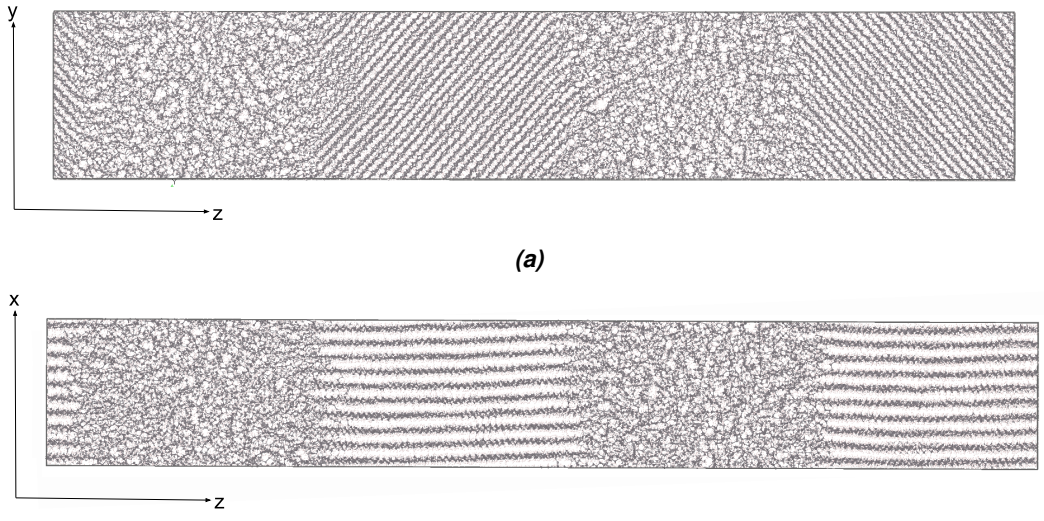

Figure 4.7: *A structure seen from different directions: a. the y direction is vertical, b. the x direction is vertical.*

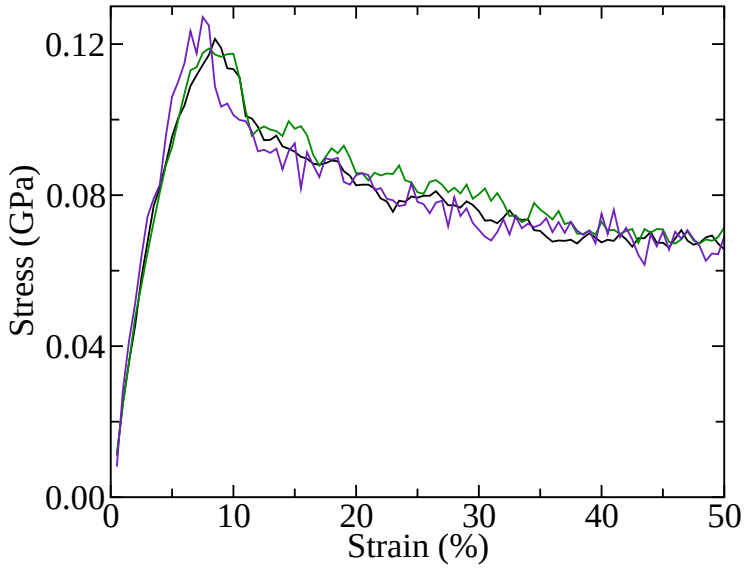

Figure 4.8: *Stress-strain curve for the three structures with* $\chi_{init} = 0.5$ *and* $C_\infty = 11$.

4.3 High deformations

4.3.1 Stress and strain curves

To investigate further the role of entanglements and molecular morphology, the structures were elongated with a strain rate $\dot{\epsilon} = 2.5 \cdot 10^{-3}$ ns^{-1} along the z axis from 0% to 50%. A strain of 0.5% per step was used followed by a relaxation in the NVT ensemble during 2 ns at each step, the xy section is kept constant. The stress-strain curves obtained present a peak between 6 and 8% then a continuous decrease toward a plateau. Examples of such curves can be found in figure 4.8.

4.3.2 Sliding of the chain during the deformation

A typical structure after 50% deformation is shown Figure 4.9. We notice that after such large stretching, crystalline phases are still present. The atoms which were initially in the crystalline phase (respectively in the amorphous phase) are colored in red (respectively in grey). One can notice that the stretching occurs by sliding of the chains. Several atoms previously in crystalline regions now appear in the amorphous phases and inversely. One amorphous region is almost destroyed, with the formation of a cavity and fibrils. This behavior is observed almost systematically in our samples.

4.3.3 The stress transmitters

What is considered to influence the mechanical properties are the so called *stress transmitters* [Seguela, 2005, Takayanagi and Nitta, 1997, Lee and Rutledge, 2011, Bartczak,

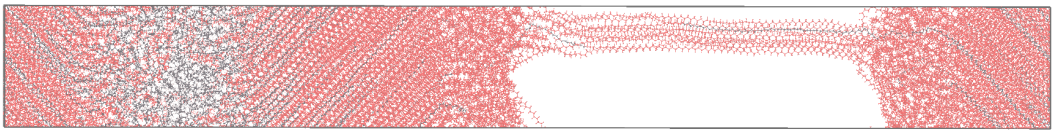

Figure 4.9: *50% stretched structure along the z direction. The red atoms are the atoms which were initially in the crystalline phase.*

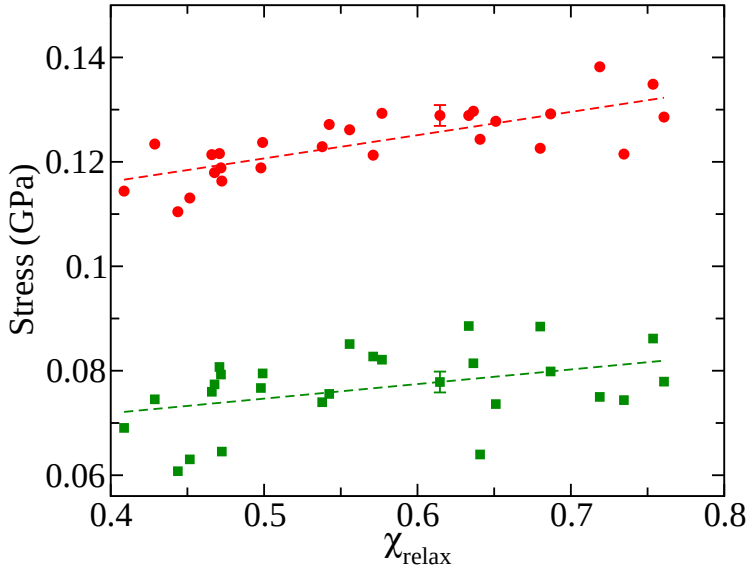

Figure 4.10: *σ_{US} (red dots) and σ_{45-50} (green squares) as a function of the degree of crystallinity χ_{relax}. Dashed lines are linear regressions of each data set. Error bars are stress fluctuations and are given on a single point.*

2018, Moyassari et al., 2015, Jabbari-Farouji et al., 2017]. The term encompasses bridging entanglements and tie chains. Bridging entanglements link polymer chains emerging from two different crystalline phases. We have considered here only loop-loop bridging entanglements, neglecting those including tail chains due to their small number. A loop-loop bridging entanglement is characterized as an entanglement between two loops emerging from different crystalline phases.

To further investigate the high deformations, two criteria were used to characterize the stress-strain curves:

- the ultimate strength σ_{US} being the maximum stress the material withstands along the stress-strain curve,
- the average stress from 45% to 50% strain, σ_{45-50}.

As shown in Figure 4.10, the ultimate strength, σ_{US}, and the average stress between 45 and 50% strain, σ_{45-50}, are increasing with the degree of crystallinity, as observed for the elastic coefficients c_{ii}. σ_{US} and σ_{45-50} are plotted in Figure 4.11 as a function of the number of tie chains and loop-loop bridging entanglements to investigate the importance of the *stress transmitters*. An increase of both stress quantities is expected with an increase

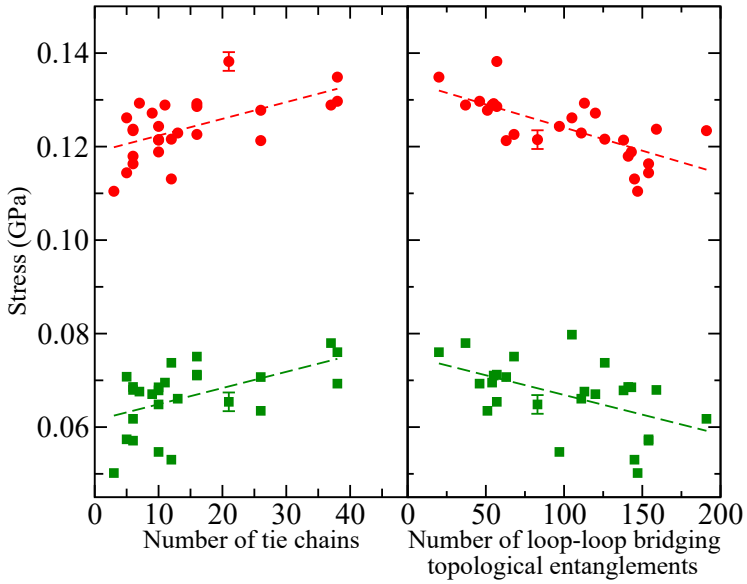

Figure 4.11: *σ_{US} (red dots) and σ_{45-50} (green squares) as a function of the number of tie chains and loop-loop bridging topological entanglements. Error bars are stress fluctuations and are given on a single point.*

of the number of stress transmitters. This increase is indeed observed for σ_{US} and σ_{45-50} versus the tie chain number. However, the opposite trend is observed versus loop-loop bridging entanglement number. The quantity of tie chains is the decisive factor over the entanglements to act as *stress transmitters*. This result confirms recent experimental work by McDermott [McDermott et al., 2020]. It would be however interesting to quantitatively investigate the magnitude of loop-loop entanglements contribution. This implies to control the number of loop-loop entanglements at constant number of other stress transmitters (tie chains). This is not possible as in our building procedure, $\bar{n}_{\mathrm{tie}}$ and $\bar{n}_{\mathrm{loop}}$ are not independent quantities (see Figure 4.12). However when looking qualitatively at structures with the same amount of tie chains in each amorphous region, it is the region with the most loop-loop bridging entanglements which is the least deformed. The bridging entanglements are thus secondary *stress transmitters* after the tie chains.

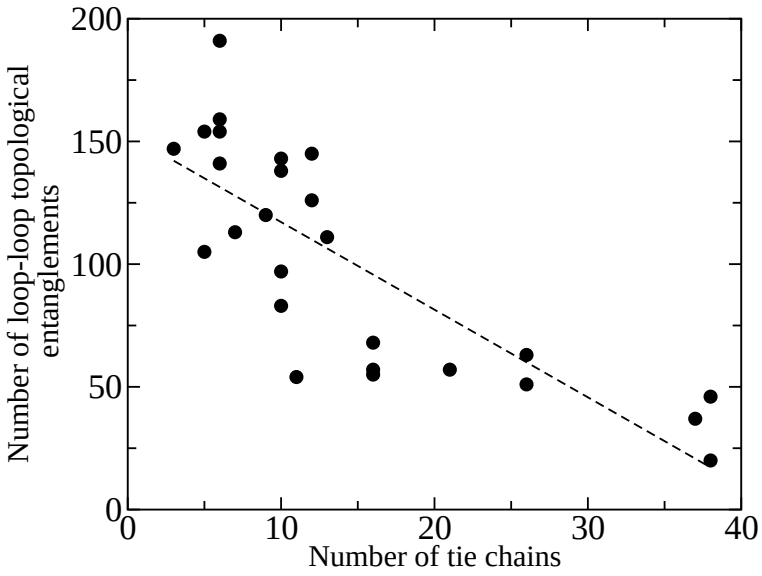

Figure 4.12: *Relationship between the number of tie chains and loop-loop bridging entanglements.*

Chapter 5

Sorption and diffusion

5.1 Introduction

In this section, we present sorption and diffusion computations in semicrystalline polyethylene, focusing on the sorption and diffusion of small gases, specifically CO_2 and CH_4. These properties are evaluated within the structures constructed according to the procedure outlined in Part 3.2.2.3.

The primary parameter used to assess a species' ability to permeate through a polymer membrane is the permeability Pe (as discussed in Section 2.4). It is calculated as the product of two factors: the solubility coefficient S, which measures the loading of a species at a given pressure (and temperature) within the material, and the diffusion coefficient D, representing the species' ability to cross the material.

For solubility computation, we employ the Grand Canonical Monte Carlo method, as described in Part 3.1.3. In this approach, insertion of the species are performed within the polymer matrix. During the simulation, no Monte Carlo moves are conducted on the polymer chains, as sampling the configuration space is challenging in dense polymer materials and would lead to excessively long computation times.

To address the mobility of the polymer chains and potential material swelling, a molecular dynamics run will follow the Monte Carlo run. The Monte Carlo and molecular dynamics runs are repeated in cycles until the concentration of dissolved gas reaches a plateau. This combined approach ensures an accurate assessment of solubility in the semicrystalline polyethylene matrix [Velioglu et al., 2012][Abedini et al., 2017, Velioglu et al., 2018, Kupgan et al., 2018, Balcik and Ahunbay, 2018].

The diffusion coefficient D is computed using the structures with dissolved gas in it, using Einstein equation.

5.2 Computing fugacities

We will employ the Grand Canonical Monte Carlo method to compute solubility coefficients. Instead of directly modeling the gas to be dissolved, this approach utilizes μVT simulations.

In this statistical ensemble, the system exchanges energy with a thermostat, as well as particles with a reservoir, with μ representing the chemical potential of the inserted gas particles in equilibrium with a virtual bath. It quantifies the energy change when adding or removing one particle from the system.

In thermal equilibrium, two systems share the same temperature, while in mechanical equilibrium, their pressures are equal. For diffusive equilibrium, the chemical potentials must be the same. The objective of the Grand Canonical Monte Carlo simulation is to calculate the absorption for a given chemical potential of the virtual bath. To achieve this, we need to compute the chemical potential of the particle bath corresponding to a given pressure. This chemical potential will be utilized in the Boltzmann weights during the Monte Carlo procedure, which samples the configuration space and determines whether to accept or reject the moves of these particles in the polymer matrix.

5.2.1 Widom insertion method

For a system with one specie, the chemical potential may be defined, in the Gibbs ensemble, as:

$$\mu = \left(\frac{\partial G}{\partial N}\right)_{PT} \tag{5.1}$$

It corresponds to the difference in the Gibbs free energy G when adding a particle into the system. The expression for the Gibbs free energy:

$$G(N,P,T) = -k_B T ln\left(\int dV \frac{V^N \exp\left(-\beta PV\right)}{\Lambda^{3N} N!} \int d\mathbf{r}^N \exp\left(-\beta U(\mathbf{r}^N)\right)\right) \tag{5.2}$$

where $\mathbf{r}^N$ is the position vector of the particles, V is the volume, $\Lambda = h/\sqrt{2\pi m k_B T}$ the De Broglie thermal wavelength, $\beta = \frac{1}{k_B T}$, and U the potential of interaction. When N is large, using the definition of the chemical potential:

$$\mu = G(N+1,P,T) - G(N,P,T) \tag{5.3}$$

$$= -k_B T \ln < \frac{V}{\Lambda^3 (N+1)} \exp(-\beta \Delta U) > \tag{5.4}$$

$$= -k_B T ln(k_B T/P\Lambda^3) - k_B T ln < \frac{PV}{(N+1)k_B T} \exp(-\beta \Delta U) > \tag{5.5}$$

$$= \mu_{ideal}(P) + \mu_{excess}(P) \tag{5.6}$$

In the last line, the chemical potential was separated into an ideal gas contribution and an excess part due to interactions. We can write:

$$\mu_{\text{excess}}(P) = -k_B T ln < \frac{PV}{(N+1)k_B T} \exp(-\beta \Delta U) > \tag{5.7}$$

Here, $< ... >$ represents NPT ensemble averaging over the configuration space of the N-particle system. An NPT Monte Carlo is performed on the system of N particles. At frequent intervals, a particle is inserted, and ΔU is computed. The move is never accepted, but the difference in energy allows us to compute the average of the exponential.

Instead of using the chemical potential, the fugacity, which has the dimension of pressure, is often used. It encodes the same information.

5.2.2 Fugacities

The chemical potential (μ) defined this time from the Gibbs free energy is:

$$\mu = \left(\frac{\partial G}{\partial N}\right)_{TP} \tag{5.8}$$

$$d\mu = dG_m = -S_m dT + V_m dP \tag{5.9}$$

Here, T and P represent the temperature and pressure, respectively, G_m is the molar Gibbs energy, V_m is the molar volume, and S_m is the molar entropy. For an ideal gas, the volume per mole is given by:

$$V_m^{\text{ideal}} = \frac{RT}{P} \tag{5.10}$$

where R is the ideal gas constant. In an isothermal process, we can simplify the equation further:

$$d\mu = V_m dP = RT\frac{dP}{P} = RTd\ln P \tag{5.11}$$

However, for real gases, the equation of state departs from this simple form, and the ideal gas law is only a good approximation under certain conditions. These conditions include the negligible size of molecules compared to the average distance between them and the insignificance of short-range inter-molecular potential interactions. Real gases behave like ideal gases at low pressures and high temperatures [Zumdahl and Zumdahl, 2012]. At moderately high pressures, attractive interactions between molecules reduce the pressure compared to the ideal gas law. At very high pressures, the sizes of the molecules become significant, leading to increased pressure due to repulsive forces between molecules. At low temperatures, molecules are more likely to stick together instead of rebounding elastically [Clugston and Flemming, 2000].

To describe the behavior of real gases, even at non-ideal conditions, the ideal gas law can be modified by introducing the concept of fugacity (f), defined as:

$$d\mu = RTd\ln f \tag{5.12}$$

and

$$\lim_{P\to 0}\frac{f}{P} = 1 \tag{5.13}$$

At low pressures, f is approximately equal to the pressure. f share the same units as pressure. Considering a reference state with a zero superscript, integrating the equation for the chemical potential gives:

$$\mu - \mu_0 = RT\ln\frac{f}{P_0} \tag{5.14}$$

atoms	type	ϵ/k_B [K]	sigma [Å]	charge [e]
C (1)	O=(C)=O	27	2.8	0.7
O (2)	(O)=C=O	79	3.05	-0.35
O (3)	O=C=(O)	79	3.05	-0.35
stretch	type	length [Å]		
1 - 2	O=(C=O)	1.16		
2 - 3	O=(C=O)	1.16		
bend	type	θ [°]		
2 - 1 - 3	O=(C)=O	180		

Table 5.1: *Forcefield parameters of the rigid CO_2*

(pseudo)atom	type	ϵ/k_B [K]	sigma [Å]	charge [e]
CH4	CH4	148	3.73	0

Table 5.2: *Forcefield parameters of the rigid CH_4*

Alternatively, this equation can be expressed using the dimensionless quantity $a = \frac{f}{P_0}$, known as the activity.

When the chemical potential μ (i.e., the fugacity f) is computed for a gas at a given pressure, it can be utilized in a Grand Canonical Monte Carlo to compute sorption properties. At chemical equilibrium, the chemical potential is equal in the system where we absorb particles and in the particles reservoir.

5.2.3 Fugacities results

We conducted fugacity calculations for CH_4 and CO_2 at 300 K, exploring a range of pressures from 1 MPa to 40 MPa. The gas molecules were modeled using the TraPPE-UA forcefield [Eggimann et al., 2014], where UA signifies United-Atom, implying that hydrogens are not explicitly represented but rather integrated into the larger atom they are bonded to. For CO_2, a rigid model was utilized, neglecting stretching or bending, and the relevant parameters can be found in table 5.1. Conversely, CH_4 was modeled as a simple bead dressed with a Lennard-Jones potential (table 5.2). The Monte Carlo move probabilities are provided in table 5.3.

During the simulation, we first allowed the system to equilibrate over 2×10^6 steps and then performed a production run for 6×10^6 steps to obtain the fugacities.

Rigid translation	Rigid rotation	Insertion test	Volume moves
0.33	0.33	0.31	0.03

Table 5.3: *Probability of the moves for the Windom insertion test computation for CO_2, the probabilities are the same for CH_4 minus the rotation.*

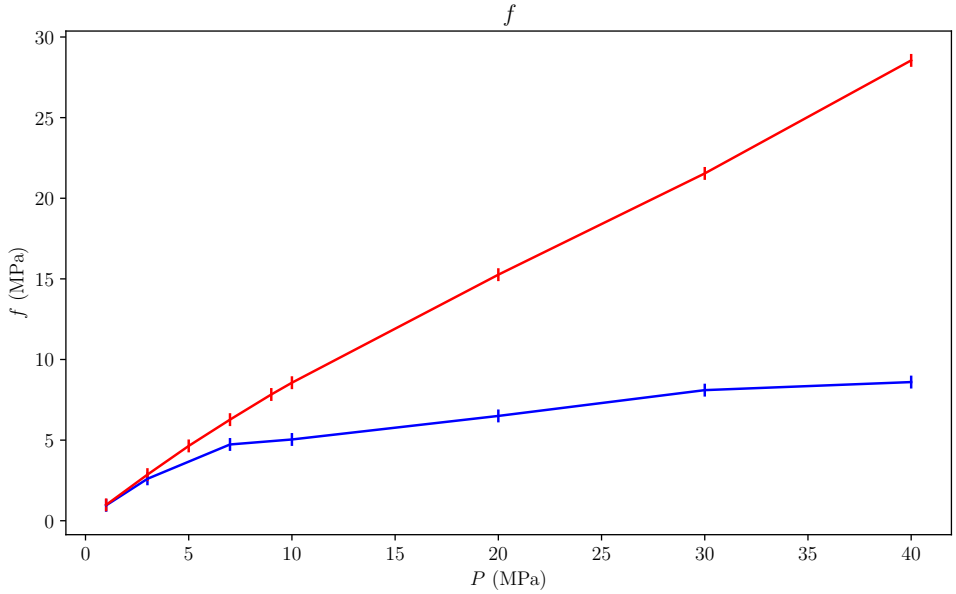

Figure 5.1: *Fugacities of CO_2 and CH_4 computed with Widom insertion test. The top red structure concerns CH_4, the bottom blue structure concerns CO_2.*

5.3 Sorption of CO_2 and CH_4 in semicrystalline polyethylene

5.3.1 Methods: Monte Carlo - Molecular Dynamics cycles, amorphous fraction, averaging

To improve the efficiency of our simulations, the Grand Canonical Monte Carlo method was used, treating the polymer matrix as a solid due to the difficulty to sample polymer configuration with Monte Carlo. To further enhance the simulation speed, a precalculation approach for the potential energies was implemented. This involved calculating the potential energies on a grid of points separated by 0.3 Å in the three spatial directions, enabling us to efficiently interpolate values at any specific point during the simulation and optimize overall computational efficiency.

To account for the swelling effect and the mobility of the polymers caused by the presence of gas molecules, each Monte Carlo run was followed by a Molecular Dynamics run. This sequence of Monte Carlo runs and Molecular Dynamics runs was repeated until a plateau was reached for the gas concentration in the polymer matrix.

This procedure was used with success by various authors [Velioglu et al., 2012, Abedini et al., 2017, Velioglu et al., 2018, Kupgan et al., 2018, Balcik and Ahunbay, 2018].

5.3.1.1 Description of the Monte Carlo run

The Monte Carlo move probabilities are straightforward and only concern the gas molecule (table 5.4). There are two successive runs, one is done with 500000 steps, then a second one with 3000000 steps, the average number of dissolved molecules from the second run is

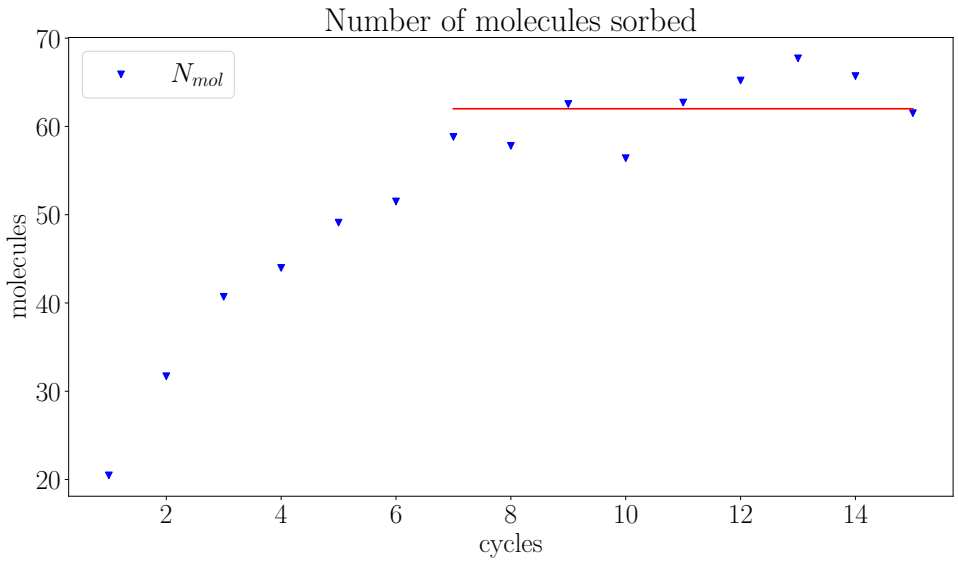

Figure 5.2: *The Figure is an example of the resulting number of molecules at each MC-MD cycle for a given simulation box. The red line represents the average taken on the final plateau.*

the one considered.

Insertion/deletion	translation	rotation
1/3	1/3	1/3

Table 5.4: *Probabilities for the Monte Carlo moves related to the CO_2, for CH_4 being represented as a single bead, there is no rotation.*

5.3.1.2 Molecular Dynamics run (NPT)

The NPT run enables us to consider the swelling of the system and the potential reorganization of the polymer chains caused by the presence of dissolved gas molecules, such as the melting/crystallization of the edges of the crystalline phase. The NPT run is performed with the Nosé-Hoover combined barostat and thermostat using LAMMPS, as described in section 3.1.2.5, for a duration of 500 ps.

5.3.1.3 Reaching a plateau

The Monte Carlo and Molecular Dynamics runs are successively performed up to 25 times. At low pressure, convergence is quickly reached, at high pressure more cycles are required. An average of dissolved molecules is taken on a plateau (refer to Figure 5.2) when the number of molecules stops to monotonically increase and start to fluctuate, the example is given in one structure for CH_4 MC-MD absorption cycles.

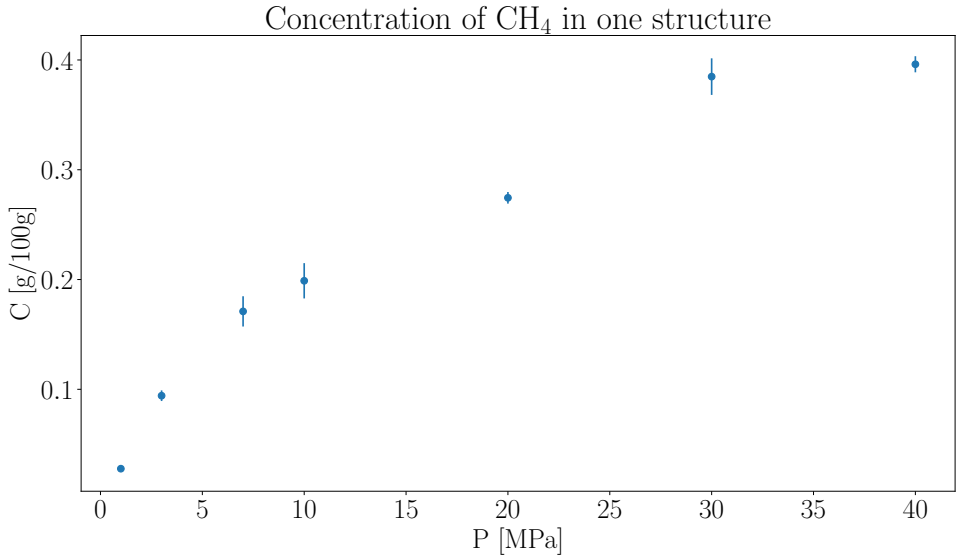

Figure 5.3: *Absorption curve of CH_4 in a semicrystalline polymer simulation box for a structure with $\chi_c = 60.1\%$ the density criterion used to separate the amorphous phase and the crystalline phase is $d_{crit.} = 0.93$ g/cm^3 here, the error-bar is given with a confidence of 98.8% using the different values of number of molecules taken on the plateau.* ***Remark:*** *This confidence interval does not take into account that the choice of the "plateau" zone may be imprecise with a loose criterion which is a limitation of the present method.*

5.3.1.4 Concentration vs Pressure (fugacity)

From this information, we compute the mass concentration of dissolved gas in the polymer matrix in g/(100g of polymer). An example of the resulting absorption curve is given in Figure 5.3.

5.3.1.5 Sorption in the amorphous fraction ϕ_a

When experimentalists are providing numerical values for the concentration or the solubility coefficient, as explained in the bibliography section 2.4.1, it is needed to convert theses values into the concentration or the solubility in the amorphous phase to compare results obtained from samples with different crystallinity degrees. Indeed, Michaels showed that the solubility coefficient (or the concentration) linearly decreases with the degree of crystallinity [Michaels and Bixler, 1961b]:

$$C_a = \frac{C}{\phi_a} \tag{5.15}$$

where ϕ_a is the volumic degree of amorphous phase, C the concentration in all the structure and C_a the concentration in the amorphous phase. The amorphous fraction is measured with two main methods, one is using the X-ray powder diffraction, separating the contribution due to the crystalline phase and the amorphous phase, others are using calorimetric measurements [Goderis et al., 1999, Ryan et al., 1994]. It is not clear what precisely measures the two methods. Sometimes authors are only giving the density from which you can infer the degree of crystallinity.

To discriminate between the amorphous and crystalline regions, we used a density crite-

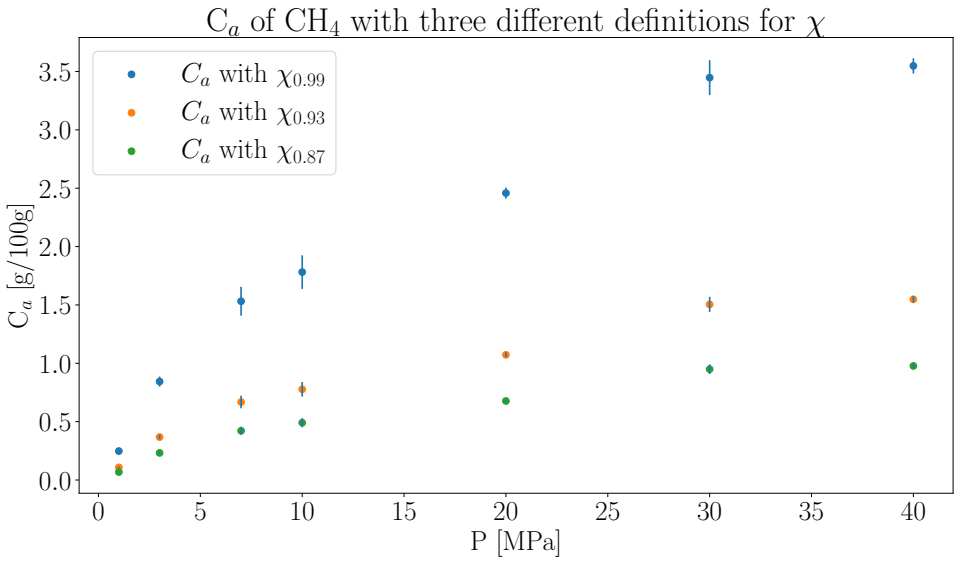

Figure 5.4: *The figure represents the concentration of CH_4 in the amorphous phase in the same structure as in Figure 5.3 for three definitions of the separation between the amorphous phase and the crystalline phase.*

rion. The interphase is perpendicular to the z-axis, the long period axis, in all the simulated structures. Computing the density in slices perpendicular to the z-axis indicates us if we are in the crystalline phase (≈ 1 g/cm^3) or in the amorphous phase (≈ 0.86 g/cm^3). It is not obvious how to correlate the fraction of amorphous given by the experimentalists and the density criterion used in this study due to the quite large transition zone in the interphase. As an example, the concentration in the amorphous C_a is given with three different criterions separating the amorphous phase and the crystalline phase in Figure 5.4: 0.87 g/cm^3, 0.93 g/cm^3 and 0.99 g/cm^3. The first definition integrates most of the interphase in the crystalline phase, the second cuts the interphase in two parts, the last definition integrates the interphase in the amorphous phase. We chose to use the intermediate density $d = 0.93$ g/cm^3, it is not exactly the same definition that was used in the part 4.1.2.

5.3.1.6 Averaging over multiple structures

In order to mitigate the impact of local events arising from the relatively modest sample sizes and to achieve a smoother representation of sorption curves across all molecules, we opted for an averaging approach. This involved averaging the outcomes across two distinct categories, specifically $\chi_{init} = 50\%$ and $\chi_{init} = 70\%$, for all structures (see Figures 5.5 and 5.6).
It is essential to acknowledge that real semicrystalline samples exhibit not a solitary long period or a singular degree of crystallinity ϕ_a (the picture obtained from AFM measurement shows us that [Savage et al., 2015]). Instead, they encompass diverse distributions of these parameters. The justification for averaging across the different cells stems from this standpoint.

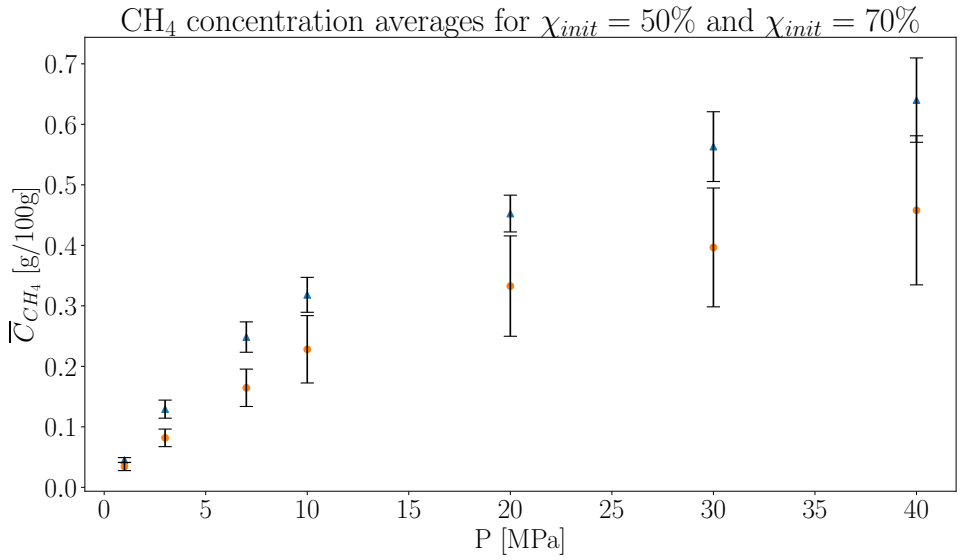

Figure 5.5: *Average concentration of CH_4 in the two initial degrees of crystallinity (in triangles $\chi_{init} = 50\%$, in circles $\chi_{init} = 70\%$), in average the final degree of crystallinity with the chosen definition ($d = 0.93$ g/cm^3 as the limit between the two phases) is 51% and 71%.*

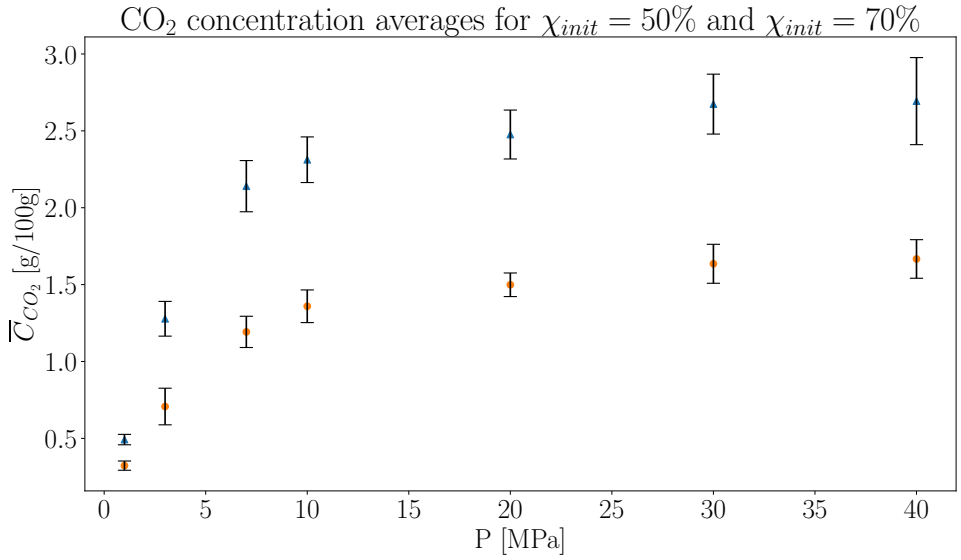

Figure 5.6: *Average concentration of CO_2 in the two initial degrees of crystallinity (in triangles $\chi_{init} = 50\%$, in circles $\chi_{init} = 70\%$), in average the final degree of crystallinity with the chosen definition ($d = 0.93$ g/cm^3 as the limit between the two phases) is 51% and 71%.*

5.3.2 Sorption results

5.3.2.1 Concentration

The results of the concentration in the amorphous phase are given in Figures 5.7 and 5.8. The definition of the amorphous fraction is the one given in the above section.
Within the range of crystallinity that our computations consider, the relationship proposed

by Michaels et al.[Michaels and Parker, 1959] $Sa = \frac{S}{\phi_a}$ or $Ca = \frac{C}{\phi_a}$ is in excellent agreement with our results.
Few authors have provided sorption curves for the two penetrants studied at the temperature under which our computations were performed, Von Solms et al. [Von Solms et al., 2004], the dissertation thesis of Hu [Hu, 2018] and Flaconnèche results[Flaconneche et al., 2001] were used to compare our results. Von Solms, Hu and Flaconnèche results had to be corrected to obtain the concentration in the amorphous phase only, we either used the crystallinity directly given by the authors or when not provided the crystallinity infered from the density. For both the curves, the order of magnitude is correct.
The Von Solms results are in partial agreement with our computations for CH_4, somewhat below.
For CO_2, under 20 MPa, all our results are in good agreement with the available experimental data point. Von Solms and Flaconnèche results are in very good agreement with each other. Above 5 MPa, only the Hu's dissertation thesis is providing data points. The continuity between the congruent Von Solms and Flaconnèche points on one hand, and Hu points on another hand suggest that Hu's work is reliable. It seems, that the higher the pressure, the more below our computations are compared to Hu's results. In previous work, using this methodology with Monte-Carlo and Molecular Dynamics cycles [Velioglu et al., 2012, Abedini et al., 2017, Velioglu et al., 2018, Kupgan et al., 2018, Balcik and Ahunbay, 2018], the max pressure used for the sorption was 5 MPa. An hypothesis is that at higher pressure the lack of coupling between the mobility of the polymer chains and the sorbed penetrants does not allow a complete loading of penetrants.
As we explained, very few authors provide sorption curves, most provides only Henry constants which we can compare too with our results in the next section.

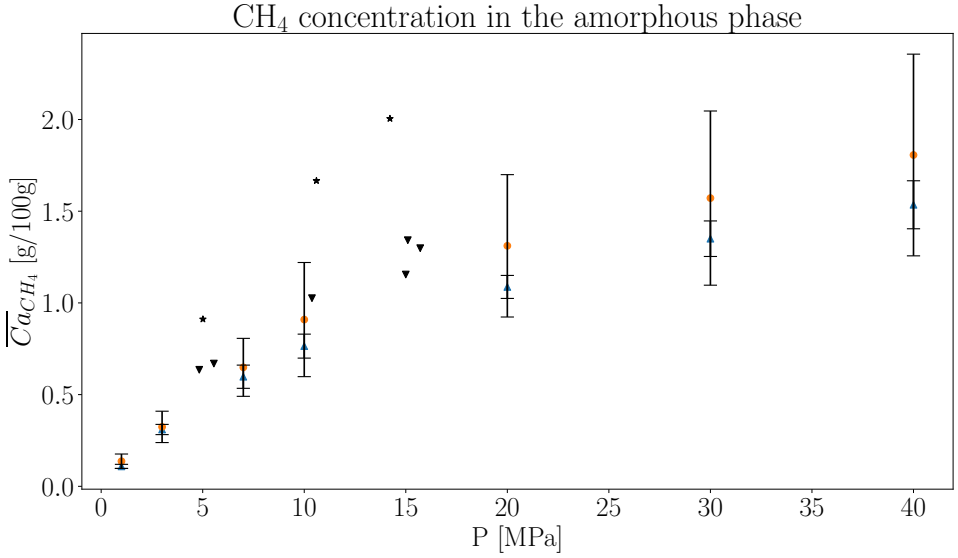

Figure 5.7: *The average concentration of CH_4 in the amorphous phases in the two initial degrees of crystallinity with the chosen definition ($d = 0.93$ g/cm^3 as the limit between the two phases). The experimental measures of Von Solms are given too[Von Solms et al., 2004] and labeled with reversed triangle (▾, $T = 305$ K) and stars (⋆, $T = 298$ K). The computational results are labeled with blue triangles ($\chi_{init} = 50\%$) and orange circles ($\chi_{init} = 70\%$) both at $T = 300$ K.*

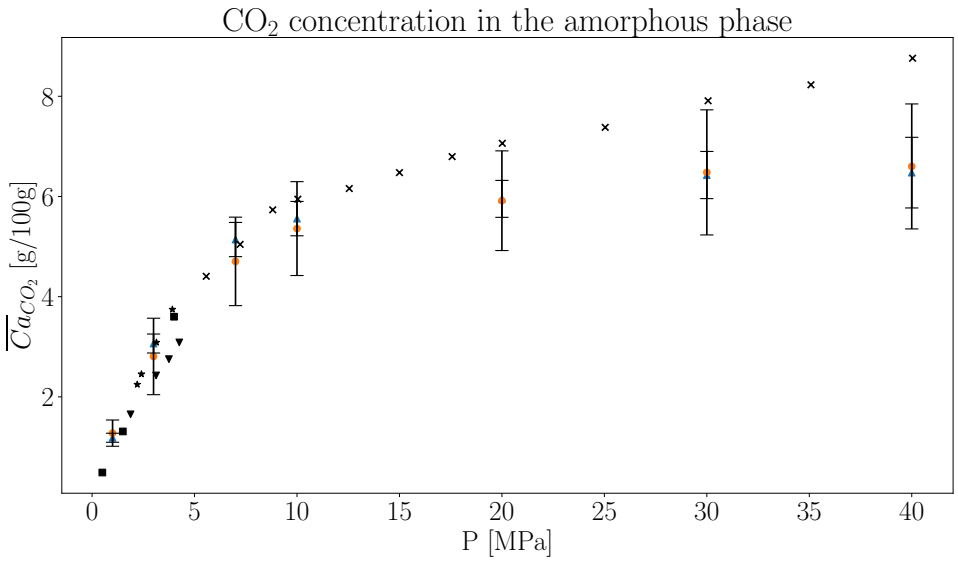

Figure 5.8: *The average concentration of CO_2 in the amorphous phases is determined for the two initial degrees of crystallinity, with $d = 0.93$ g/cm^3 serving as the boundary between the two phases. The experimental measurements from Von Solms [Von Solms et al., 2004] are represented as reversed triangles (▼, $T = 305$ K) and stars (⋆, $T = 298$ K). Flaconnèche et al. [Flaconneche et al., 2001] results are shown as squares (■, $T = 298$ K), and Hu's results are denoted by crosses (×, $T = 298$ K). The computational results are labeled with blue triangles ($\chi_{init} = 50\%$) and orange circles ($\chi_{init} = 70\%$) both at $T = 300$ K.*

5.3.2.2 Henry constants

The solubility coefficients in the amorphous fraction, denoted as S_a, were determined by dividing the concentration by the fugacities: $S_a = C_a/f$. These values are depicted in Figures 5.9 and 5.10. We no longer distinguish between the two initial degrees of crystallinity since we have demonstrated that Michaels' equation ($S = \phi_\alpha S_a$) is valid in our structures, and S_a is averaged over all the structures. Starting at 7 MPa, the error bars for solubility no longer overlap with the 1 MPa point. Only the 1 MPa and 3 MPa data points can be considered within the Henry's domain.
Memari et al.[Memari et al., 2010] compiled all the available Henry constants results measured in HDPE for CH_4 and CO_2. There were no new results available in the literature for the studied gases at the given temperature. All the available experimental constants were represented in the figures as dotted lines. Michaels' results [Michaels and Bixler, 1961b] were obtained at pressures below 0.1 MPa. In Naito's work [Naito et al., 1991], the determination of the Henry constants was carried out at higher pressures, with results fitted using an equation that separates the specific contribution of the Henry sorption mode. Ash et al. [Ash et al., 1970] measured the concentration slope up to 0.3 MPa. Von Solms obtained the solubility coefficients from the points shown in Figures 5.7 and 5.8 at higher pressures, which may lead to deviations from the Henry's domain; thus, the provided solubility coefficients are the lowest.

Flaconnèche results were acquired at higher pressures compared to Michaels, Naito, and Ash, but lower than Von Solms, resulting in an intermediate value for the solubility coefficient. Togawa et al. [Togawa et al., 2001] utilized a more accurate method that minimizes gas loss, and they conducted experiments at very low pressures, leading to higher results.

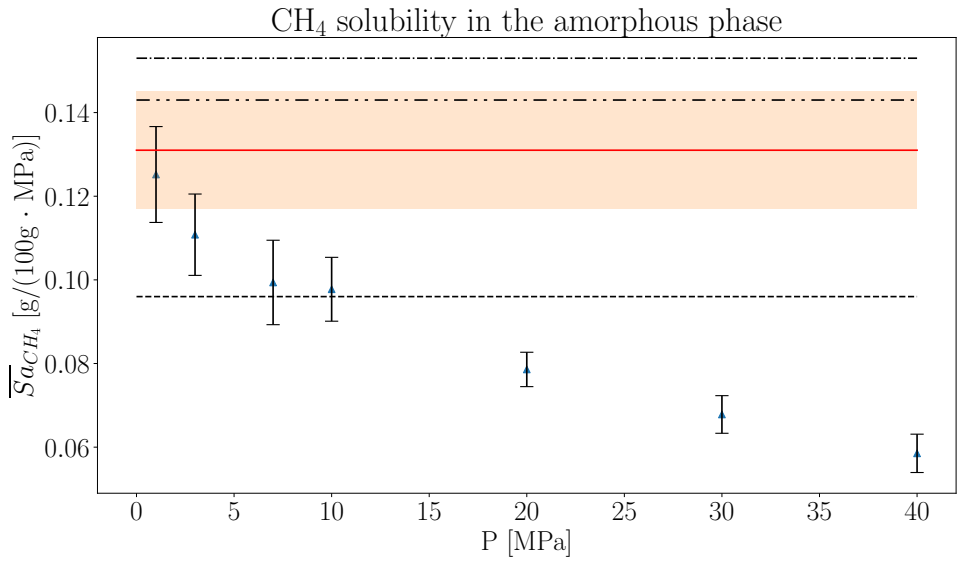

Figure 5.9: *The average solubility coefficient of CH_4 in the amorphous fraction ($d = 0.93$ g/cm^3, marking the boundary between the two phases) is presented in the figure. The experimental measurements are indicated by dotted or dashed lines, arranged from top to bottom as follows: Michaels [Michaels and Bixler, 1961b], Naito [Naito et al., 1996], and Von Solms [Von Solms et al., 2004]. The red line represents the average of the Henry constants found in the literature, and the colored rectangle represents the standard deviation of the experimental results. The error bars are calculated from the results obtained across all our structures, using a margin of 2.5σ.*

For both curves, even though the error bars of the first two computed points slightly overlap (at 1 and 3 MPa), it's important to consider that the experimentalists who conducted measurements at lower pressures provided higher solubility constants compared to Von Solms, who conducted measurements at higher pressures (approximately 2 to 5 MPa for CO_2 and 5 to 15 MPa for CH_4). Therefore, it is advisable to utilize the first computed point at 1 MPa when comparing our calculations with experimental results to ensure that we remain closer to the Henry's domain and minimize deviations.

For CH_4, when we include Von Solms' results in our comparison, our computations are highly consistent with the experimental results. Given that Von Solms' results may potentially underestimate the solubility, it is possible that our computed solubility coefficient might be slightly lower than the actual value. In either case, our results provide validation for the forcefields, semicrystalline models, and the sorption method used.

For CO_2, our computed solubility coefficient is slightly higher than the average of the experimental values. However, it's worth noting that our error bar includes Togawa's more accurate result. In summary, the forcefields, the semicrystalline model, and the sorption method employed are validated by the experimental results.

5.3.2.3 Swelling

Figures 5.11 and 5.12 depict the mass density of the polymer during the sorption process, excluding the sorbed mass density. The swelling effect is nearly negligible for CH_4. In the case of CO_2, we can observe a competing effect: initially, sorption causes the polymer to

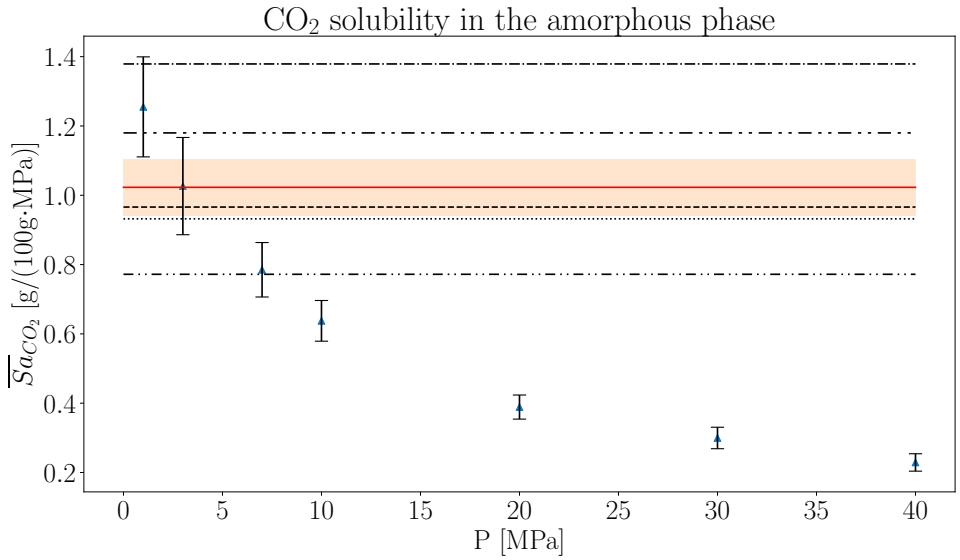

Figure 5.10: *The average solubility coefficient of CO_2 in the amorphous fraction ($d = 0.93$ g/cm^3, denoting the boundary between the two phases) is illustrated in the figure. The experimental measurements are represented by dotted or dashed lines, ordered from top to bottom as follows: Togawa [Togawa et al., 2001], Ash [Ash et al., 1970], Naito [Naito et al., 1996], Michaels [Michaels and Bixler, 1961b], Flaconnèche [Flaconneche et al., 2001], and Von Solms [Von Solms et al., 2004]. The red line corresponds to the average of the Henry constants found in the literature, and the colored rectangle denotes the standard deviation of the experimental results. Our computational results are presented as small triangles, and the error bars are determined from the results obtained from all our structures using a margin of 2.5σ.*

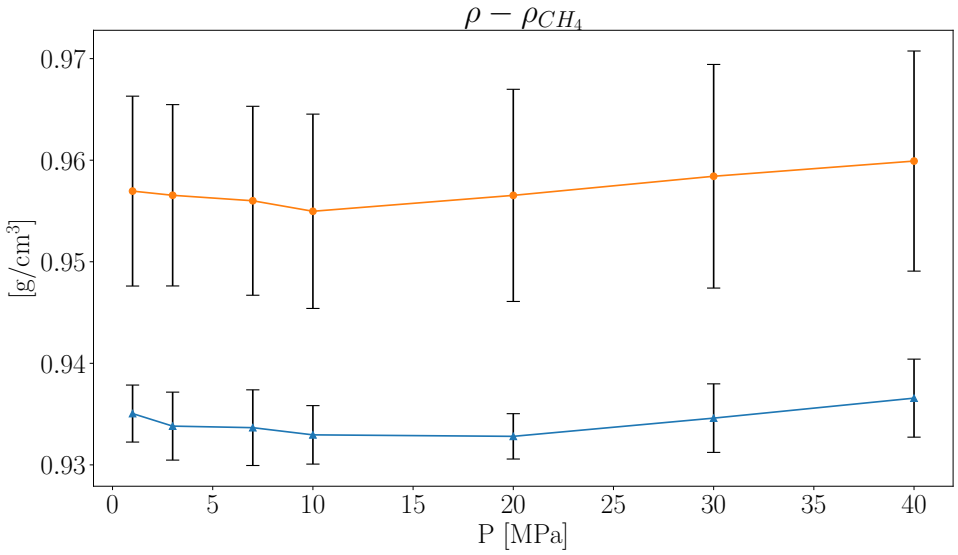

Figure 5.11: *Average mass density of the polymer without the sorbed CH_4 in the amorphous phases with the two initial degrees of crystallinity (at the top, $\chi_{init} = 70\%$, at the bottom $\chi_{init} = 50\%$).*

expand up to 10 MPa, and then the influence of hydrostatic pressure begins to compress the semicrystalline matrix. This aligns with Naito's phenomenological theory of diffusion [Naito et al., 1991], which suggests that diffusion increases due to a plasticizing effect and subsequently decreases because of the influence of hydrostatic pressure. This also serves as a smooth transition to the next section on diffusion.

5.4 Diffusivity

5.4.1 Method

5.4.1.1 Initial configuration

Molecular dynamics simulations conducted to determine the diffusion coefficient make use of the results from sorption computations. From the configurations generated during the Monte Carlo and Molecular dynamics cycles, the one with the number of sorbed molecules closest to the average over all the "plateau" cycles is selected for each pressure and structure under consideration. To prepare these structures for the diffusivity calculation, an NPT run is conducted at the specified pressure. The average cell parameters obtained from the NPT run are used to adjust the simulation box size, ensuring that the density corresponds to the desired pressure.

The structures are then further relaxed in the NVT ensemble to assign the appropriate velocities to the molecules in accordance with the specified temperature ($T = 300$ K). Following this, the NVE run dedicated to computing the diffusion coefficient commences. Although it's possible to use an NVT run for diffusion coefficient calculations, it's important to note that the thermostat, which dynamically adjusts the velocities of the molecules to maintain the correct temperature, may impact the displacements of the molecules used for

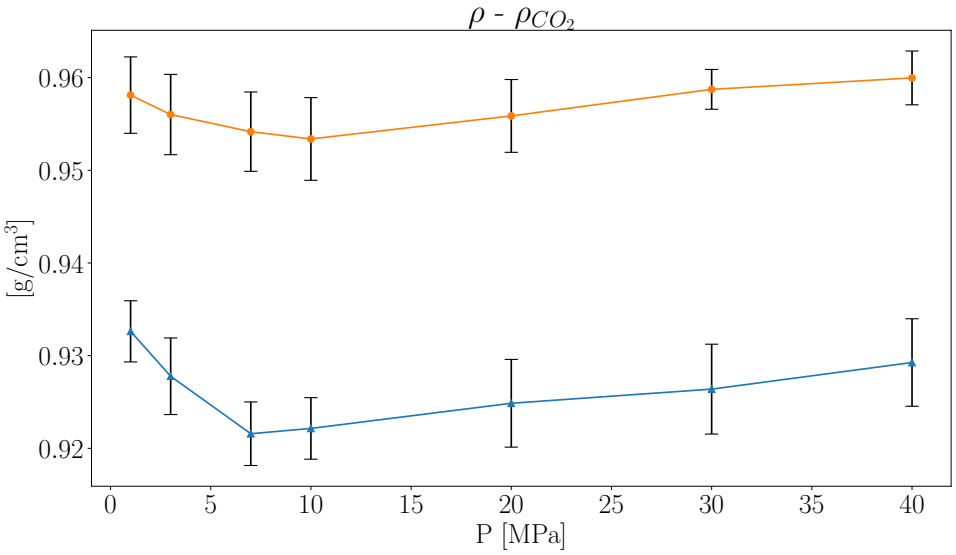

Figure 5.12: *Average mass density of the polymer without the sorbed CO_2 in the amorphous phases with the two initial degrees of crystallinity (at the top, $\chi_{init} = 70\%$, at the bottom $\chi_{init} = 50\%$).*

computing the diffusion coefficient.

5.4.1.2 Einstein relation

In an isotropic system, the self-diffusion coefficient, denoted as D, can be determined through the displacement autocorrelation, which involves considering the mean squared displacement in all isotropic directions. This relationship is described by the Einstein relation:

$$msd(t) = \frac{1}{N} \sum_{i=1}^{N} |\mathbf{r_i}(t) - \mathbf{r_i}(0)|^2 \tag{5.16}$$

$$D = \frac{1}{d} \lim_{t \to \infty} \frac{d}{dt} msd(t) \tag{5.17}$$

where d is the number of isotropic directed dimensions of space (6 for 3 dimensions), $\frac{d}{dt}$ the time derivative. N the number of tracked molecules.
To compute D, molecular dynamics simulations are performed in the NVE ensemble. During the simulation, the positions of the gas penetrants are recorded. To enhance the sampling, a block method is employed. The time block has a size much smaller than the entire run but is large enough for the diffusive mode to be reached (where a linear relationship is achieved between the *msd* and time). An average of the *msd* is calculated over all the available data (the entire run) in the dataset over the time block. This significantly improves the quality of the statistics.

5.4.1.3 Anisotropy of the semicrystalline structure

The semicrystalline polymers exhibit strong anisotropy. In the amorphous phase, concerning the gas penetrants, the x and y directions, which are perpendicular to the long-period

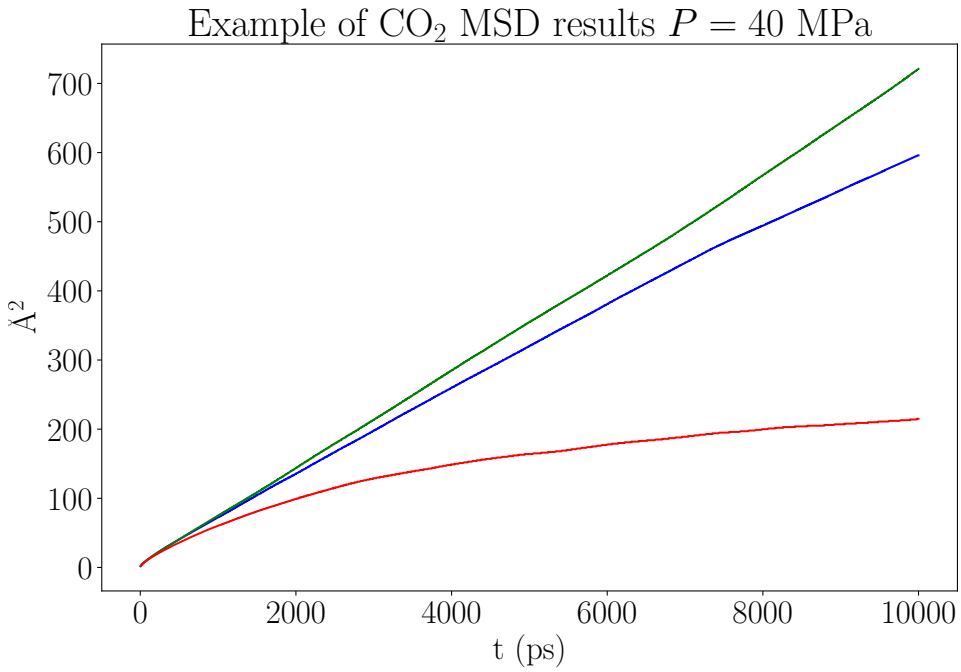

Figure 5.13: *The MSD is depicted in three spatial directions, calculated using the block method. The top green line corresponds to the x direction, the blue line represents the MSD for the y direction. The bottom red line corresponds to the MSD in the z direction.*

direction, can be considered equivalent. For instance, in Figure 5.13, the mean squared displacement (MSD) of CO_2 sorbed in the semicrystalline structure at 40 MPa is computed in each spatial direction. As shown, the MSD slopes in the x and y directions are nearly identical, while the MSD in the z direction tends to converge towards a finite value related to the inter-crystalline distance's size. Only the x and y isotropic directions are considered in the study for the computation of the total coefficient of diffusion D.

5.4.1.4 Thermodynamic factor correction

As explained in Section 2.4.2.1, self-diffusion is calculated from the Mean Squared Displacement (MSD). However, it is equal to the Maxwell-Stefan diffusion coefficient since the velocity of the chains is negligible compared to the velocity of the small gases. To obtain the Fickian diffusion coefficient, which is the one which interests us, it is necessary to multiply the Maxwell-Stefan coefficient by the thermodynamic factor $Q = \frac{\partial \ln(f/P_0)}{\partial \ln(C_a)}$.

$\ln(f/P_0)$ is plotted as a function of $\ln(C_a)$ in Figures 5.14 and 5.15. Up to 30 MPa, the logarithm of the fugacity is well approximated with linear fits. The slope were used as the thermodynamic factor to correct the computed diffusion to obtain the Fickian diffusion coefficient.

5.4.1.5 Diffusion results

The significant challenge when comparing diffusion results in our system with experimental data lies in the complex path that a gas particle follows within the semicrystalline struc-

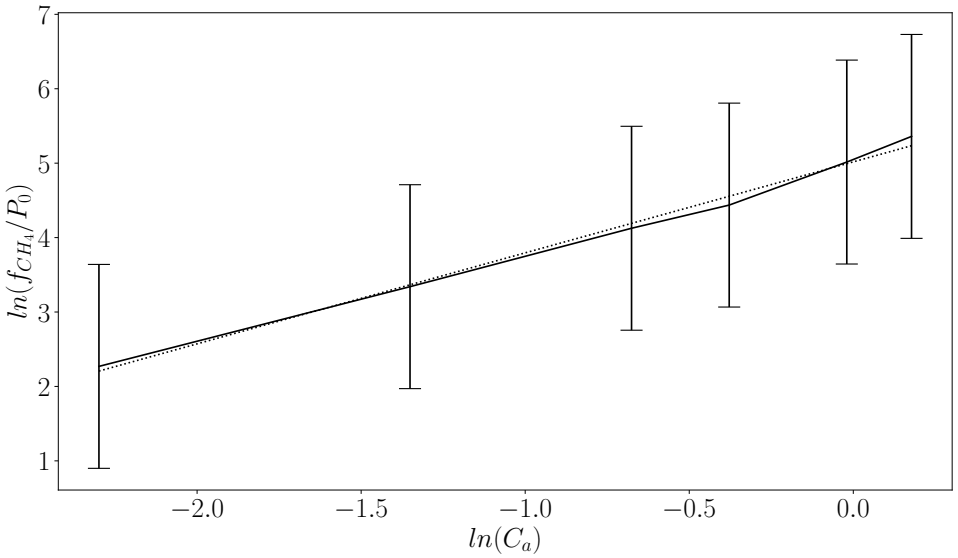

Figure 5.14: *The logarithm of the CH_4 fugacity is plotted as the function of the logarithm of the concentration in the amorphous phase. The dotted line is a linear fit, the slope is the thermodynamic factor* 1.2227*. The points correspond to* $1, 3, 7, 10, 20, 30$ *MPa.*

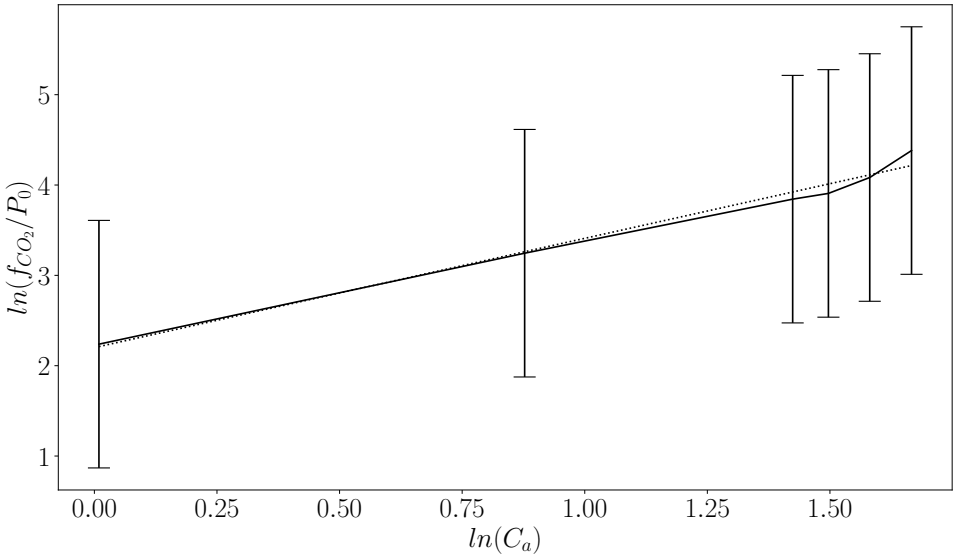

Figure 5.15: *The logarithm of the CO_2 fugacity is plotted as the function of the logarithm of the concentration in the amorphous phase. The dotted line is a linear fit, the slope is the thermodynamic factor* 1.2096*. The points correspond to* $1, 3, 7, 10, 20, 30$ *MPa.*

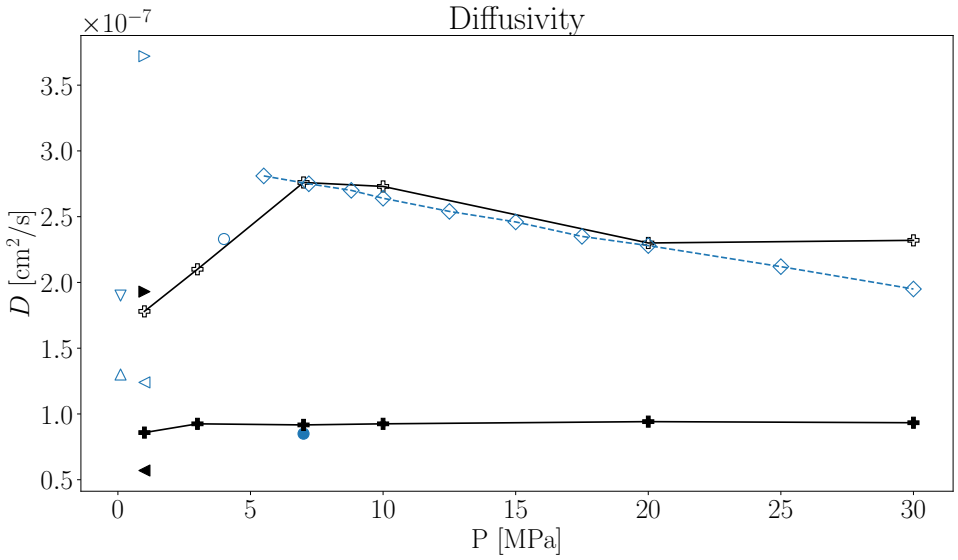

Figure 5.16: *Diffusion of CO_2 and CH_4 with pressure of particle reservoir. The average across the used structures of the amorphous fraction is $\overline{\phi}_a = 40$ %. The hollow markers label CO_2, the solid markers label the CH_4 for all the results. The two solid black lines (CO_2 at the top, CH_4 at the bottom), are the results of our computation corrected with the tortuosity τ such that it matches the results of Flaconnèche et al. [Flaconneche et al., 2001] : the hollow circle for CO_2 and the solid black circle for CH_4, Flaconnèche et al. results were extrapolated from 313.15 K to 300 K with the Arrhenius law presented in their article, $\phi_a = 37$ %. The triangles pointing at the right are the results of Michaels and Bixler [Michaels and Bixler, 1961b] with $\phi_a = 57$ %. The triangles pointing on the left are Michaels and Bixler results with $\phi_a = 23$ % ($T = 298$ K). Pino et al. results ($T = 295 - 298$ K)[Pino et al., 2005] for CO_2 are shown with a triangle pointing down for $\phi_a = 43$ %, pointing up for $\phi_a = 37$ %. The results of Hu[Hu, 2021] for CO_2 are represented with the dashed line ($\phi_a = 40$ %).*

ture. Spherulites form intricate mazes, with the crystalline lamellae serving as their walls. Furthermore, these lamellae are branched, leading to bifurcations, and the connections between spherulites themselves remain poorly understood.

In recent years, authors modeling the diffusivity of particles in semicrystalline polymers, such as Memari et al. [Memari et al., 2015], have primarily focused on modeling pure amorphous polymers. Several methods have been utilized to bridge the gap between values in pure amorphous polymers and those in semicrystalline polymers.

One approach involves extrapolating diffusion coefficients obtained from the melt to the amorphous phase of the semicrystalline polymer using the Arrhenius law. However, this method relies on strong assumptions, such as a constant activation energy over the temperature range, and it does not account for the reduced mobility of chains in the amorphous fraction of the semicrystalline structure. Another method assumes a homogeneous dispersion of crystalline lamellae [Krishna Pant and Boyd, 1993] to provide a lower bound for the diffusion results in the amorphous phase of the semicrystalline structure.

An alternative method involves comparing the amorphous phase of the semicrystalline polymer to an equivalent pure amorphous polymer, like natural rubber [Michaels and Bixler, 1961a]. Michaels assumes that natural rubber and the amorphous part of the semicrystalline polyethylene structure have equivalent properties. However, the diffusivity in rubber needs correction, which takes into account the higher immobilization of chains in the amor-

phous part of the semicrystalline structure and a geometric factor, known as the tortuosity coefficient. This coefficient considers that the crystalline phase is impermeable, and the path of the sorbed molecules must follow the continuous amorphous region (see Section 2.4.2.2).

The efforts, we employed to model explicit semicrystalline structure were partly dedicated to overcome this situation. It is possible to apply Michaels theory, but only the correction with the geometric factor is needed.

$$D = \frac{D_{sc}}{\tau} \tag{5.18}$$

where D_{sc} is the fickian diffusion coefficient in the semicrystalline model. Our results are presented in Figure 5.16. The calculations were conducted on four different structures for both gases and pressures, and the results were averaged. The average volumic amorphous fraction in our structures is 40%. We calibrated the parameter τ using Flaconnèche's results, which led to a value of $\tau = 8.5$. This value is higher than the τ values provided in Figure 2.17 by Michaels, which is approximately 3.2, considering the average amorphous fraction of the selected structures. Flaconnèche's structures have an amorphous fraction of $\phi_a = 37$ %, which is close to that of our simulated structures. Michaels' results and Pino's results, with amorphous fractions both above and below that of our simulated structures, closely align with our findings. Hu's results show excellent agreement with the computed results at higher pressures.

- How can we explain the higher value for the tortuosity?
  - The Trappe-UA forcefield is known for overestimating diffusion coefficients in alkanes. Diffusion computations for CO_2 in alkanes performed by Moultos et al. [Moultos et al., 2016] significantly overestimate the experimental results, up to 50%. Moultos et al. explain this by pointing out that the united-atom forcefield, without the hydrogens, inhibits the mobility of sorbed molecules less.
  - It is possible that Michaels' theory may require some refinement. While it considers the amorphous fraction, it does not account for other factors such as the intercrystalline distance and the spherulite connections.

One promising aspect is that tortuosity is not species-dependent. This implies that by calibrating the tortuosity using experimental data for one species, it may be possible to predict diffusion for other species. For engineers seeking to forecast transport coefficients for a broad spectrum of species, it might require just one set of experimental data to calibrate the tortuosity, enabling predictions of diffusion coefficients for all species.

The reason for choosing TraPPE-UA over a forcefield better suited for diffusion computations lies in the nature of our diffusion study, which involves a complex construction process and extended relaxation. The use of a united-atom forcefield, including hydrogen in the carbon atoms, facilitated a faster process. Our study encompasses investigations into mechanical properties, sorption, and diffusion, demanding a forcefield calibrated to address all these aspects, which is a challenging task.

To assess the impact of the forcefield and validate or challenge Michaels' proposed tortuosities, it is advisable to replicate the same study using a forcefield known to accurately replicate diffusion coefficients in pure amorphous n-alkane systems at high pressure. This approach ensures the forcefield correctly describes constrained chains within the amorphous fraction of the semicrystalline structure. Such an approach would allow the compilation of tortuosities for different polymers, degrees of crystallinity, intercrystalline distances,

and would provide valuable insights for theoreticians addressing the question of tortuosity analytically.

In Section 2.4.2.3, we presented Naito's phenomenological theory, which predicts diffusivity results based on the competing effects of concentration at low pressure. This concentration plasticizes the system, enhancing the mobility of the chains, and subsequently, the mobility of gas penetrants. Conversely, hydrostatic pressure immobilizes the system at high pressure, and our results illustrate this effect. This is illustrated by the shape of the CO_2 diffusion coefficient curve.

Another significant point is the correlation between the diffusion of CO_2 and swelling. The peak in the CO_2 diffusion coefficient, occurring at around 10 MPa, is associated with the maximum swelling (see Figure 5.12).

5.5 Exploration of the coupling between the transport properties and the mechanical properties

This section remains primarily exploratory in nature. We have endeavored to establish a connection between our studies of mechanical and sorption properties. In this section, we present various results, including sorption in a highly deformed structure, insights into the plasticizing effect of CO_2 with computations of glass transition temperature (T_g) with and without CO_2 sorbed in the system, and the effects of high deformations with sorbed CO_2. It's important to note that this is still an exploratory phase. In the case of sorption in the highly deformed structure, our computations are primarily focused on addressing the presence of cavities that emerge during deformation.

The significance of our T_g computations lies more in the methodology we employed, using an unconventional method to obtain higher resolution. However, it's essential to acknowledge that the presented results remain uncertain. Lastly, our highly deformed computations with sorbed CO_2 offer qualitative insights, rather than quantitative findings.

5.5.1 Sorption in the highly deformed structure

Sorption was performed in the deformed structure along the z-axis. However, it was not conducted using the full procedure involving MC-MD cycles, as stress and strain curves encompass a multitude of structures. Carrying out the full procedure for every deformed structure would prove to be prohibitively expensive. Therefore, for each deformation, the polymers are held frozen, and a simple grand canonical Monte Carlo simulation is executed. The results are displayed in Figure 5.17. This should be viewed more as a method for analyzing morphological changes during deformation, rather than a full-fledged sorption study.

As evident from the results, three distinct zones can be clearly identified. Up to approximately a strain of 0.025, there is a linear regime in the number of sorbed molecules. Subsequently, at a strain of 0.03, it appears that a cavity emerged and was rapidly filled. Between strains of 0.03 and 0.055, an evolution akin to a power law is observed. At a strain of 0.06, another break occurs, and another linear evolution emerges.

A comparison with the stress and strain curve may assist in our analysis of the results. The

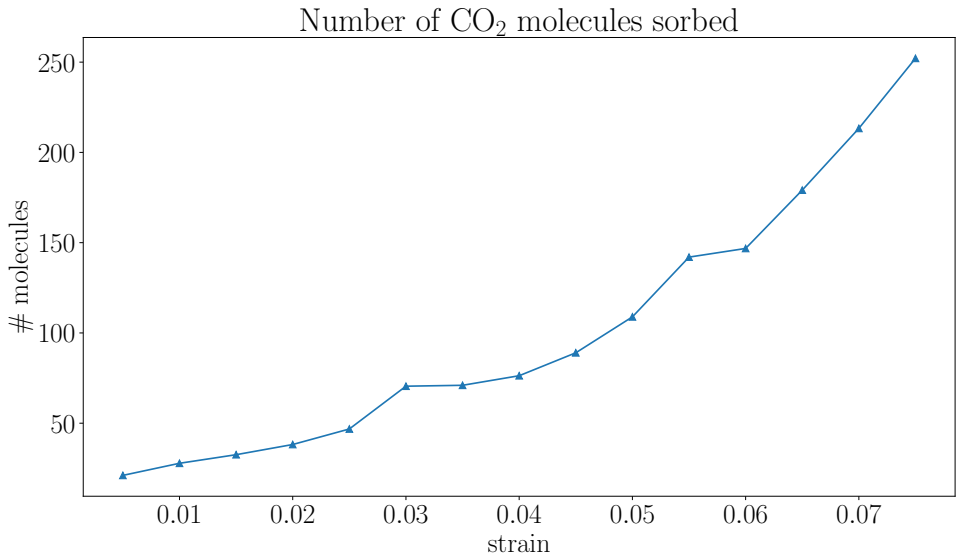

Figure 5.17: *Sorption of CO2 at* 30 *MPa on a strained structure.*

peak in the upper curve of Figure 5.20 (which pertains to the same system) aligns with the second sorption break at 0.06. This could be interpreted as the initiation of significant cavitation, similar to what is depicted in Figure 4.9 in its final form. The first break at 0.025 in the sorption vs strain curve could signify the point where the system deviates from the linear elastic regime.

5.5.2 Glass transition temperature

In this section, the glass transition temperature (T_g) for empty semicrystalline structures and structures with CO_2 sorbed at 40 MPa was computed.

5.5.2.1 Method for T_g calculation

To determine the glass transition temperatures, the structures undergo the following process: they are initially equilibrated at 350 K in the NPT ensemble; then, they are cooled down in steps of 10 K over the course of 1 ns in the NPT ensemble, with a pressure of 40 MPa (the pressure at which the CO_2 molecules were sorbed), until reaching 10 K. Subsequently, the structures are heated in a similar manner until they reach 350 K again.

The primary method for identifying the glass transition temperature (T_g) involves locating the two linear regimes in the mass density vs. temperature plot. The intersection of these two linear regimes corresponds to the T_g.

The only issue is that the T_g depends of the cooling (or heating rate), in simulation we access cooling (or heating) rate orders of magnitude larger than the ones used for experiments. Hopefully, the WLF method named after Williams-Landel-Ferry[Ferry, 1980] allows to relate the T_g at different heating (or cooling) rate.

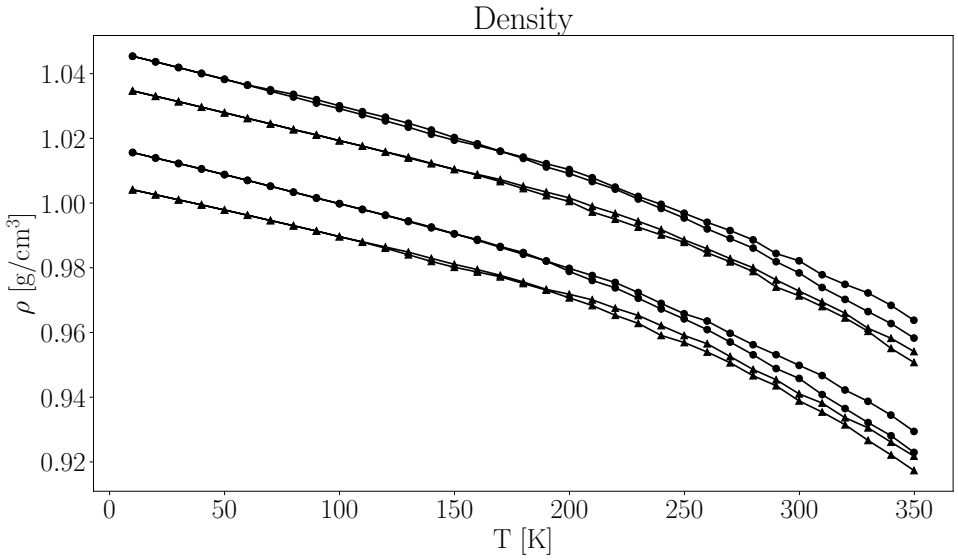

Figure 5.18: *The figure shows the evolution of the density during the cooling (and heating) in two structures with two degree of crystallinity $\phi_a = 0.49\%$ and $\phi_a = 24\%$, loaded and non-loaded with CO_2 sorbed at 40 MPa. The structures loaded with CO_2 are labeled with circles. The empty structures are labeled with triangles. The two structures with $\chi_{init} = 70\%$ are at the top, the two structures with $\chi_{init} = 50\%$ are at the bottom.*

$$T_{g(sim)} - T_{g(exp)} = \frac{-C_2 log_{10} \frac{t_{g(sim)}}{t_{g(exp)}}}{C_1 + log_{10} \frac{t_{g(sim)}}{t_{g(exp)}}} \tag{5.19}$$

where $T_{g(sim)}$ and $T_{g(exp)}$ are the simulated and experimental T_g, $t_{g(sim)}$ and $t_{g(exp)}$ are the cooling or heating rates.
C_1 and C_2 are coefficients specific at different polymers or family of polymers. Soldera et al. provide value adapted to polyethylene [Soldera and Metatla, 2006] : $C_1 = 16.7$ and $C_2 = 48$ K.

To identify the two best linear fits, sophisticated methods are employed. These methods include fitting the entire curve with a hyperbola, the asymptotes of which are linear (as described by Watts [Watts and Bacon, 1974]), or conducting an exhaustive search of all possible fits with two lines and selecting the pair that minimizes the error.

In our simulated system, the challenge is that because the model's melting temperature is very close from the glass transition temperature, as we will see, fitting a line on this side of the curve is complicated due to the lack of points.

5.5.2.2 T_g results

The density along the heating (or cooling) are plotted on Figure 5.18. Straight lines from 10 K to almost 200 K are showing a linear domain below T_g. The second domain is not clear. The heating and cooling curve are not converging, a reason is that another transition very close from the T_g is happening i.e. crystallization or melting. Ramos et al. [Ramos et al., 2015] did some T_c (temperature of crystallization) computation with TraPPE-UA semicrystalline models, they found a dependency with the width of the crystalline phase

ϕ_c	76%	51%
Without CO_2	157 K	137 K
With CO_2	127 K	127 K

Table 5.5: *Estimation of the T_g from the difference of Energy between the cooling and heating corrected with the WLF equation.*

m, considering our crystalline widths, we expect a crystalline transition around 350 K (the experimental value is closer to 400 K). This transition contaminates the changes in density we may observe due to the glassy transition.

Minisini and Soldera [Minisini and Soldera, 2023] in a recent paper proposed a way to characterize the T_g. They showed that during a transition, the total energy is found to be lower during heating than during cooling. Explaining that in a more intuitive way, we can think about what happens when we heat a glassy or a crystalline object, the object may persist a bit in its more stable configuration, hence a lower energy. When an amorphous object is cooled down, it may persist in a higher energy configuration, the time to adopt the lower energy configuration. Minisini et al. showed that the difference of energy between the heating and the cooling of the polymers was less noisy than the equivalent volumetric or density information. A narrow peak for the difference of energy is present at the transition. Narrower than the equivalent difference of density peak.

The results are shown in Figure 5.19. The results are sligthly clearer, but still uncertain. The sum of two pyramid shapes are expected for the results. A small pyramid shape, for the glassy transition temperature, a larger temperature for the melting/crystallization.

In the bottom left of the Figure 5.19, we clearly see two peaks. A first small peak for the T_g may be identified, then another transition occurs on the right.

The sum of the two pyramid shapes may also results in a plateau between the two peaks like in the upper right plot. The beginning of the plateau may be considered as the T_g.

The two other plots, the upper left and the bottom right are not clear, still we may interpret the first peak of the upper right as the T_g. The bottom right is very uncertain.

Applying the WLF correction we obtain the results in table 5.5. The experimental T_g is between -100℃ and -125℃ (173 - 148 K) [Greene, 2021] depending on the molecular weights and the degrees of crystallinity.

The results are consistent with the experimental data for the T_g. Two effects are visible, the effect of the degree of crystallinity and the plasticizing effect of CO_2. A higher degree of crystallinity involves smaller bound chain sections in the amorphous phase with less mobility so a higher T_g. A plasticizing effect due to the presence of CO_2 decrease the T_g.

The results are consistent, but the determination of the points are quite uncertain. The resolution of the curves is too low. To determinate the T_g with better accuracy, decrease the heating (and cooling) speed at least one order of magnitude is needed which is possible but computationally expensive.

5.5.2.3 High deformation with CO_2

Another approach to explore the plasticizing effect of CO_2 in polyethylene is through high deformation computations. In Figure 5.20, we present high deformation computations sim-

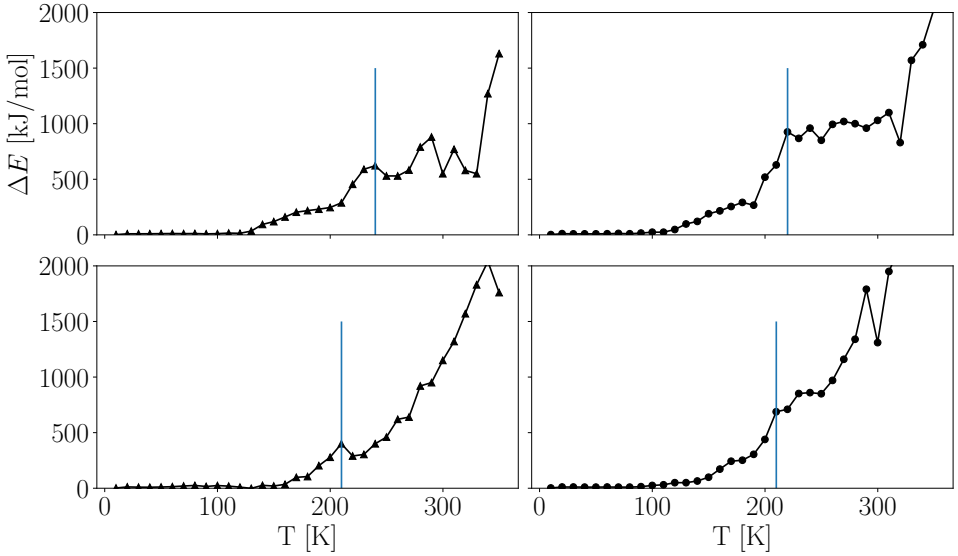

Figure 5.19: *ΔE for the 4 structures, the top row concerns the structures without sorbed species, the bottom row concern the structure with sorbed CO_2 at 40 MPa. The left column is the structure with $\phi_a = 24$ %, the right column is the structure with $\phi_a = 0.49$ %. The blue lines are trials at localization of the T_g before the WLF correction.*

ilar to those conducted in Section 4.3, but this time applied to a single structure with and without CO_2 dissolved at 30 MPa.

As we can see, the sorbed CO_2 plasticizes the structure. The elastic domain of the structure with sorbed CO_2 has a slope slightly lower than the one without CO_2. The peak is also slightly below the peak of the empty structure. Interestingly, the plateau is exactly the same.

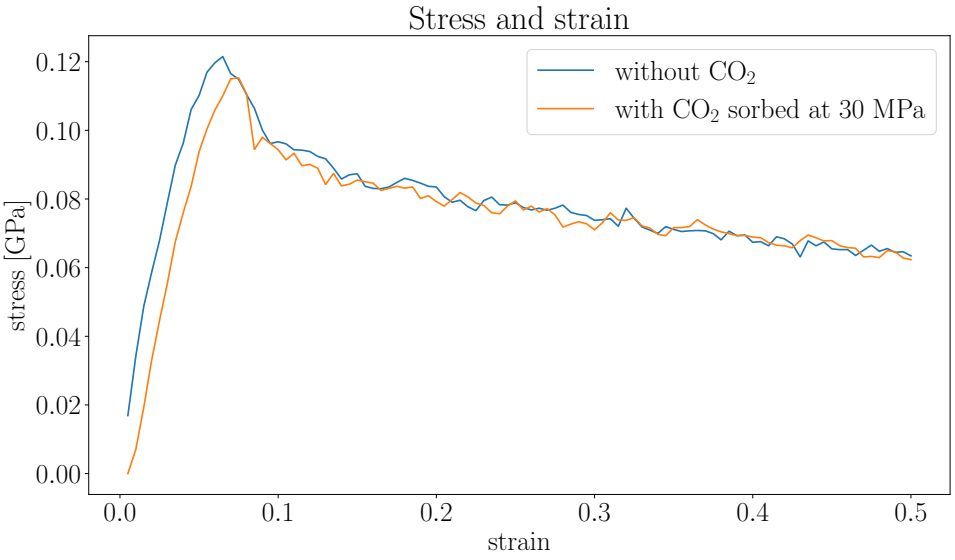

Figure 5.20: *Comparison between the same structure strained with or without CO_2 sorbed at 30 MPa.*

Chapter 6

Conclusion

6.1 Regarding semicrystalline polymer model building

6.1.1 Generation of semicrystalline structure with Adhikari's statistics

The method used in this study is based on a polymer statistical physics theory proposed by Adhikari and Muthukumar [Adhikari and Muthukumar, 2019]. This statistical theory provides insights into the fraction of different amorphous chain types (tie chain, loop, tail) in the amorphous phase and the distribution of their lengths considering freely jointed chains.

It is important to note that freely jointed chains are an idealization of real polymer chain, which can be seen as a limitation. However, by bridging the gap between idealized and real chains, control over the fraction of tie chains which aligns with one of the study's objectives, was gained, allowing the investigation of the relationship between mechanical properties and the tie chain fraction.

The conversion from the ideal chain to the real chain relies on an input parameter, the characteristic ratio (C_∞). This parameter controls the stiffness of the ideal chain; a higher characteristic ratio results in longer chains emerging from the crystalline phase, persisting in the same direction, and increasing the probability of forming tie chains bridging two crystallites.

Additionally, other factors such as the degree of crystallinity, the long period, and molecular weight were well-controlled in the study.

With this foundation in place, the method could evolve in two different directions.

6.1.2 Simplification of the method

Instead of relying on complex non-analytical probability distributions of chain section lengths in the amorphous phase, it is possible to use a simpler probability distribution.

In terms of mechanical properties, under the elastic limit, the tie chain fraction does not

seem to have a significant impact. Similarly, for sorption and diffusion properties, there is no substantial influence of the tie chain fraction on sorption properties. However, further investigation is required to fully characterize the effect of *elastically active chains*, as proposed by Memari et al. [Memari et al., 2015], which likely include the tightest *bridging entanglements* and *tie chains*.

Beyond the debate surrounding the quantity of adjacent reentries, there seems to be a consensus in theoretical treatment, modeling methods, and experimental measurements that smaller amorphous chain sections are more prevalent than larger ones. When initiating the construction process with two crystalline phases surrounding a void, any monotonically decreasing probability function for amorphous chain section lengths may be employed to fill the amorphous phase.

If a convex probability distribution function for amorphous chain section lengths is chosen, the resulting models will more closely resemble what is commonly known as the *adjacent reentries model*. Conversely, if a concave probability distribution function for length is chosen, the constructed models will align more closely with what is referred to as the *switchboard model*. It's important to note that the selected probability distribution must undergo renormalization to ensure proper filling of the entire amorphous phase. A similar renormalization was also performed with Adhikari statistics. Subsequently, an amorphous phase is generated using the drawn polymer chains.

The most important requirement is that the chosen probability distribution enables the connection of the amorphous chain sections to the crystallite edges through the connection algorithm. The final lengthy relaxation process facilitates the sliding of the chains and their readjustment.

In the procedure described in Chapter 3, the edges of the amorphous chain sections were labeled to identify the connection sites for the connection algorithm. In this simplified method, these labels (e.g., label A to connect with crystalline edge A, label B to connect with crystalline edge B) are assigned randomly. However, there is a constraint in place: chain sections smaller than the imposed intercrystalline distance must share the same label to be connected to the same crystalline edge. This constraint is necessary because chain sections smaller than the intercrystalline distance cannot form ties with separate crystalline edges.

Random labeling is a crucial aspect of the process as it ensures a high level of entanglements. This high density of entanglements is vital because it guarantees that the final degree of crystallinity remains close to the intended value. In our trials, too few entanglements lead to recrystallization when performing a final relaxation. Randomly selecting the connection sites helps prevent recrystallization or melting, ensuring that the system does not deviate too far from the imposed initial degree of crystallinity.

Following the labeling step and the connection algorithm, the final stage involves a lengthy relaxation process until all the thermodynamic quantities converge.

In Figures 6.1, 6.2, and 6.3, examples of other polymers constructed using a simplified method are presented: Polyethylene glycol (PEG), Polyether ether ketone (PEEK), and Polytetrafluoroethylene (PTFE), also known as Teflon. These models can be adjusted to match the experimental molecular weights, degrees of crystallinity, and long periods. Moreover, these models can be utilized to compute various properties, including mechanical and sorption properties, as well as other properties like electronic properties. Band gap computations were performed in model of semicrystalline polyethylene by Moyassari et al. [Moyassari et al., 2017] with density functionnal theory.

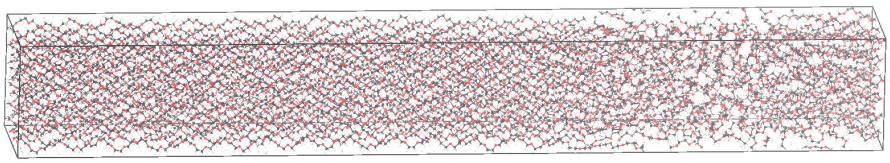

Figure 6.1: *Model of Polyethylene glycol (PEG) with a simplified building method.*

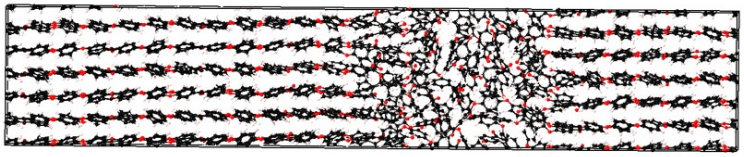

Figure 6.2: *Model of Polyether ether ketone (PEEK) with a simplified building method.*

Only pure linear polyethylene was modeled, but branched chains may be modeled too. The branches are necessarily excluded from the crystalline phase, because it prevents crystallization.

6.1.3 More complicated method

Instead of simplifying the method, an alternative approach could involve a more detailed development similar to what Adhikari and Muthukumar undertook, but with real polymer chains rather than ideal ones. This method would necessitate the construction of matrices that describe the probabilities of chain movement in various directions, taking into account the energies associated with torsion and bending of the polymer chain. While this approach would be considerably intricate and require meticulous mathematical treatment, it is indeed feasible. However, it would need to be repeated for each type of polymer.

Nilsson's model uses a realistic random walk of this type [Nilsson et al., 2012], however the formalism used required a correction with adjacent reentries to prevent the realistic random walk from filling the entire amorphous phase without connecting all the crystalline stems. Adhikari's formalism do not need such a correction. Integrating a realistic random walk such as the one in Nilsson's method with Adhikari's treatment to create a more comprehensive approach is a possibility.

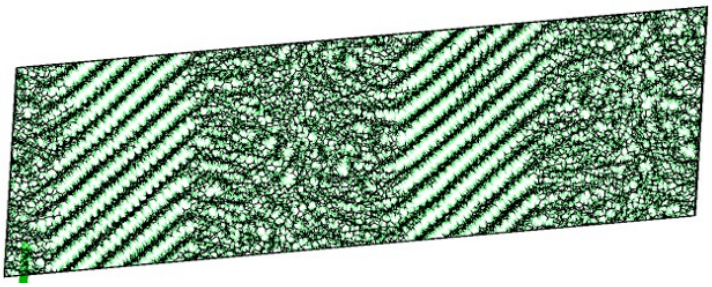

Figure 6.3: *Model of Polytetrafluoroethylene (PTFE), commercially known as Teflon, with a simplified building method.*

It is important to recognize that this more complex treatment may be of greater significance for fundamental scientific knowledge rather than providing immediate practical solutions for materials development.

6.2 Regarding the mechanical properties

6.2.1 Elastic constants

In our study of elasticity, we exclusively computed the uniaxial elastic coefficients, specifically the first three c_{ii} values of the elastic matrix, with success. This limitation arises from the complexity of effectively relaxing the shear directions, which poses challenges both when relaxing the unstrained structure and when dealing with strained structures. The difficulty to determine the shear coefficients has, in turn, prevented us from calculating macroscopic moduli, such as the Young modulus and the shear modulus. To potentially address this limitation, it may be necessary to conduct longer relaxation simulations with larger structures. Advances in computational power may soon enable the determination of shear non-diagonal coefficients more easily.

However, the results on the elastic coefficients gave consistent results such as their increase with the degree of crystallinity.

Furthermore, another critical step must be taken: the development of mesoscopic spherulitic models into which we can incorporate our atomistic results. Examples of mesoscopic models can be found in the following references [Oktay and Gürses, 2015, Roguet et al., 2019]. Multiscale modeling is important to reproduce all the mechanical properties of semicrystalline polymer.

6.2.2 High deformation

Through high deformation along the direction of the long period, we were able to discern the primary stress transmitters, specifically, whether the bridging entanglements or the tie chains connecting two separate crystalline phases were more influential in rigidifying the polymer structures. Our observations indicated that tie chains played the most significant role, while the bridging entanglements assumed a secondary importance.

Exploring high deformation along other axes, as well as shear deformation, would also be of interest. In real materials subjected to significant stretching, these various types of deformation may occur in different locations.

Additionally, in our simulations, we maintained a constant cross-sectional area. It might be worthwhile to consider the same deformation under lateral atmospheric pressure conditions.

6.3 Regarding the transport properties

6.3.1 Sorption

The method achieved relative success, with the sorption results displaying a good agreement with experimental data. However, at higher pressures, our results exhibited slight deviations from the available experimental data. It is essential to note that, for practical reasons, a combination of molecular dynamics run and Monte Carlo run iterated in cycles was employed.

While this approach has its advantages, a more optimal coupling between the sorbed molecules and the chain mobility could be achieved by utilizing a pure Monte Carlo approach within the osmotic ensemble (μPT) and a direct integration of molecular dynamics steps into the Monte Carlo algorithm.

It is worth mentioning that dealing with long densely packed chains can be challenging when using standard Monte Carlo steps. These approaches, which involve molecular dynamics steps in the Monte Carlo run, are now directly integrated into the Gibbs code and will soon be implemented into the MedeA Gibbs engine.

Concerning the relationship with the morphology, it was shown that the solubility coefficients linearly increase with the amorphous fraction. It was not possible to discern sorption changes with the distribution of types of chains (tie, loop, tail).

6.3.2 Diffusion

The diffusion results can also be regarded as relatively successful. However, it is essential to note that these results necessitate an adjustment using a tortuosity factor because only a few long periods may be modeled at the molecular scale.

This factor takes into consideration the impermeability of the crystalline phase to the sorbed gases and the intricate path that gases follow within the spherulite structure. The results required a more substantial correction using this geometric factor compared to the one proposed by Michaels. It is well-established from other studies that the united-atom forcefield employed in this research significantly overestimates the diffusivity of the sorbed species.

By using a forcefield better calibrated for diffusion computations, it would be straightforward to validate (or falsify) Michaels' theory of tortuosity. Nevertheless, the calibrated tortuosity factor, accounting for the spherulite geometry and correcting the diffusivity overestimation due to the united-atom forcefield, is species-independent. This suggests that a researcher aiming to compute various diffusion coefficients only needs one set of experimental data for one gas to fit the tortuosity factor.

6.3.3 Permeation

As a result, it became possible to determine the gas loading and diffusivity for various pressures (with the need for calibration for one gas species). Consequently, the permeation coefficient can be fully determined. With the semicrystalline model at the molecular scale, the transport properties are entirely predictable.

6.4 Plasticizing effect

The T_g computations provided consistent predictions and clearly revealed the plasticizing effect of CO_2. They also highlighted that a lower degree of crystallinity decreases the T_g because it enhances the mobility of the bound amorphous chains.

One challenge to address is the proximity of the crystallization/melting temperature. By examining the difference in energy between cooling and heating, it became possible to discern the T_g more effectively, although there was still some uncertainty. A more precise resolution and a better separation of the two temperature transitions could be achieved by reducing the heating and cooling rates and utilizing a model with a wider crystalline width. Indeed, other studies have demonstrated that increasing the width of the crystalline lamellae leads to higher melting or crystallization temperature.

6.5 General conclusion

The thesis project has resulted in the development of a model-building procedure that allows precise control over various aspects of semicrystalline morphology, including the degree of crystallinity, molecular weight, types of amorphous chain sections, and the long period in HDPE. This procedure can also be extended to model other semicrystalline polymers.

With this model construction procedure, it becomes possible to predict properties related to both mechanical and transport characteristics. Furthermore, various other properties can be predicted using different theoretical approaches with similar semicrystalline models.

The development of an integrated semicrystalline model construction module could provide access to a wide range of properties, including electronic properties and those associated with molecular arrangement. To access properties that depend on mesoscopic spherulitic structures, employing phase field modeling of the spherulite and incorporating results obtained at the molecular scale may become necessary. The ability to predict most of the relevant properties of semicrystalline polymers through simulation is well within reach.

Chapter 7

Résumé en français

Cette étude a été menée dans le cadre d'une thèse financée par Materials Design S.A.R.L., l'Association Nationale de la Recherche et de la Technologie (ANRT) et l'IFP Énergies Nouvelles, en collaboration avec le CNRS. L'objectif scientifique de cette étude est d'explorer l'influence de la morphologie des polymères semicristallins sur leurs propriétés mécaniques et de perméation à travers des simulations à l'échelle moléculaire. Sur le plan industriel, l'objectif est de développer une méthodologie pour la création de modèles de polymères semicristallins destinés à la simulation, ainsi que pour le calcul des propriétés mécaniques et barrière.

Contexte scientifique et industrielle

La morphologie des polymères semicristallins demeure encore mal comprise. À l'échelle microscopique, nous observons la présence de structures sphérulitiques de quelques centaines de micromètres, qui pavent l'espace. Ces sphérulites sont constituées de lamelles cristallines qui émergent radialement à partir d'un centre de nucléation, formant des embranchements et séparées par des zones amorphes, comme illustré dans le schéma à gauche de la figure 7.1.

À l'échelle des lamelles, elles se présentent de manière parallèle (au centre du schéma 7.1). La périodicité est appelée la longue période, notée L_P, et son ordre de grandeur est la centaine d'Angströms.

En mesurant la masse volumique, ou en utilisant d'autres méthodes telles que la diffraction de poudre par rayons X, il est possible de déterminer le degré massique de cristallinité (χ_c), qui représente le rapport de la masse de cristal sur la masse totale.

Il est expérimentalement établi que, du point de vue des propriétés mécaniques, un accroissement de la cristallinité rigidifie le polymère. En ce qui concerne la sorption de gaz dans le polymère, seules les zones amorphes sont perméables. Plus la cristallinité augmente, moins les molécules de gaz peuvent se dissoudre dans la matrice de polymère. Cette relation est même linéaire, comme indiqué par Michaels : $C = \phi_a C_a$, où la concentration de gaz dans le polymère C est proportionnelle à la concentration dans la zone amorphe C_a, le facteur de proportionnalité étant la fraction volumique amorphe ϕ_a.

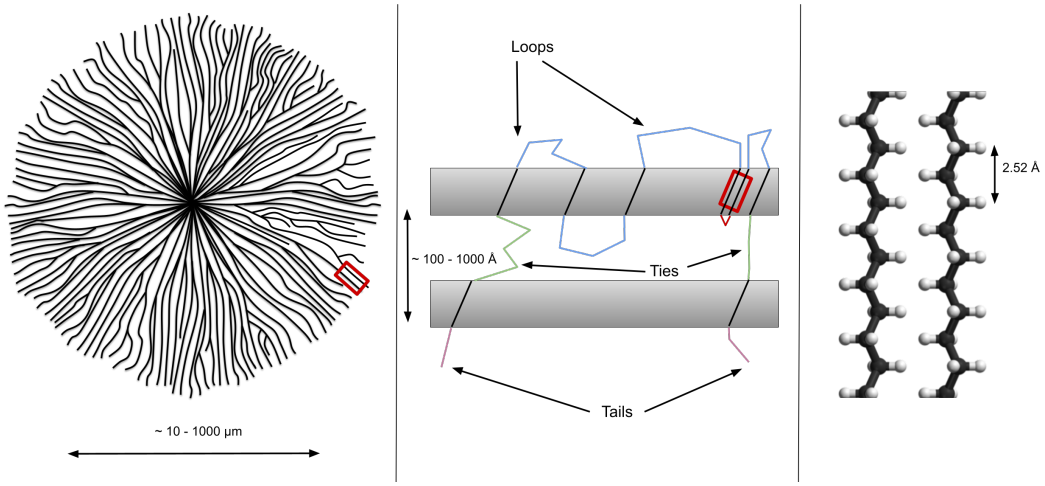

Figure 7.1: *Réprésentation schématique multi-échelle d'un polymère semi-cristallin. À gauche : une sphérulite composée de lamelles cristallines émanant d'un centre de nucléation dans toutes les directions. Ces lamelles sont constituées de polymères alignés formant une région cristalline. Au milieu : une seule chaîne polymère traverse deux lamelles cristallines en gris. Les sections de chaînes dans les régions amorphes se déclinent en trois types : des chaînes réentrantes en bleu, où le polymère réintègre la même lamelle ; des chaînes pontantes en vert, où le polymère relie deux lamelles ; et des bouts de chaîne en violet, où le polymère termine son chemin dans la phase désordonnée. La marche rouge est appelée une réentrée adjacente. Il s'agit de la réentrée la plus petite possible. À droite : une représentation de deux chaînes cristallines de polyéthylène. Les rectangles rouges montrent l'agrandissement successif de gauche à droite.*

D'autres paramètres morphologiques sont pris en compte dans notre étude.

La zone amorphe est, par définition, désordonnée, mais elle peut néanmoins être caractérisée. Cela est illustré dans le schéma central de la figure 7.1, où certaines sections de chaînes amorphes relient deux lamelles cristallines et sont appelées *chaînes pontantes* (ties en anglais), tandis que d'autres retournent dans la même lamelle dont elles ont émergées et sont appelées *chaînes réentrantes* (loops). Les chaînes pontantes sont soupçonnées d'être des *transmetteurs de contrainte* lors de la déformation mécanique.

Un autre paramètre morphologique lié à la zone amorphe concerne la quantité d'enchevêtrements piégés. Les enchevêtrements qui relient deux sections amorphes émergeant de deux lamelles différentes sont également suspectés d'être des transmetteurs de contraintes.

En ce qui concerne la sorption, les *chaînes élastiquement actives*, constituées de chaînes pontantes courtes, c'est-à-dire tendues (d'où le terme *élastiquement actives*), et les chaînes enchevêtrées liant deux lamelles tendues également, limitent le gonflement du polymère immergé dans un bain de gaz et, par conséquent, limitent la sorption.

L'objectif de l'étude est de générer des structures qui contrôlent ou mesurent les paramètres morphologiques susmentionnés, dans le but de préciser leur impact sur les propriétés mécaniques et de perméation.

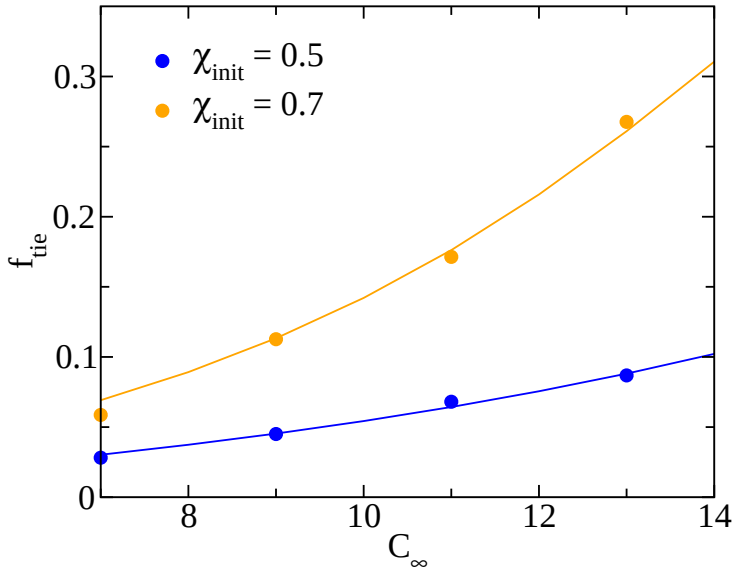

Figure 7.2: *Fraction de chaînes pontantes, f_{tie}, en fonction du C_∞, obtenue par la théorie de Adhikari et Muthukumar (lignes) et celles des modèles construites (points) pour deux degrés de cristallinité étudiés.*

Une proposition originale de création d'échantillons semi-cristallin pour la simulation à l'échelle moléculaire

Une part significative de cette recherche concerne le développement d'une nouvelle méthode de construction de modèles de polymères semicristallins pour la simulation moléculaire (dynamique moléculaire et Monte Carlo). Cette méthode permet de construire des modèles en contrôlant divers paramètres morphologiques tels que la cristallinité, la longue période et la fraction de types de chaînes (réentrantes, pontantes). Cependant, la dernière de ces données, à savoir la fraction de chaînes de chaque type et la distribution de longueur de chaîne, ne fait pas consensus dans la littérature expérimentale.

Une théorie de physique statistique proposée par Adhikari et Muthukumar (2019) nous fournit ces informations en utilisant un traitement issu de la théorie des champs des polymères. Cette théorie statistique repose sur le modèle de chaîne idéale librement jointe (*freely jointed chain*). Elle fournit les fractions de différents types de chaînes et les distributions de longueur. Pour effectuer la conversion entre une chaîne idéale et une chaîne réelle, un paramètre d'entrée crucial est le C_∞.

Lorsque l'on convertit une chaîne réelle en une chaîne idéale, on choisit à partir de quelle quantité de monomères la corrélation avec la direction du monomère initial est considérée comme perdue. Cela permet d'approximer ce groupe de monomères par un segment librement joint dans le squelette du polymère. Plus le C_∞ est grand, plus le nombre de monomères réels est important dans le segment librement joint, correspondant à une chaîne réelle plus rigide.

Dans cette théorie, en augmentant le C_∞, on accroît la rigidité des chaînes idéales. Une chaîne émergeant de la zone cristalline persistera plus longtemps dans une même direction, augmentant ainsi la quantité de chaînes pontantes. La théorie nous fournit les

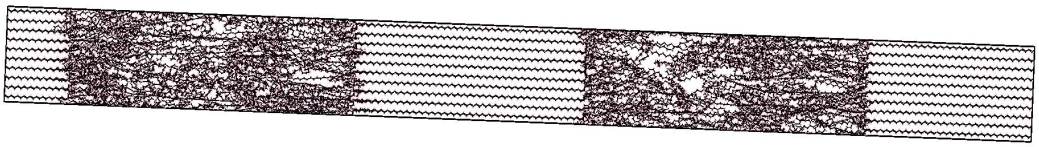

Figure 7.3: *Structure après connection avec un degré de cristallinité* $\chi = 0.5$.

fractions de chaque type de chaînes et la distribution de leur longueur.

Avec des paramètres d'entrée tels que le C_∞, la longue période, la section cristalline et le degré de cristallinité, la théorie nous donne les fractions de chaque type de chaîne (voir figure 7.2) et la distribution de leurs longueurs.

Nous pouvons générer des zones amorphes en utilisant l'*Amorphous Builder* du logiciel MedeA. De plus, en utilisant les paramètres de mailles, des zones cristallines sont générées. Ces différentes zones sont ensuite empilées. Un algorithme de connexion, initialement conçu pour créer des polymères thermodurcissables (*Thermoset Builder*), est utilisé. Cet algorithme respecte les types de chaînes grâce à un système d'étiquetage des extrémités de chaînes à connecter. Par exemple, une chaîne pontante sera reliée à deux lamelles cristallines différentes (voir figure 7.3).

Enfin, la structure est relaxée à l'aide de la dynamique moléculaire (LAMMPS), en utilisant le champ de force TRAPPE-UA, pendant 100 ns dans l'ensemble NPT.

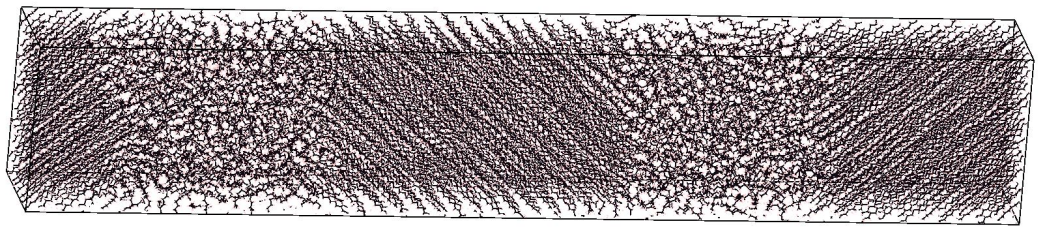

Figure 7.4: *Structure après relaxation avec un degré de cristallinité* $\chi = 0.5$.

Une fois que l'équilibrage des densités et des énergies est assuré, les structures sont prêtes pour la prédiction des propriétés.

Morphologie et propriété mécanique

Après relaxation, il est possible de recalculer, en utilisant les profils de densité (voir figure 7.5), les degrés de cristallinité (voir figure 7.6). On observe une dispersion des densités et des degrés de cristallinité, mais une bonne correspondance, en moyenne, avec les cristallinités initiales (0.5 et 0.7).

Les théories de la cristallisation, telles que celle de Flory, expliquent que ce sont les enchevêtrements qui empêchent une cristallisation complète. Bien que les conditions thermodynamiques favorisent la cristallisation, les contraintes causées par le "sac de nœuds" de la zone amorphe entravent la poursuite de la cristallisation.

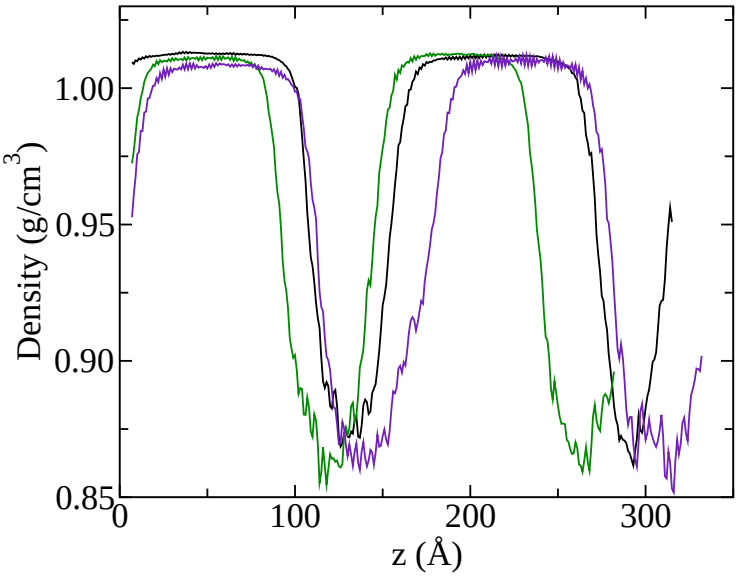

Figure 7.5: *Profile de densité le long de l'axe z, l'axe de la longue période, des trois structures avec $\chi_{init} = 0.7$ et $C_\infty = 7$.*

Nous avons mesuré la densité d'enchevêtrements dans la zone amorphe à l'aide du code Z1 de Martin Kröger. La densité d'enchevêtrement dans la zone amorphe est deux à trois fois supérieure à celle mesurée expérimentalement dans le fondu. Selon les théories de la cristallisation, presque tous les enchevêtrements du fondu se déplacent dans la zone amorphe à mesure que les cristallites se développent. Dans notre cas, en fonction de la quantité d'enchevêtrements fixée avec l'algorithme de connexion, les semi-cristallins fondent ou cristallisent jusqu'à la convergence (relative) de la densité d'enchevêtrement dans l'amorphe (voir figure 7.7).

Des calculs d'élasticité ont été effectués en accord avec les mesures expérimentales. Les coefficients élastiques uniaxiaux sont corrélés à la cristallinité (voir figure 7.8).

Au delà, de l'élasticité, les structures ont été déformées jusqu'à 50 % le long de l'axe z, celui de la longue période. On obtient des courbes de contrainte-déformation telle que celle de la figure 7.9.

Deux mesures : la contrainte maximale de la courbe σ_{US} et la contrainte moyenne entre 45% et 50% σ_{45-50}, sont choisies. Cela nous a permis de comparer nos résultats avec la morphologie.

Similairement au domaine élastique, les deux mesures augmentent avec la cristallinité (figure 7.10).

Les enchevêtrements liants et les chaînes pontantes sont suspects d'être *transmetteurs de containtes* lors de la déformation. Les σ_{US} et σ_{45-50} sont tracés sur la figure 7.11 en fonction de Les contraintes mesurées croissent avec le nombre de chaînes pontantes. De manière étrange, les contraintes diminuent avec le nombre d'enchevêtrements liants. En fait, la quantité de chaîne réentrante est anti-corrélée avec la quantité de chaînes pontantes (dû à notre méthode de construction). Le plus, il y a de chaînes pontantes, le moins il y a d'enchevêtrements liants. Ce qui nous permet de conclure, qu'en terme de transmission de contrainte, ce sont les chaînes pontantes qui sont les plus importantes.

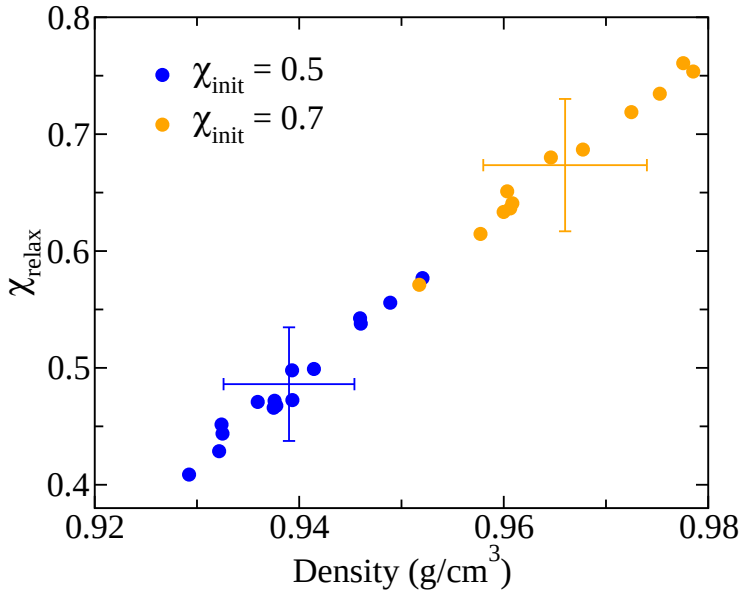

Figure 7.6: *Degrés de cristallinité en fonction de la densité pour toutes les structures étudiées. Les symboles bleus et orange correspondent respectivement aux structures avec* $\chi_{init} = 0.5$ *et* $\chi_{init} = 0.7$. *Les deux croix indiquent la cristallinité moyenne et la densité moyenne avec l'écart-type correspondant.*

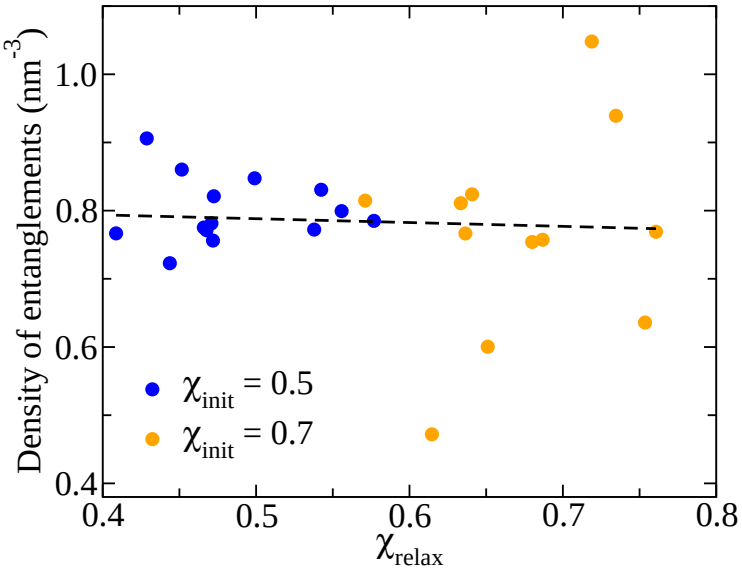

Figure 7.7: *Densité d'enchevêtrements topologiques dans les régions amorphes en fonction du degré de cristallinité* χ_{relax} *dans toutes les structures semicristallines générées.*

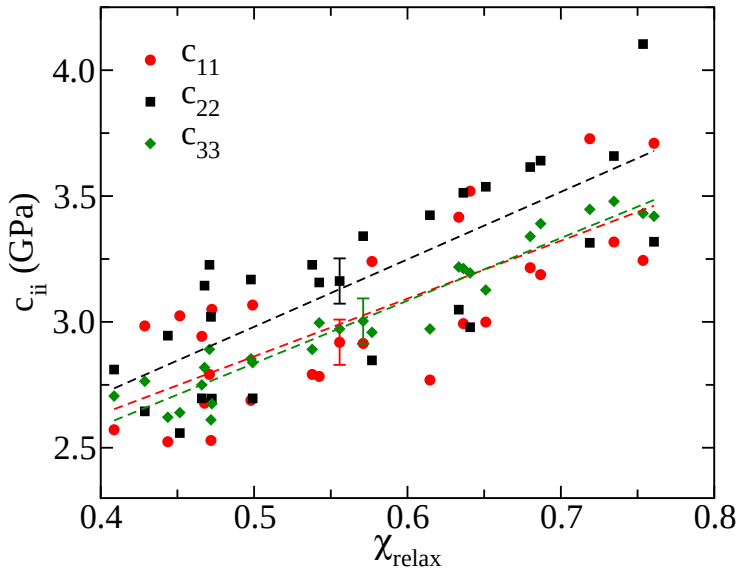

Figure 7.8: *Coefficients élastiques en traction c_{ii} en fonction du degré de cristallinité χ_{relax} de toutes les structures modélisées. Les barres d'erreur sont obtenues par propagation d'erreur à partir des erreurs de la contrainte interne calculée pour les structures déformées, et la plus grande barre d'erreur est représentée une fois pour chaque coefficient.*

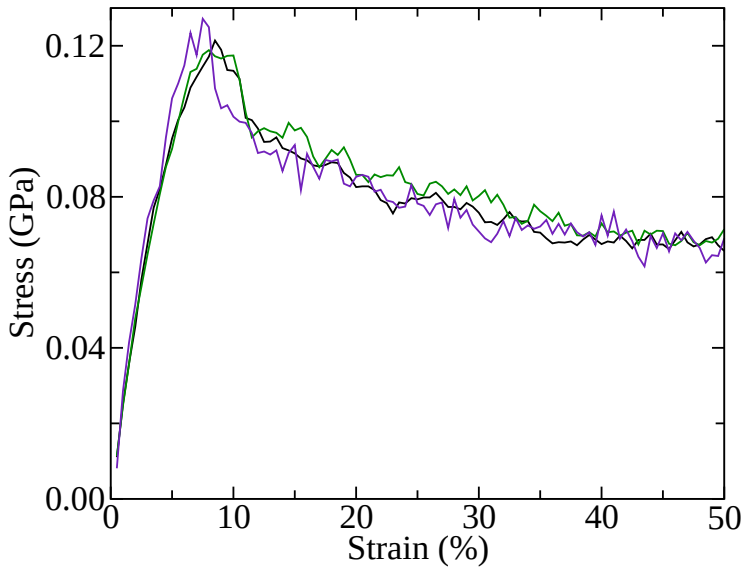

Figure 7.9: *Courbe déformation-contrainte de trois structures avec $\chi_{init} = 0.5$ et $C_\infty = 11$.*

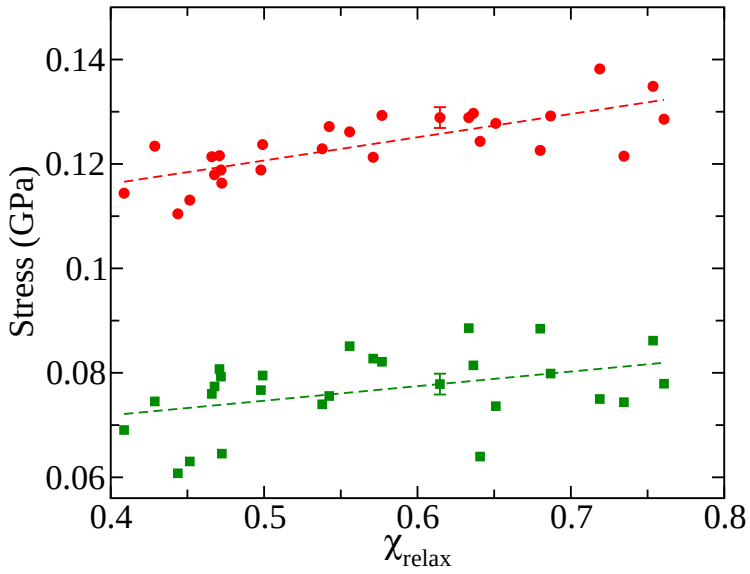

Figure 7.10: *σ_{US} (points rouges) et σ_{45-50} (carrés verts) en fonction du degré de cristallinité χ_{relax}. Les lignes en pointillés sont des régressions linéaires de chaque ensemble de données. Les barres d'erreur représentent les fluctuations des contrainte et sont fournies pour un seul point.*

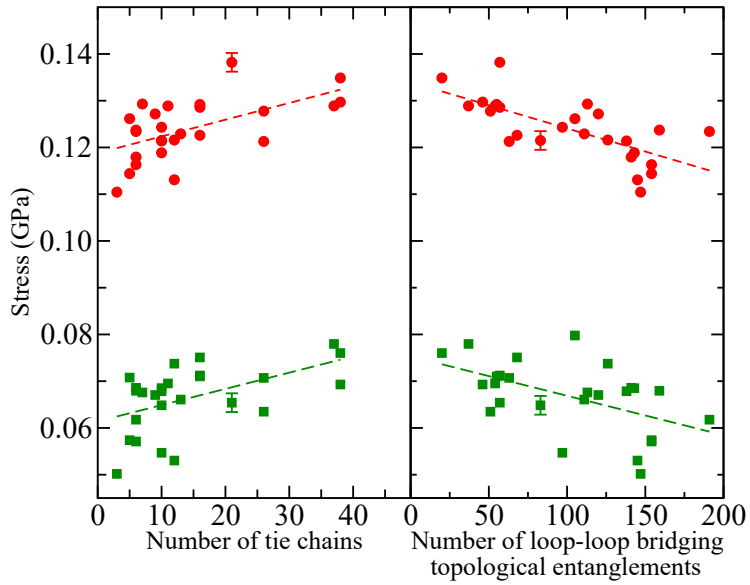

Figure 7.11: *σ_{US} (points rouges) et σ_{45-50} (carrés verts) en fonction du nombre de chaînes pontantes et des enchevêtrements topologiques de type réentrant-réentrant. Les barres d'erreur représentent les fluctuations de contrainte et sont données pour un seul point.*

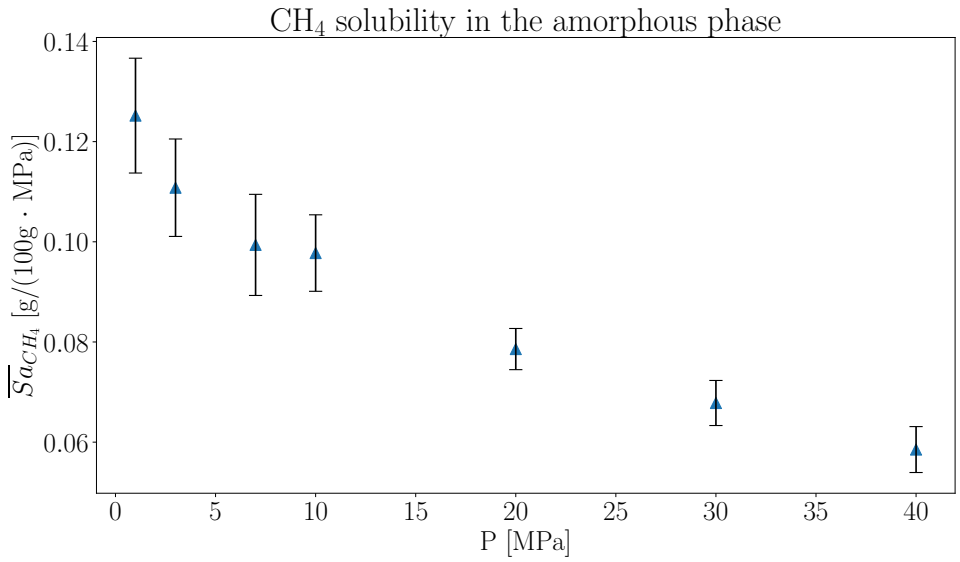

Figure 7.12: *Coefficient de solubilité moyen du CH_4 dans la fraction amorphe ($d = 0.93$ g/cm^3, marquant la frontière entre les deux phases).*

Sorption de gaz

Pour les calculs de sorption, nous avons utilisé une méthode hybride, impliquant du monte carlo dans une matrice de polymère immobile itéré avec de la dynamique moléculaire prenant en compte la mobilité des chaînes. Pour comparer les résultats avec les expériences, nous avons ramené les coefficients de solubililité à la solubilité dans la zone amorphe et nous avons consolidé les résultats sur toutes les structures (figures 7.12 et 7.13).

Les résultats s'accordent bien avec les réultats expérimentaux, on peut comparer les constantes de Henry donnés par les expérimentalistes au premier point des deux figures pour CH_4 les points expérimentaux sont entre 0.10 et 0.14 g/(100g.MPa), pour CO_2 les points expérimentaux sont entre 0.8 et 1.4 g/(100g.MPa).

Pour les calculs de diffusion à différentes pression, nous avons pris des structures avec le nombre de molécules moyen sorbés pour chaque pression. Et nous avons lancé des calculs de dynamique moléculaire, on peut utiliser l'équation d'Einstein reliant le déplacement carré moyen au coefficient de diffusion D quand la limite diffusive est atteinte. Nous avons simulé des alternances de zones amorphes et cristallines, la zone où peuvent diffuser les molécules de gaz sorbés est un plan infini amorphe dans la direction x et z, perpendiculairement à la longue période. Dans la réalité, le chemin amorphe est tortueux, il faut corriger le coefficient de diffusion calculé par un facteur de tortuosité τ qui prend en compte le fait que la zone amorphe n'est pas un plan.

$$D = \frac{D_{sc}}{\tau} \tag{7.1}$$

où D_{sc} est la diffusion dans notre modèle semicristallin, et τ la tortuosité. La figure 7.14 montre nos résultats avec une tortuosité calibrée sur les résultats de Flaconnèche.

La calibration est indépendante de l'espèce chimique et est en accord remarquable avec les valeurs expérimentales, mais le τ est plus grand que celui proposé par les travaux de Michaels. Cela peut s'expliquer par le champ de force choisi pour toute l'étude (TraPPE-

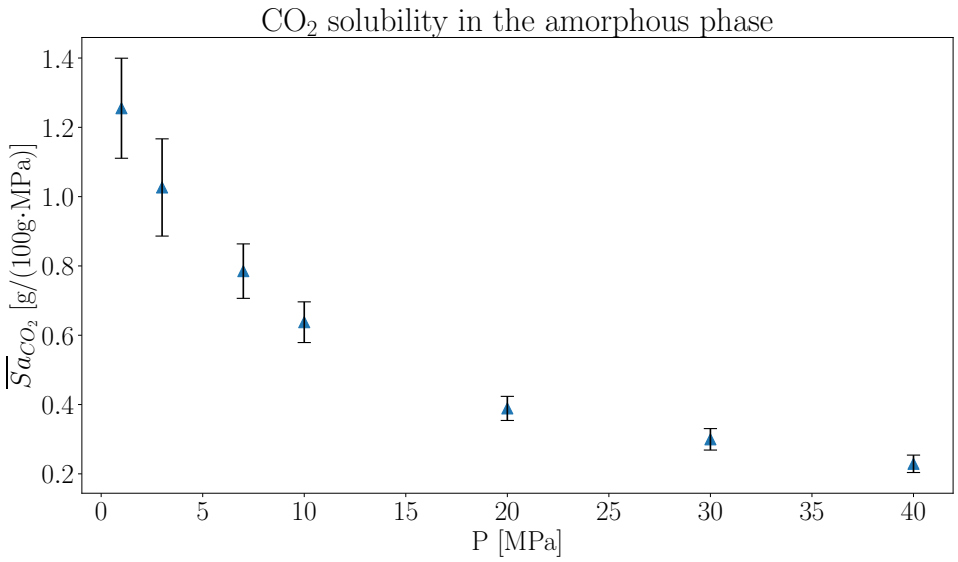

Figure 7.13: *Coefficient de solubilité moyen du CO_2 dans la fraction amorphe ($d = 0.93$ g/cm^3, marquant la frontière entre les deux phases).*

UA) qui tend à surestimer la mobilité des molécules.

Conclusion

Nous avons développé une méthodologie originale pour la création de modèles semi-cristallins destinés à la simulation. Cette approche novatrice repose sur l'utilisation d'une théorie de physique statistique des polymères. Bien que la théorie soit basée sur une chaîne idéale, cet aspect s'avère être un avantage dans notre contexte, car il nous a permis de contrôler les fractions de chaînes pontantes.
Les coefficients élastiques uniaxiaux ont été calculés avec succès et ont montré une corrélation significative avec la cristallinité. Dans le domaine des grandes déformations, l'évolution en fonction de la cristallinité demeure similaire. Nous avons mis en évidence l'influence décisive des chaînes pontantes. Il faut étendre l'étude aux coefficients non-diagonaux, mais les contraintes dans ces directions sont plus difficiles à faire converger par la dynamique moléculaire. Cela permettrait d'accéder aux modules macroscopiques.
Les sorptions sont bien prédites par le protocole itérant les simulations Monte Carlo et de dynamique moléculaire. La diffusion est bien prédite à un facteur prêt indépendemment de l'espèce chimique dissoute. Si l'on dispose d'une mesure expérimentale, on peut calibrer ce facteur prenant en compte la géométrie de la sphérulite. La perméabilité dans le semi-cristallin est donc directement prédictible par la simulation Monte Carlo et la dynamique moléculaire, ce qui est une avancée originale.
D'autres polymères ont été construits avec notre méthode de construction de modèle. Les méthodologies présentées dans ce travail pourront être utilisés à l'avenir pour prédire les propriétés mécaniques et barrière de ces autres polymères.

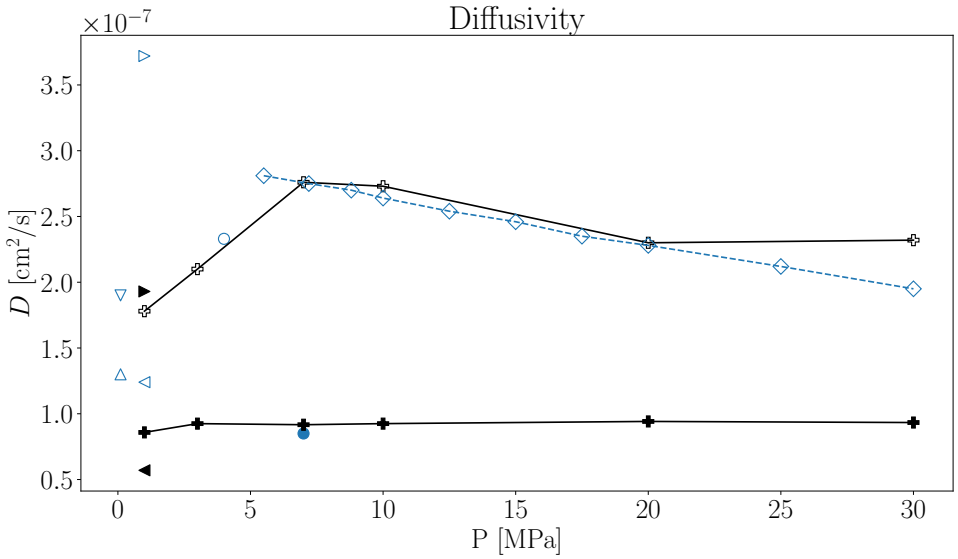

Figure 7.14: *Diffusion de CO_2 et CH_4 en fonction de la pression du réservoir de particules. La moyenne de la fraction amorphe sur les structures utilisées est $\overline{\phi}_a = 40$ %. Les marqueurs vides représentent le CO_2, tandis que les marqueurs pleins représentent le CH_4 pour tous les résultats. Les deux lignes noires pleines (CO_2 en haut, CH_4 en bas) représentent les résultats de notre calcul corrigé avec la tortuosité τ de manière à correspondre aux résultats de Flaconnèche et al. : le cercle vide pour le CO2 et le cercle noir plein pour le CH4. Les résultats de Flaconnèche et al. ont été extrapolés de $313,15$ K à 300 K avec la loi d'Arrhenius présentée dans leur article, avec $\phi_a = 37$ %. Les triangles pointant vers la droite représentent les résultats de Michaels et Bixler avec $\phi a = 57$ %. Les triangles pointant vers la gauche sont les résultats de Michaels et Bixler avec $\phi a = 23$ % ($T = 298$ K). Les résultats de Pino et al. ($T = 295 - 298$ K) pour le CO_2 sont montrés avec un triangle pointant vers le bas pour $\phi_a = 43$ %, et pointant vers le haut pour $\phi_a = 37$ %. Les résultats de Hu pour le CO_2 sont représentés par la ligne en pointillés ($\phi_a = 40$ %).*

Bibliography

[Abdou, 2015] Abdou, J. (2015). Polymer Transcrystallization Induced by Carbon Nanotube and Graphene Fibers.

[Abedini et al., 2017] Abedini, A., Crabtree, E., Bara, J. E., and Turner, C. H. (2017). Molecular Simulation of Ionic Polyimides and Composites with Ionic Liquids as Gas-Separation Membranes. *Langmuir*, 33(42):11377–11389.

[Addiego et al., 2009] Addiego, F., Dahoun, A., G'Sell, C., Hiver, J.-M., and Godard, O. (2009). Effect of microstructure on crazing onset in polyethylene under tension. *Polymer Engineering & Science*, 49(6):1198–1205.

[Adhikari and Muthukumar, 2019] Adhikari, S. and Muthukumar, M. (2019). Theory of statistics of ties, loops, and tails in semicrystalline polymers. *The Journal of Chemical Physics*, 151(11):114905.

[Alamo et al., 1992] Alamo, R. G., Chan, E. K. M., Mandelkern, L., and Voigt-Martin, I. G. (1992). Influence of molecular weight on the melting and phase structure of random copolymers of ethylene. *Macromolecules*, 25(24):6381–6394.

[Aminabhavi et al., 1988] Aminabhavi, T. M., Aithal, U. S., and Shukla, S. S. (1988). An Overview of the Theoretical Models Used to Predict Transport of Small Molecules through Polymer Membranes. *Journal of Macromolecular Science, Part C*, 28(3-4):421–474.

[Ash et al., 1970] Ash, R., Barrer, R. M., and Palmer, D. G. (1970). Solubility and transport of gases in nylon and polyethylene. *Polymer*, 11(8):421–435.

[ASTMD-638-14, 2014] ASTMD-638-14 (2014). *ASTM D638 - 14 Standard Test Method for Tensile Properties of Plastics*, volume doi:10.1520/d0638-14.

[ASTMD882-18, 2018] ASTMD882-18 (2018). *ASTM D882-18 : Standard Test Method for Tensile Properties of Thin Plastic Sheeting*, volume doi/10.1520/D0882-18.

[Balcik and Ahunbay, 2018] Balcik, M. and Ahunbay, M. G. (2018). Prediction of CO2-induced plasticization pressure in polyimides via atomistic simulations. *Journal of Membrane Science*, 547:146–155.

[Balijepalli and Rutledge, 1998] Balijepalli, S. and Rutledge, G. C. (1998). Simulation study of semi-crystalline polymer interphases. *Macromolecular Symposia*, 133(1):71–99.

[Balijepalli and Rutledge, 2000] Balijepalli, S. and Rutledge, G. C. (2000). Conformational statistics of polymer chains in the interphase of semi-crystalline polymers. *Computational and Theoretical Polymer Science*, 10(1):103–113.

[Bartczak, 2018] Bartczak, Z. (2018). Evaluation of effective density of the molecular network and concentration of the stress transmitters in amorphous layers of semicrystalline polyethylene. *Polymer Testing*, 68:261–269.

[Bassett et al., 1963a] Bassett, D. C., Frank, F. C., and Keller, A. (1963a). Some new habit features in crystals of long chain compounds part III. Direct observations on unflattened monolayer polyethylene crystals. *The Philosophical Magazine: A Journal of Theoretical Experimental and Applied Physics*, 8(94):1739–1751.

[Bassett et al., 1963b] Bassett, D. C., Frank, F. C., and Keller, A. (1963b). Some new habit features in crystals of long chain compounds part IV. the fold surface geometry of monolayer polyethylene crystals and its relevance to fold packing and crystal growth. *The Philosophical Magazine: A Journal of Theoretical Experimental and Applied Physics*, 8(94):1753–1787.

[Bassett et al., 1981] Bassett, D. C., Hodge, A. M., Olley, R. H., and Keller, A. (1981). On the morphology of melt-crystallized polyethylene - II. Lamellae and their crystallization conditions. *Proceedings of the Royal Society of London. A. Mathematical and Physical Sciences*, 377(1768):39–60.

[Berendsen et al., 1984] Berendsen, H. J. C., Postma, J. P. M., van Gunsteren, W. F., DiNola, A., and Haak, J. R. (1984). Molecular dynamics with coupling to an external bath. *The Journal of Chemical Physics*, 81(8):3684–3690.

[Bergmann, 1978] Bergmann, K. (1978). Study of the molecular motions of polyethylene by line-shape analysis of broad-line proton NMR spectra. *Journal of Polymer Science: Polymer Physics Edition*, 16(9):1611–1634.

[Bondar et al., 1996] Bondar, V. I., Kamiya, Y., and Yampol'skii, Y. P. (1996). On pressure dependence of the parameters of the dual-mode sorption model. *Journal of Polymer Science Part B: Polymer Physics*, 34(2):369–378.

[Boyer, 1973] Boyer, R. F. (1973). Glass Temperatures of Polyethylene. *Macromolecules*, 6(2):288–299.

[Brunauer et al., 1938] Brunauer, S., Emmett, P. H., and Teller, E. (1938). Adsorption of Gases in Multimolecular Layers. *Journal of the American Chemical Society*, 60(2):309–319.

[Bunn, 1939] Bunn, C. W. (1939). The crystal structure of long-chain normal paraffin hydrocarbons. The "shape" of the. *Transactions of the Faraday Society*, 35(0):482–491.

[Choy and Leung, 1985] Choy, C. L. and Leung, W. P. (1985). Elastic moduli of ultradrawn polyethylene. *Journal of Polymer Science: Polymer Physics Edition*, 23(9):1759–1780.

[Clavier, 2018] Clavier, G. (2018). *Étude à l'échelle Moléculaire Des Propriétés Mécaniques Des Polymères Semi-Cristallins*. PhD thesis, Université Paris-Saclay.

[Clugston and Flemming, 2000] Clugston, M. J. and Flemming, R. (2000). *Advanced Chemistry*. Oxford University Press, Oxford.

[Cowking et al., 1968] Cowking, A., Rider, J. G., Hay, I. L., and Keller, A. (1968). A study on the orientation effects in polyethylene in the light of crystalline texture. *Journal of Materials Science*, 3(6):646–654.

[Crank, 1979] Crank, J. (1979). *The Mathematics of Diffusion*. Clarendon Press.

[Devroye, 1986] Devroye, L. (1986). General Principles in Random Variate Generation. In Devroye, L., editor, *Non-Uniform Random Variate Generation*, pages 27–82. Springer, New York, NY.

[Eggimann et al., 2014] Eggimann, B. L., Sunnarborg, A. J., Stern, H. D., Bliss, A. P., and Siepmann, J. I. (2014). An online parameter and property database for the TraPPE force field. *Molecular Simulation*, 40(1-3):101–105.

[Ehrenstein and Theriault, 2001] Ehrenstein, G. and Theriault, R. (2001). *Polymeric Materials: Structure, Properties, Applications*. Hanser Publishers.

[Esselink et al., 1994] Esselink, K., Hilbers, P. a. J., and van Beest, B. W. H. (1994). Molecular dynamics study of nucleation and melting of n-alkanes. *The Journal of Chemical Physics*, 101(10):9033–9041.

[Favre et al., 1993] Favre, E., Nguyen, Q. T., Schaetzel, P., Clément, R., and Néel, J. (1993). Sorption of organic solvents into dense silicone membranes. Part 1.—Validity and limitations of Flory–Huggins and related theories. *Journal of the Chemical Society, Faraday Transactions*, 89(24):4339–4346.

[Ferry, 1980] Ferry, J. D. (1980). *Viscoelastic Properties of Polymers*. John Wiley & Sons.

[Flaconneche et al., 2001] Flaconneche, B., Martin, J., and Klopffer, M. H. (2001). Permeability, Diffusion and Solubility of Gases in Polyethylene, Polyamide 11 and Poly (Vinylidene Fluoride). *Oil & Gas Science and Technology - Revue d'IFP Energies nouvelles*, 56(3):261.

[Flory, 1989] Flory, J. P. (1989). *Statistical Mechanics of Chain Molecules*. Hanser Gardner Pubns, Place of publication not identified.

[Flory, 1941] Flory, P. J. (1941). Thermodynamics of High Polymer Solutions. *The Journal of Chemical Physics*, 9(8):660–660.

[Flory, 1942] Flory, P. J. (1942). Thermodynamics of High Polymer Solutions. *The Journal of Chemical Physics*, 10(1):51–61.

[Flory, 2004] Flory, P. J. (2004). Statistical Mechanics of Swelling of Network Structures. *The Journal of Chemical Physics*, 18(1):108–111.

[Flory and Rehner, 2004] Flory, P. J. and Rehner, Jr., J. (2004). Statistical Mechanics of Cross-Linked Polymer Networks II. Swelling. *The Journal of Chemical Physics*, 11(11):521–526.

[Flory and Yoon, 1978] Flory, P. J. and Yoon, D. Y. (1978). Molecular morphology in semicrystalline polymers. *Nature*, 272(5650):226–229.

[Flory et al., 1984] Flory, P. J., Yoon, D. Y., and Dill, K. A. (1984). The interphase in lamellar semicrystalline polymers. *Macromolecules*, 17(4):862–868.

[Frank, 1979] Frank, F. C. (1979). General introduction. *Faraday Discussions of the Chemical Society*, 68(0):7–13.

[Fritzsching et al., 2017] Fritzsching, K. J., Mao, K., and Schmidt-Rohr, K. (2017). Avoidance of Density Anomalies as a Structural Principle for Semicrystalline Polymers: The Importance of Chain Ends and Chain Tilt. *Macromolecules*, 50(4):1521–1540.

[Gautam et al., 2000] Gautam, S., Balijepalli, S., and Rutledge, G. C. (2000). Molecular Simulations of the Interlamellar Phase in Polymers: Effect of Chain Tilt. *Macromolecules*, 33(24):9136–9145.

[Goderis et al., 1999] Goderis, B., Reynaers, H., Koch, M. H. J., and Mathot, V. B. F. (1999). Use of SAXS and linear correlation functions for the determination of the crystallinity and morphology of semi-crystalline polymers. Application to linear polyethylene. *Journal of Polymer Science Part B: Polymer Physics*, 37(14):1715–1738.

[Greene, 2021] Greene, J. P. (2021). 3 - Microstructures of Polymers. In Greene, J. P., editor, *Automotive Plastics and Composites*, Plastics Design Library, pages 27–37. William Andrew Publishing.

[Hay and Keller, 1967] Hay, I. L. and Keller, A. (1967). A study on orientation effects in polyethylene in the light of crystalline texture. *Journal of Materials Science*, 2(6):538–558.

[Hernandez, 1994] Hernandez, R. J. (1994). Effect of water vapor on the transport properties of oxygen through polyamide packaging materials. *Journal of Food Engineering*, 22(1):495–507.

[Hernandez and Gavara, 1994] Hernandez, R. J. and Gavara, R. (1994). Sorption and transport of water in nylon-6 films. *Journal of Polymer Science Part B: Polymer Physics*, 32(14):2367–2374.

[Hernandez et al., 1992] Hernandez, R. J., Giacin, J. R., and Grulke, E. A. (1992). The sorption of water vapor by an amorphous polyamide. *Journal of Membrane Science*, 65(1):187–199.

[Hoffman and Miller, 1997] Hoffman, J. D. and Miller, R. L. (1997). Kinetic of crystallization from the melt and chain folding in polyethylene fractions revisited: Theory and experiment. *Polymer*, 38(13):3151–3212.

[Hong et al., 2016] Hong, Y.-l., Chen, W., Yuan, S., Kang, J., and Miyoshi, T. (2016). Chain Trajectory of Semicrystalline Polymers As Revealed by Solid-State NMR Spectroscopy. *ACS Macro Letters*, 5(3):355–358.

[Hong and Miyoshi, 2013] Hong, Y.-l. and Miyoshi, T. (2013). Chain-Folding Structure of a Semicrystalline Polymer in Bulk Crystals Determined by ^{13}C–^{13}C Double Quantum NMR. *ACS Macro Letters*, 2(6):501–505.

[Hoover, 1985] Hoover, W. G. (1985). Canonical dynamics: Equilibrium phase-space distributions. *Physical Review A*, 31(3):1695–1697.

[Hoy et al., 2009] Hoy, R. S., Foteinopoulou, K., and Kröger, M. (2009). Topological analysis of polymeric melts: Chain-length effects and fast-converging estimators for entanglement length. *Physical Review E*, 80(3):031803.

[Hu, 2021] Hu, T. (2021). *Permeation of High Pressure CO2 in Semicrystalline Polymers*. PhD thesis, Imperial College London.

[Hu, 2001] Hu, W. (2001). Chain folding in polymer melt crystallization studied by dynamic Monte Carlo simulations. *The Journal of Chemical Physics*, 115(9):4395–4401.

[Hu, 2018] Hu, W. (2018). The physics of polymer chain-folding. *Physics Reports*, 747:1–50.

[Huang and Brown, 1991] Huang, Y.-L. and Brown, N. (1991). Dependence of slow crack growth in polyethylene on butyl branch density: Morphology and theory. *Journal of Polymer Science Part B: Polymer Physics*, 29(1):129–137.

[Huggins, 1941] Huggins, M. L. (1941). Solutions of Long Chain Compounds. *The Journal of Chemical Physics*, 9(5):440.

[Humbert et al., 2010] Humbert, S., Lame, O., Chenal, J. M., Rochas, C., and Vigier, G. (2010). New Insight on Initiation of Cavitation in Semicrystalline Polymers: In-Situ SAXS Measurements. *Macromolecules*, 43(17):7212–7221.

[Humbert et al., 2009] Humbert, S., Lame, O., and Vigier, G. (2009). Polyethylene yielding behaviour: What is behind the correlation between yield stress and crystallinity? *Polymer*, 50(15):3755–3761.

[Hütter et al., 2006] Hütter, M., in 't Veld, P. J., and Rutledge, G. C. (2006). Polyethylene $\{201\}$ crystal surface: Interface stresses and thermodynamics. *Polymer*, 47(15):5494–5504.

[in 't Veld and Rutledge, 2003] in 't Veld, P. J. and Rutledge, G. C. (2003). Temperature-Dependent Elasticity of a Semicrystalline Interphase Composed of Freely Rotating Chains. *Macromolecules*, 36(19):7358–7365.

[in't Veld et al., 2006] in't Veld, P. J., Hütter, M., and Rutledge, G. C. (2006). Temperature-Dependent Thermal and Elastic Properties of the Interlamellar Phase of Semicrystalline Polyethylene by Molecular Simulation. *Macromolecules*, 39(1):439–447.

[Jabbari-Farouji et al., 2017] Jabbari-Farouji, S., Lame, O., Perez, M., Rottler, J., and Barrat, J.-L. (2017). Role of the Intercrystalline Tie Chains Network in the Mechanical Response of Semicrystalline Polymers. *Physical Review Letters*, 118(21):217802.

[Jabbarzadeh and Tanner, 2009] Jabbarzadeh, A. and Tanner, R. I. (2009). Crystallization of alkanes under quiescent and shearing conditions. *Journal of Non-Newtonian Fluid Mechanics*, 160(1):11–21.

[Jordan et al., 2021] Jordan, J. L., Rowland, R. L., Greenhall, J., Moss, E. K., Huber, R. C., Willis, E. C., Hrubiak, R., Kenney-Benson, C., Bartram, B., and Sturtevant, B. T. (2021). Elastic properties of polyethylene from high pressure sound speed measurements. *Polymer*, 212:123164.

[Kavassalis and Sundararajan, 1993] Kavassalis, T. A. and Sundararajan, P. R. (1993). A molecular-dynamics study of polyethylene crystallization. *Macromolecules*, 26(16):4144–4150.

[Keller, 1961] Keller, A. (1961). Some new habit features in crystals of long chain compounds. Part I. Paraffins. *The Philosophical Magazine: A Journal of Theoretical Experimental and Applied Physics*, 6(63):329–343.

[Keller, 1979] Keller, A. (1979). Crystalline polymers; an introduction. *Faraday Discussions of the Chemical Society*, 68:145.

[Kim et al., 2014] Kim, J. M., Locker, R., and Rutledge, G. C. (2014). Plastic Deformation of Semicrystalline Polyethylene under Extension, Compression, and Shear Using Molecular Dynamics Simulation. *Macromolecules*, 47(7):2515–2528.

[Klopffer and Flaconneche, 2001] Klopffer, M. H. and Flaconneche, B. (2001). Transport Properties of Gases in Polymers: Bibliographic Review. *Oil & Gas Science and Technology*, 56(3):223–244.

[Ko et al., 2004] Ko, M. J., Waheed, N., Lavine, M. S., and Rutledge, G. C. (2004). Characterization of polyethylene crystallization from an oriented melt by molecular dynamics simulation. *The Journal of Chemical Physics*, 121(6):2823–2832.

[Kolafa and Perram, 1992] Kolafa, J. and Perram, J. W. (1992). Cutoff Errors in the Ewald Summation Formulae for Point Charge Systems. *Molecular Simulation*, 9(5):351–368.

[Koyama et al., 2002] Koyama, A., Yamamoto, T., Fukao, K., and Miyamoto, Y. (2002). Molecular dynamics simulation of polymer crystallization from an oriented amorphous state. *Physical Review. E, Statistical, Nonlinear, and Soft Matter Physics*, 65(5 Pt 1):050801.

[Krishna Pant and Boyd, 1993] Krishna Pant, P. V. and Boyd, R. H. (1993). Molecular-dynamics simulation of diffusion of small penetrants in polymers. *Macromolecules*, 26(4):679–686.

[Kröger, 2005] Kröger, M. (2005). Shortest multiple disconnected path for the analysis of entanglements in two- and three-dimensional polymeric systems. *Computer Physics Communications*, 168(3):209–232.

[Kroger et al., 2023] Kroger, M., Dietz, J. D., Hoy, R. S., and Luap, C. (2023). The Z1+ package: Shortest multiple disconnected path for the analysis of entanglements in macromolecular systems. *Computer Physics Communications*, 283:108567.

[Kumaki et al., 2005] Kumaki, J., Kawauchi, T., and Yashima, E. (2005). Two-Dimensional Folded Chain Crystals of a Synthetic Polymer in a Langmuir-Blodgett Film. *Journal of the American Chemical Society*, 127(16):5788–5789.

[Kupgan et al., 2018] Kupgan, G., Demidov, A. G., and Colina, C. M. (2018). Plasticization behavior in polymers of intrinsic microporosity (PIM-1): A simulation study from combined Monte Carlo and molecular dynamics. *Journal of Membrane Science*, 565:95–103.

[Lange and Speight, 2005] Lange, N. A. and Speight, J. G. (2005). *Lange's Handbook of Chemistry / Edited by J. G. Speight.*. McGraw-Hill Professional, New York ; London, 16th ed. edition.

[Lavine et al., 2003] Lavine, M. S., Waheed, N., and Rutledge, G. C. (2003). Molecular dynamics simulation of orientation and crystallization of polyethylene during uniaxial extension. *Polymer*, 44(5):1771–1779.

[L.D. Landau & E.M. Lifshitz, 1970] L.D. Landau & E.M. Lifshitz (1970). *Theory of Elasticity*.

[Lee and Rutledge, 2011] Lee, S. and Rutledge, G. C. (2011). Plastic Deformation of Semicrystalline Polyethylene by Molecular Simulation. *Macromolecules*, 44(8):3096–3108.

[Lenz and Stein, 1973] Lenz, R. W. and Stein, R. S., editors (1973). *Structure and Properties of Polymer Films*. Springer US, Boston, MA.

[Liu and Muthukumar, 1998] Liu, C. and Muthukumar, M. (1998). Langevin dynamics simulations of early-stage polymer nucleation and crystallization. *The Journal of Chemical Physics*, 109(6):2536–2542.

[Lovinger, 2020] Lovinger, A. J. (2020). Twisted Crystals and the Origin of Banding in Spherulites of Semicrystalline Polymers. *Macromolecules*, 53(3):741–745.

[Lundberg, 1964] Lundberg, J. L. (1964). Diffusivities and solubilities of methane in linear polyethylene melts. *Journal of Polymer Science Part A: General Papers*, 2(9):3925–3931.

[Ma et al., 2019] Ma, Z., Yang, P., Zhang, X., Jiang, K., Song, Y., and Zhang, W. (2019). Quantifying the Chain Folding in Polymer Single Crystals by Single-Molecule Force Spectroscopy. *ACS Macro Letters*, 8(9):1194–1199.

[Martin and Siepmann, 1998] Martin, M. G. and Siepmann, J. I. (1998). Transferable Potentials for Phase Equilibria. 1. United-Atom Description of n-Alkanes. *The Journal of Physical Chemistry B*, 102(14):2569–2577.

[Martyna et al., 1992] Martyna, G. J., Klein, M. L., and Tuckerman, M. (1992). Nosé–Hoover chains: The canonical ensemble via continuous dynamics. *The Journal of Chemical Physics*, 97(4):2635–2643.

[Martyna et al., 1996] Martyna, G. J., Tuckerman, M. E., Tobias, D. J., and Klein, M. L. (1996). Explicit reversible integrators for extended systems dynamics. *Molecular Physics*, 87(5):1117–1157.

[Materials Design inc., a] Materials Design inc. MedeA Builders. https://www.materialsdesign.com/builders.

[Materials Design inc., b] Materials Design inc. MedeA Software. https://www.materialsdesign.com/medea-software.

[Matteucci et al., 2006] Matteucci, S., Yampolskii, Y., Freeman, B. D., and Pinnau, I. (2006). Transport of Gases and Vapors in Glassy and Rubbery Polymers. In *Materials Science of Membranes for Gas and Vapor Separation*, chapter 1, pages 1–47. John Wiley & Sons, Ltd.

[McDermott et al., 2020] McDermott, A. G., DesLauriers, P. J., Fodor, J. S., Jones, R. L., and Snyder, C. R. (2020). Measuring Tie Chains and Trapped Entanglements in Semicrystalline Polymers. *Macromolecules*, 53(13):5614–5626.

[Memari et al., 2010] Memari, P., Lachet, V., and Rousseau, B. (2010). Molecular simulations of the solubility of gases in polyethylene below its melting temperature. *Polymer*, 51(21):4978–4984.

[Memari et al., 2015] Memari, P., Lachet, V., and Rousseau, B. (2015). Gas Permeation in Semicrystalline Polyethylene as Studied by Molecular Simulation and Elastic Model. *Oil & Gas Science and Technology – Revue d'IFP Energies nouvelles*, 70(2):227–235.

[Merkel et al., 2000] Merkel, T. C., Bondar, V. I., Nagai, K., Freeman, B. D., and Pinnau, I. (2000). Gas sorption, diffusion, and permeation in poly(dimethylsiloxane). *Journal of Polymer Science Part B: Polymer Physics*, 38(3):415–434.

[Metropolis et al., 1953] Metropolis, N., Rosenbluth, A. W., Rosenbluth, M. N., Teller, A. H., and Teller, E. (1953). Equation of State Calculations by Fast Computing Machines. *The Journal of Chemical Physics*, 21(6):1087–1092.

[Meyer and Müller-Plathe, 2002] Meyer, H. and Müller-Plathe, F. (2002). Formation of Chain-Folded Structures in Supercooled Polymer Melts Examined by MD Simulations. *Macromolecules*, 35(4):1241–1252.

[Michaels and Bixler, 1961a] Michaels, A. and Bixler, H. (1961a). Solubility of Gases in Polyethylene. *Journal of Polymer Science*, 50:393–412.

[Michaels and Bixler, 1961b] Michaels, A. S. and Bixler, H. J. (1961b). Flow of gases through polyethylene. *Journal of Polymer Science*, 50(154):413–439.

[Michaels and Parker, 1959] Michaels, A. S. and Parker, R. B. (1959). Sorption and flow of gases in polyethylene. *Journal of Polymer Science*, 41(138):53–71.

[Minisini and Soldera, 2023] Minisini, B. and Soldera, A. (2023). Volumetric and Energetic Properties of Polystyrene and Polyethylene Oxide Affected by Thermal Cycling. *Macromolecular Theory and Simulations*, 32(4):2300008.

[Monasse et al., 2008] Monasse, B., Queyroy, S., and Lhost, O. (2008). Molecular Dynamics prediction of elastic and plastic deformation of semi-crystalline polyethylene. *International Journal of Material Forming*, 1(S1):1111–1114.

[Moultos et al., 2016] Moultos, O. A., Tsimpanogiannis, I. N., Panagiotopoulos, A. Z., Trusler, J. P. M., and Economou, I. G. (2016). Atomistic Molecular Dynamics Simulations of Carbon Dioxide Diffusivity in n-Hexane, n-Decane, n-Hexadecane, Cyclohexane, and Squalane. *The Journal of Physical Chemistry B*, 120(50):12890–12900.

[Moyassari et al., 2015] Moyassari, A., Mostafavi, H., Gkourmpis, T., Hedenqvist, M. S., Gedde, U. W., and Nilsson, F. (2015). Simulation of semi-crystalline polyethylene: Effect of short-chain branching on tie chains and trapped entanglements. *Polymer*, 72:177–184.

[Moyassari et al., 2017] Moyassari, A., Unge, M., Hedenqvist, M. S., Gedde, U. W., and Nilsson, F. (2017). First-principle simulations of electronic structure in semicrystalline polyethylene. *The Journal of Chemical Physics*, 146(20):204901.

[Mullin and Hobbs, 2011] Mullin, N. and Hobbs, J. K. (2011). Direct Imaging of Polyethylene Films at Single-Chain Resolution with Torsional Tapping Atomic Force Microscopy. *Physical Review Letters*, 107(19):197801.

[Murthy and Minor, 1990] Murthy, N. and Minor, H. (1990). General procedure for evaluating amorphous scattering and crystallinity from X-ray diffraction scans of semicrystalline polymers. *Polymer*, 31(6):996–1002.

[Muthukumar, 1996] Muthukumar, M. (1996). Localized structures of polymers with long-range interactions. *The Journal of Chemical Physics*, 104(2):691–700.

[Muthukumar, 2003] Muthukumar, M. (2003). Molecular modelling of nucleation in polymers. *Philosophical Transactions of the Royal Society of London. Series A: Mathematical, Physical and Engineering Sciences*.

[Mutter et al., 1993] Mutter, R., Stille, W., and Strobl, G. (1993). Transition regions and surface melting in partially crystalline polyethylene: A raman spectroscopic study. *Journal of Polymer Science Part B: Polymer Physics*, 31(1):99–105.

[Naito et al., 1996] Naito, Y., Kamiya, Y., Terada, K., Mizoguchi, K., and Wang, J.-S. (1996). Pressure dependence of gas permeability in a rubbery polymer. *Journal of Applied Polymer Science*, 61(6):945–950.

[Naito et al., 1991] Naito, Y., Mizoguchi, K., Terada, K., and Kamiya, Y. (1991). The effect of pressure on gas permeation through semicrystalline polymers above the glass transition temperature. *Journal of Polymer Science Part B: Polymer Physics*, 29(4):457–462.

[Nakamae et al., 1991] Nakamae, K., Nishino, T., and Ohkubo, H. (1991). Elastic modulus of crystalline regions of polyethylene with different microstructures: Experimental proof of homogeneous stress distribution. *Journal of Macromolecular Science, Part B*, 30(1-2):1–23.

[Nielsen, 1954] Nielsen, L. E. (1954). Effect of Crystallinity on the Dynamic Mechanical Properties of Polyethylenes. *Journal of Applied Physics*, 25:1209–1212.

[Nilsson et al., 2012] Nilsson, F., Lan, X., Gkourmpis, T., Hedenqvist, M., and Gedde, U. (2012). Modelling tie chains and trapped entanglements in polyethylene. *Polymer*, 53(16):3594–3601.

[Nosé, 1984] Nosé, S. (1984). A unified formulation of the constant temperature molecular dynamics methods. *The Journal of Chemical Physics*, 81(1):511–519.

[Oktay and Gürses, 2015] Oktay, H. E. and Gürses, E. (2015). Modeling of spherulite microstructures in semicrystalline polymers. *Mechanics of Materials*, 90:83–101.

[Olsson et al., 2018] Olsson, P. A., in 't Veld, P. J., Andreasson, E., Bergvall, E., Persson Jutemar, E., Petersson, V., Rutledge, G. C., and Kroon, M. (2018). All-atomic and coarse-grained molecular dynamics investigation of deformation in semi-crystalline lamellar polyethylene. *Polymer*, 153:305–316.

[Pandiyan and Rousseau, 2013] Pandiyan, S. and Rousseau, B. (2013). Factors influencing properties of interfacial regions in semicrystalline polyethylene: A molecular dynamics simulation study. *Polymer*, 54(14):3586–3593.

[Parrinello and Rahman, 1981] Parrinello, M. and Rahman, A. (1981). Polymorphic transitions in single crystals: A new molecular dynamics method. *Journal of Applied Physics*, 52(12):7182–7190.

[Paul, 2016] Paul, D. R. (2016). Dual Mode Sorption Model. In Drioli, E. and Giorno, L., editors, *Encyclopedia of Membranes*, pages 1–2. Springer, Berlin, Heidelberg.

[Peacock, 2000] Peacock, A. (2000). *Handbook of Polyethylene: Structures: Properties, and Applications*. CRC Press.

[Peterlin, 1980] Peterlin, A. (1980). Chain Folding in Lamellar Crystals. *Macromolecules*, 13(4):777–782.

[Pethrick, 2007] Pethrick, R. A. (2007). *Polymer Structure Characterization: From Nano To Macro Organization*. Royal Society of Chemistry.

[Pino et al., 2005] Pino, M., Duckett, R. A., and Ward, I. M. (2005). Single and mixed gas diffusion through polyethylene films. *Polymer*, 46(13):4882–4890.

[Plimpton et al., 1997] Plimpton, S., Pollock, R., and Stevens, M. (1997). Particle-Mesh Ewald and rRESPA for Parallel Molecular Dynamics Simulations. In *In Proceedings of the Eighth SIAM Conference on Parallel Processing for Scientific Computing*.

[Point et al., 1969] Point, J. J., Homés, G. A., Gezovich, D., and Keller, A. (1969). A study on the orientation effects in polyethylene in the light of crystalline texture. *Journal of Materials Science*, 4(10):908–918.

[Queyroy and Monasse, 2012] Queyroy, S. and Monasse, B. (2012). Effect of the molecular structure of semicrystalline polyethylene on mechanical properties studied by molecular dynamics. *Journal of Applied Polymer Science*, 125(6):4358–4367.

[Ramos et al., 2015] Ramos, J., Vega, J. F., and Martínez-Salazar, J. (2015). Molecular Dynamics Simulations for the Description of Experimental Molecular Conformation, Melt Dynamics, and Phase Transitions in Polyethylene. *Macromolecules*, 48(14):5016–5027.

[Ramos et al., 2008] Ramos, J., Vega, J. F., Theodorou, D. N., and Martinez-Salazar, J. (2008). Entanglement Relaxation Time in Polyethylene: Simulation versus Experimental Data. *Macromolecules*, 41(8):2959–2962.

[Ranganathan et al., 2020] Ranganathan, R., Kumar, V., Brayton, A. L., Kröger, M., and Rutledge, G. C. (2020). Atomistic Modeling of Plastic Deformation in Semicrystalline Polyethylene: Role of Interphase Topology, Entanglements, and Chain Dynamics. *Macromolecules*, 53(12):4605–4617.

[Ray, 1983] Ray, J. R. (1983). Molecular dynamics equations of motion for systems varying in shape and size. *The Journal of Chemical Physics*, 79(10):5128–5130.

[Rigby et al., 2016] Rigby, D., Saxe, P. W., Freeman, C. M., and Leblanc, B. (2016). Computational Prediction of Mechanical Properties of Glassy Polymer Blends and Thermosets. In Sano, T., Srivatsan, T. S., and Peretti, M. W., editors, *Advanced Composites for Aerospace, Marine, and Land Applications*, pages 157–171. Springer International Publishing, Cham.

[Rogers, 1985a] Rogers, C. E. (1985a). Permeation of Gases and Vapours in Polymers. In Comyn, J., editor, *Polymer Permeability*, pages 11–73. Springer Netherlands, Dordrecht.

[Rogers, 1985b] Rogers, C. E. (1985b). Sorption and diffusion in multicomponent polymers. *Journal of Polymer Science: Polymer Symposia*, 72(1):301–301.

[Rogers et al., 1959] Rogers, C. E., Stannett, V., and Szwarc, M. (1959). The Sorption of Organic Vapors by Polyethylene. *The Journal of Physical Chemistry*, 63(9):1406–1413.

[Roguet et al., 2019] Roguet, E., Akhan, K., Brusselle-Dupend, N., Le Corre, V., Sidhom, M., Cangemi, L., Moreaud, M., Clavier, G., Lachet, V., and Rousseau, B. (2019). Investigation of the 3D crystalline network impact on the elastic properties of Semi-Crystalline Polymers from a multi-scale modelling approach. *Computational Materials Science*, 167:77–84.

[Rubinstein, 2007] Rubinstein, M. (2007). *Polymer Physics*. Oxford University Press, Oxford ;.

[Rutledge, 2002] Rutledge, G. C. (2002). Implications of Metastability for the Crystal/Amorphous Interface from Molecular Simulation. *Journal of Macromolecular Science, Part B*, 41(4-6):909–922.

[Ryan et al., 1994] Ryan, A. J., Bras, W., Mant, G. R., and Derbyshire, G. E. (1994). A direct method to determine the degree of crystallinity and lamellar thickness of polymers: Application to polyethylene. *Polymer*, 35(21):4537–4544.

[Sadler and Keller, 1977] Sadler, D. M. and Keller, A. (1977). Neutron Scattering Studies on the Molecular Trajectory in Polyethylene Crystallized from Solution and Melt. *Macromolecules*, 10(5):1128–1140.

[Sakurada et al., 1964] Sakurada, I., Ito, T., and Nakamae, K. (1964). Elastic Moduli of Crystal Lattices of Polymers (Special Issue on Polymer Chemistry, I). *Bulletin of the Institute for Chemical Research, Kyoto University*, 42(2-3):77–92.

[Sanchez and Lacombe, 1976] Sanchez, I. C. and Lacombe, R. H. (1976). An elementary molecular theory of classical fluids. Pure fluids. *The Journal of Physical Chemistry*, 80(21):2352–2362.

[Sanchez and Lacombe, 1978] Sanchez, I. C. and Lacombe, R. H. (1978). Statistical Thermodynamics of Polymer Solutions. *Macromolecules*, 11(6):1145–1156.

[Savage et al., 2015] Savage, R. C., Mullin, N., and Hobbs, J. K. (2015). Molecular Conformation at the Crystal–Amorphous Interface in Polyethylene. *Macromolecules*, 48(17):6160–6165.

[Schelten et al., 1976] Schelten, J., Ballard, D. G. H., Wignall, G. D., Longman, G., and Schmatz, W. (1976). Small-angle neutron scattering studies of molten and crystalline polyethylene. *Polymer*, 17(9):751–757.

[Schelten et al., 1977] Schelten, J., Wignall, G. D., Ballard, D. G. H., and Longman, G. W. (1977). Small-angle neutron scattering studies of molecular clustering in mixtures of polyethylene and deuterated polyethylene. *Polymer*, 18(11):1111–1120.

[Seguela, 2005] Seguela, R. (2005). Critical review of the molecular topology of semicrystalline polymers: The origin and assessment of intercrystalline tie molecules and chain entanglements. *Journal of Polymer Science Part B: Polymer Physics*, 43(14):1729–1748.

[Seignobos, 2009] Seignobos, E. (2009). *Compréhension des mécanismes physiques de fatigue dans le polyamide vierge et renforcé de fibres de verre*. Thèse de doctorat, Institut national des sciences appliquées de Lyon, Lyon, France.

[Shanbhag and Kröger, 2007] Shanbhag, S. and Kröger, M. (2007). Primitive Path Networks Generated by Annealing and Geometrical Methods: Insights into Differences. *Macromolecules*, 40(8):2897–2903.

[Shinoda et al., 2004] Shinoda, W., Shiga, M., and Mikami, M. (2004). Rapid estimation of elastic constants by molecular dynamics simulation under constant stress. *Physical Review B*, 69(13):134103.

[Soldera and Metatla, 2006] Soldera, A. and Metatla, N. (2006). Glass transition of polymers: Atomistic simulation versus experiments. *Physical Review E*, 74(6):061803.

[Sommer and Luo, 2010] Sommer, J.-U. and Luo, C. (2010). Molecular dynamics simulations of semicrystalline polymers: Crystallization, melting, and reorganization. *Journal of Polymer Science Part B: Polymer Physics*, 48(21):2222–2232.

[Spells and Sadler, 1984] Spells, S. J. and Sadler, D. M. (1984). Neutron scattering studies on solution-grown crystals of polyethylene: A statistical preference for adjacent re-entry. *Polymer*, 25(6):739–748.

[Stamm et al., 1979] Stamm, M., Fischer, E. W., Dettenmaier, M., and Convert, P. (1979). Chain conformation in the crystalline state by means of neutron scattering methods. *Faraday Discussions of the Chemical Society*, 68(0):263–278.

[Strobl and Hagedorn, 1978] Strobl, G. R. and Hagedorn, W. (1978). Raman spectroscopic method for determining the crystallinity of polyethylene. *Journal of Polymer Science: Polymer Physics Edition*, 16(7):1181–1193.

[Suwandi and Stern, 1973] Suwandi, M. S. and Stern, S. A. (1973). Transport of heavy organic vapors through silicone rubber. *Journal of Polymer Science: Polymer Physics Edition*, 11(4):663–681.

[Takayanagi and Nitta, 1997] Takayanagi, M. and Nitta, K.-h. (1997). Application of a tie molecule model to the postyielding deformation of crystalline polymers. *Macromolecular Theory and Simulations*, 6(1):181–195.

[Takeuchi, 1998] Takeuchi, H. (1998). Structure formation during the crystallization induction period of a short chain-molecule system: A molecular dynamics study. *The Journal of Chemical Physics*, 109(13):5614–5621.

[Tashiro et al., 1978a] Tashiro, K., Kobayashi, M., and Tadokoro, H. (1978a). Calculation of Three-Dimensional Elastic Constants of Polymer Crystals. 1. Method of Calculation. *Macromolecules*, 11(5):908–913.

[Tashiro et al., 1978b] Tashiro, K., Kobayashi, M., and Tadokoro, H. (1978b). Calculation of Three-Dimensional Elastic Constants of Polymer Crystals. 2. Application to Orthorhombic Polyethylene and Poly(vinyl alcohol). *Macromolecules*, 11(5):914–918.

[Theodorou and Suter, 1985] Theodorou, D. N. and Suter, U. W. (1985). Detailed molecular structure of a vinyl polymer glass. *Macromolecules*, 18(7):1467–1478.

[Thompson et al., 2022] Thompson, A. P., Aktulga, H. M., Berger, R., Bolintineanu, D. S., Brown, W. M., Crozier, P. S., in 't Veld, P. J., Kohlmeyer, A., Moore, S. G., Nguyen, T. D., Shan, R., Stevens, M. J., Tranchida, J., Trott, C., and Plimpton, S. J. (2022). LAMMPS - a flexible simulation tool for particle-based materials modeling at the atomic, meso, and continuum scales. *Computer Physics Communications*, 271:108171.

[Togawa et al., 2001] Togawa, J., Horiuchi, J.-i., Kanno, T., and Kobayashi, M. (2001). Freeze–purged–desorption method for quantitative evaluation of CO2-solubility in polymeric films. *Journal of Membrane Science*, 182(1):125–128.

[Velioglu et al., 2012] Velioglu, S., Ahunbay, M. G., and Tantekin-Ersolmaz, S. B. (2012). Investigation of CO2-induced plasticization in fluorinated polyimide membranes via molecular simulation. *Journal of Membrane Science*, 417–418:217–227.

[Velioglu et al., 2018] Velioglu, S., Ahunbay, M. G., and Tantekin-Ersolmaz, S. B. (2018). An atomistic insight on CO2 plasticization resistance of thermally rearranged 6FDA-bisAPAF. *Journal of Membrane Science*, 556:23–33.

[Vittoria, 1995] Vittoria, V. (1995). Influence of the crystallinity on the transport properties of polyethylene. *Journal of Materials Science*, 30(15):3954–3958.

[Voigt-Martin et al., 1980] Voigt-Martin, I. G., Fischer, E. W., and Mandelkern, L. (1980). Morphology of melt-crystallized linear polyethylene fractions and its dependence on molecular weight and crystallization temperature. *Journal of Polymer Science: Polymer Physics Edition*, 18(12):2347–2367.

[Voigt-Martin and Mandelkern, 1984] Voigt-Martin, I. G. and Mandelkern, L. (1984). A quantitative electron microscopic study of the crystallite structure of molecular weight fractions of linear polyethylene. *Journal of Polymer Science: Polymer Physics Edition*, 22(11):1901–1917.

[Voigt-Martin et al., 1989] Voigt-Martin, I. G., Stack, G. M., Peacock, A. J., and Mandelkern, L. (1989). A comparison of the Raman LAM and electron microscopy in determining crystallite thickness distributions: Polyethylenes with narrow size distributions. *Journal of Polymer Science Part B: Polymer Physics*, 27(5):957–965.

[Von Solms et al., 2004] Von Solms, N., Nielsen, J. K., Hassager, O., Rubin, A., Dandekar, A. Y., Andersen, S. I., and Stenby, E. H. (2004). Direct measurement of gas solubilities in polymers with a high-pressure microbalance. *Journal of Applied Polymer Science*, 91(3):1476–1488.

[Wang et al., 2017] Wang, Z., An, M., Xu, H., Lv, Y., Tian, F., and Gu, Q. (2017). Structural evolution from shish-kebab to fibrillar crystals during hot-stretching process of gel spinning ultra-high molecular weight polyethylene fibers obtained from low concentration solution. *Polymer*, 120:244–254.

[Watts and Bacon, 1974] Watts, D. G. and Bacon, D. W. (1974). Using An Hyperbola as a Transition Model to Fit Two-Regime Straight-Line Data. *Technometrics*, 16(3):369–373.

[Yamamoto, 2008] Yamamoto, T. (2008). Molecular dynamics simulations of steady-state crystal growth and homogeneous nucleation in polyethylene-like polymer. *The Journal of Chemical Physics*, 129(18):184903.

[Yamamoto, 2010] Yamamoto, T. (2010). Molecular dynamics simulations of polymer crystallization in highly supercooled melt: Primary nucleation and cold crystallization. *The Journal of Chemical Physics*, 133(3):034904.

[Yeh et al., 2015] Yeh, I.-C., Andzelm, J. W., and Rutledge, G. C. (2015). Mechanical and Structural Characterization of Semicrystalline Polyethylene under Tensile Deformation by Molecular Dynamics Simulations. *Macromolecules*, 48(12):4228–4239.

[Yi and Rutledge, 2011] Yi, P. . and Rutledge, G. C. (2011). Molecular simulation of bundle-like crystal nucleation from n-eicosane melts. *The Journal of Chemical Physics*, 135(2):024903.

[Yi et al., 2013] Yi, P., Locker, C. R., and Rutledge, G. C. (2013). Molecular Dynamics Simulation of Homogeneous Crystal Nucleation in Polyethylene. *Macromolecules*, 46(11):4723–4733.

[Yi and Rutledge, 2009] Yi, P. and Rutledge, G. C. (2009). Molecular simulation of crystal nucleation in n-octane melts. *The Journal of Chemical Physics*, 131(13):134902.

[Yoon and Flory, 1984] Yoon, D. Y. and Flory, P. J. (1984). Chain packing at polymer interfaces. *Macromolecules*, 17(4):868–871.

[Zhang and Larson, 2018] Zhang, W. and Larson, R. G. (2018). Direct All-Atom Molecular Dynamics Simulations of the Effects of Short Chain Branching on Polyethylene Oligomer Crystal Nucleation. *Macromolecules*, 51(13):4762–4769.

[Zumdahl and Zumdahl, 2012] Zumdahl, S. S. and Zumdahl, S. A. (2012). *Chemistry : An Atoms First Approach*. Bellmont, CA : Brooks/Cole, CENGAGE Learning.

-